Studies in Magnetoelasticity

Finlay Ryburn
Magdalen College

A thesis presented for the degree of Doctor of Philosophy

Department of Physics
University of Oxford
Hilary Term 2024

Studies in Magnetoelasticity

Submitted for the degree of Doctor of Philosophy

Finlay Ryburn, Magdalen College, University of Oxford

Hilary Term 2024

Abstract

This thesis is divided into two halves: the first reports on the study of surface acoustic waves (SAWs) in thin magnetic films and their magnetoelastic coupling with spin waves; the second describes a study of magnetoelastic torque sensors used in electric bicycles.

Chapter 1 motivates the need for alternative computing architectures to improve performance and reduce energy consumption. One such alternative, spin-wave computing, is introduced, alongside a possible energy-efficient mechanism for spin-wave excitation using SAWs.

Chapter 2 describes the experimental process used to fabricate yttrium iron garnet zinc oxide heterostructures, in which the coupling between SAWs and spin waves can be studied.

Chapter 3 sets out a theoretical model to determine the properties of SAWs in thin film multilayers. Chapter 4 outlines a theoretical model to describe the coupling of SAWs with spin waves.

Chapter 5 presents the micro-focused Brillouin light scattering data used to analyse the samples. Firstly, the SAW transducer frequency response and SAW group velocities are measured; following this, data showing the coupling of SAWs with spin waves is presented. The coupling is highly non-reciprocal, which agrees with the predictions from the theoretical model. Finally, in Chapter 6, concluding remarks on this first part of the thesis are given.

Acknowledgements

Firstly, I would like to express my gratitude to my supervisor, Prof. John Gregg, for his guidance, enthusiasm, and support. His intuitive approach to physics, many entertaining tales, and unhesitating willingness to dive in and fix your experiment (or car) have always been greatly appreciated.

I would also like to thank Dr. Alexy Karenowska for the out-of-the-blue introduction to the DPhil, Dr. Dharmalingam Prabhakaran for his kind help in annealing samples, and Yangzhan Zhang for his help with the calculations of SAW properties. I am grateful to the Clarendon Workshop, particularly Jon Denton and Pete Thompson, for their support and teaching me a little of the art of milling and turning. I also want to thank Phil Prior and Dan Lordan for their help in the lab, Alan Francis for always knowing where to find whatever you needed, and all the exceptional personnel that keep the Department afloat.

I am very grateful to Prof. Dr. Mathias Weiler for his great many insights and direction in our collaborative work. In addition, many others at RPTU made my visits both academically rewarding and good fun. Jun. Prof. Dr. Philipp Pirro, Anna Maria Friedel, Yannik Kunz, Philipp Schwenke, Julian Schüler, and Dr. Michael Schneider, to name a few. In particular, however, I want to thank Kevin Künstle, whose friendship and good humour saw us through many hours of BLS microscopy and cleanroom work.

I would like to thank Methode Electronics for partially funding my DPhil project, and I am grateful to Assed Mir and Ignazio Barraco for their support. Thanks also go to Dr. Jing Wu and Dr. Gonzalo Vallejo Fernandez for their help with MOKE and VSM measurements, and Tony Hickman for preparing samples.

I could not have been more fortunate to have Sally Lord and Will Henderson join me in Room 174. Not only did they make day-to-day study infinitely more enjoyable, but I have also made lifelong friends; from our trips to Nancy and conferences to parties and pub visits. The DPhil journey is certainly better with good company.

I am also thankful to all my other friends for keeping me going through what was, at times, a challenging experience. In particular, Darius, Linda, Shu, Mitchell, and Lachlan, with whom I will warmly remember our weekend trips.

Finally, I am especially grateful to my supportive family for always encouraging my further study (even if they might not understand what I do very well), in particular to my mum, sisters, Meg and Caitlin, gran, Irene, and Sue, Robin, and Pablo. Also, to Romina for her patience, love, and support, always cheering up my days. Lastly, a special mention to my dad, who would have been very proud of this achievement and was a wonderfully supportive and loving father.

Finlay Ryburn, April 2024

Dedicated to my parents,
Liz and Murray.

Contents

List of Figures

List of Tables

List of Abbreviations

SAW . . . . . Surface Acoustic Wave

IDT . . . . . Interdigital Transducer

LLG . . . . . Landau-Lifshitz-Gilbert

FMR . . . . . Ferromagnetic Resonance

BVMSW . . . Backward Volume Magnetostatic Spin Wave

MSSW . . . . Magnetostatic Surface Spin Wave

YIG . . . . . Yttrium Iron Garnet

GGG . . . . . Gadolinium Gallium Garnet

PMMA . . . . Polymethyl Methacrylate

LPE . . . . . Liquid Phase Epitaxy

EBL . . . . . Electron Beam Lithography

RF . . . . . Radio Frequency

XRD . . . . . X-ray Diffraction

μ-BLS . . . . . Micro-focused Brillouin Light Scattering

FPI . . . . . Fabry-Pérot Interferometer

TFPI . . . . . Tandem Fabry-Pérot Interferometer

Part I

The coupling of surface acoustic waves and spin waves

1 Motivation and introduction

To mitigate overheating risks, computer processor clock speeds were frozen about 20 years ago [1]. This marked the beginning of significant challenges for conventional silicon-based computing. These challenges signify a departure from the historical trend of doubling transistor density in integrated circuits every few years, effectively signalling the end of Moore's Law [1–4]. When combined with the considerable environmental impact associated with the 2.5% of global greenhouse gas emissions estimated to come from information and communication technology [5], a strong motivation is provided for developing alternative computing architectures.

Conventional computing primarily relies on the movement of electrons and holes for information transfer and processing. However, inherent scattering during this process results in Joule heating, leading to the aforementioned overheating risks and performance limitations. Addressing these challenges necessitates exploring alternative information carriers that do not suffer from such drawbacks.

Electrons are spin 1/2 particles and, therefore, in addition to their charge, possess an intrinsic magnetic moment. In magnetically ordered materials, the phase-coherent precession of these magnetic moments allows the transport of angular momentum through the system in the form of spin waves, a representation of which can be seen in Fig. 1.1. The quasiparticle that quantises these spin waves is the magnon, the study of which constitutes the field of Magnonics.

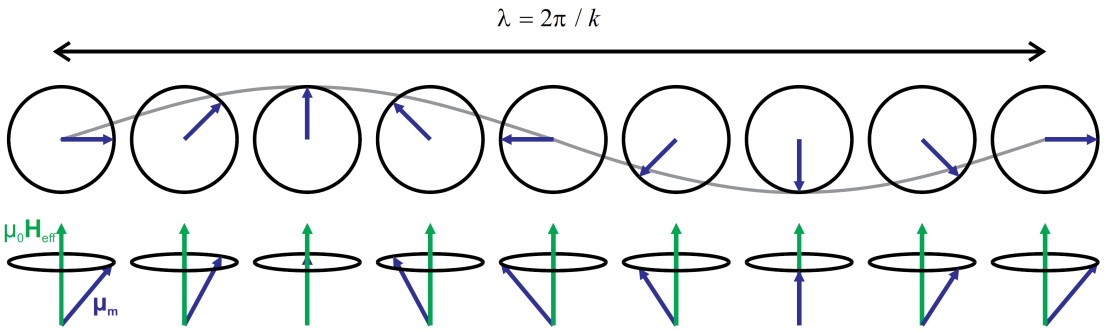

Figure 1.1: Schematic diagram of a spin wave in one dimension. The effective magnetic field is shown by the green arrows around which the coupled magnetic moments, blue arrows, precess. The wavelength, λ, is shown, as its relation to the wavevector, k; adapted from [6].

Magnons present a promising alternative for computing architecture, offering the potential for terahertz clock speeds, greatly reduced footprints, and up to 1000 times less heat waste [7–9]. Moreover, magnons offer a number of interesting properties that could lend themselves to unconventional computing architectures, including easily accessible non-linearity [10, 11], negative group velocities [12], and tunable dispersion relations governed by an externally applied magnetic field [13]. These properties are illustrated in Fig. 1.2, where the magnon dispersion relations in a thin magnetic film are shown as a function of the magnetic field direction relative to the magnon propagation direction and highlight the versatility of magnons for novel computing paradigms.

Experiments and simulations have already demonstrated the feasibility of various magnonic devices, such as magnon transistors [15], artificial crystals for time-reversal [16, 17], majority gates [18], half adders [19], and a nanoscale neural network for vowel recognition [20]. To function effectively, all these devices require an energy-efficient mechanism for the generation of magnons. Common excitation techniques, utilising conventional microwave antenna or spin pumping via the spin-hall effect, suffer from Joule heating, returning us to our initial problem. Thus, an alternative is required [21–24].

The first part of this thesis explores one such alternative mechanism: the coupling between surface acoustic waves (SAWs) and spin waves. Exploiting this

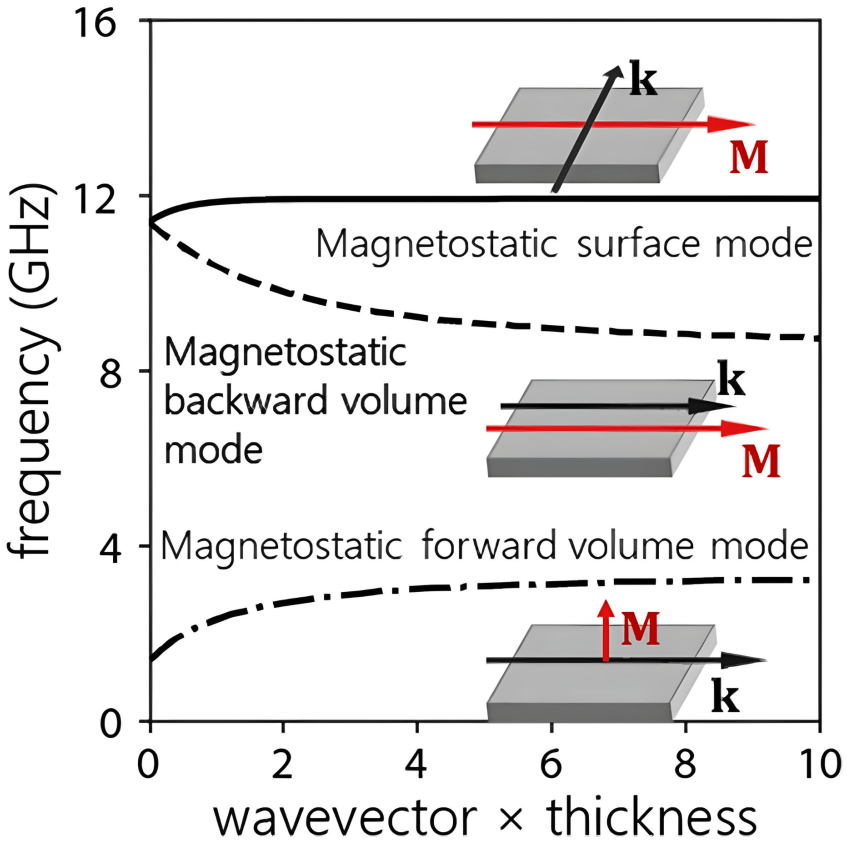

Figure 1.2: An illustration of the magnon dispersion relations that arise depending on the direction of the applied external magnetic field relative to the direction of propagation of the magnon. The three different modes, with the different shapes and frequencies of their dispersion relations when at the same external magnetic field, are shown. The negative gradient of the magnetostatic backward volume mode indicates that these magnons have negative group velocities, adapted from [14].

coupling not only offers a potential method for energy-efficient magnon excitation but also, as we will show, introduces non-reciprocal behaviour, thereby enhancing device functionality.

Before discussing the coupling mechanism between SAWs and spin waves, a brief introduction to SAWs, piezoelectricity, and our piezoelectric material of choice, zinc oxide (ZnO), is provided. This is followed by an introduction to spin waves and our magnetic material of choice, yttrium iron garnet (YIG).

Note that large parts of Chapters 1 to 6 of this thesis are based on the publication Ryburn et al. [25].

1.1 Surface acoustic waves (SAWs)

SAWs are acoustic waves that propagate along the free surface of a solid material, typically with a frequency range between a few megahertz to several gigahertz. There are a few different types of SAWS, but perhaps the most well-known is the Rayleigh wave, discovered by Lord Rayleigh in 1885 [26]. These SAWs induce an elliptical particle motion, with a transverse component normal to the surface and a longitudinal component. All SAWs have a characteristic exponentially decaying amplitude with distance from the free surface, with decay lengths typically on the order of one wavelength [27].

In more recent times, SAWs have become ubiquitous in modern life; indeed, most of us carry SAW devices every day in the form of mobile telephone filters [28, 29], owing to their relatively short wavelengths at gigahertz frequencies compared to their electromagnetic counterparts. Other applications include sensors [30, 31], oscillators [32, 33], and microfluidic actuators [34, 35].

Note that analogously to spin waves, in the quantum picture, acoustic waves can be thought of in terms of their quasiparticle equivalent, the phonon. Phonons carry quantised vibrational mechanical energy in solids and some liquids [36].

1.1.1 Piezoelectricity

Historically, SAWs were observed in nature, helping to explain the features of seismic records when generated by earthquakes, for example. However, to integrate SAWs into devices, an artificial generation mechanism is necessary. To realise this, we rely on a property of certain materials whereby they generate an electric charge in response to applied mechanical stress or, conversely, undergo mechanical deformation when subject to an electric field. Such materials are known as piezoelectrics.

Piezoelectric materials have non-centrosymmetric crystal symmetry and, therefore, can have an inherent electric dipole moment. When a mechanical force is applied to such a material, it causes a distortion in the crystal lattice, resulting in a separation of positive and negative charges and subsequently polarising the unit cell, thereby generating an electric field. This is shown schematically in

Fig. 1.3. Conversely, applying an electric field distorts the crystal lattice, and hence, by applying an oscillating electric field, the oscillating mechanical response of a piezoelectric material can generate an acoustic wave. Commonly used piezoelectric materials include quartz, Rochelle salt, lead zirconate titanate (PZT), and ZnO [37].

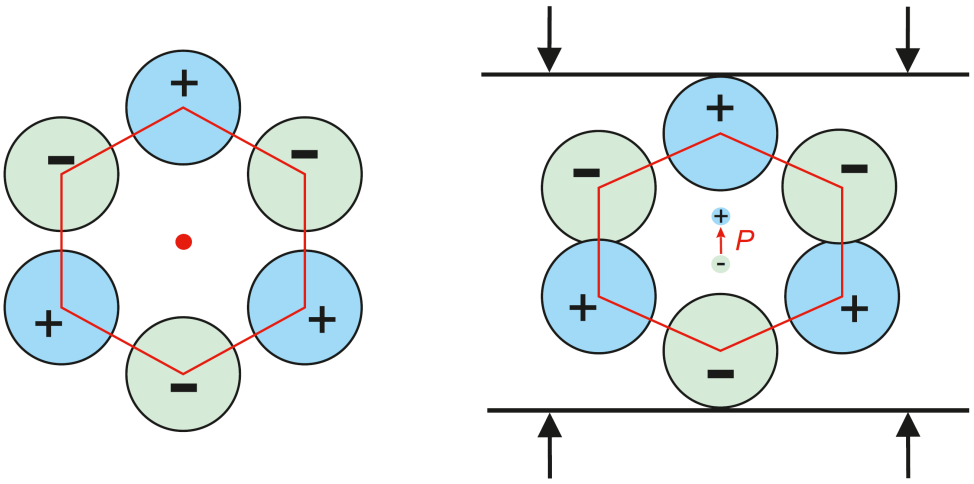

Figure 1.3: A schematic representation of the piezoelectric effect. On the left, there is a non-centrosymmetric hexagonal unit cell. On the right, under the application of a mechanical force represented by the black lines and arrows, the unit cell is polarised, inducing an electric field; adapted from [38].

1.1.2 Interdigital transducers

To generate the electric field required to excite a SAW in a piezoelectric material, a certain geometry of metallic contacts, referred to as interdigital transducers (IDTs), is used; a diagram of an IDT is shown in Fig. 1.4. As can be seen, there are a pair of 'interdigitated' electrodes which are patterned on the surface of a piezoelectric substrate. When an alternating voltage is applied to the electrodes, an electric field that alternates between positive and negative polarities is generated. This alternating electric field causes the piezoelectric substrate to expand and contract cyclically, generating SAWs that propagate perpendicular to the IDT fingers. Due to the reversibility of the piezoelectric effect, the inverse process can be used to detect an incoming SAW, converting it to an electrical signal, thus allowing the transfer of electrical information via SAWs.

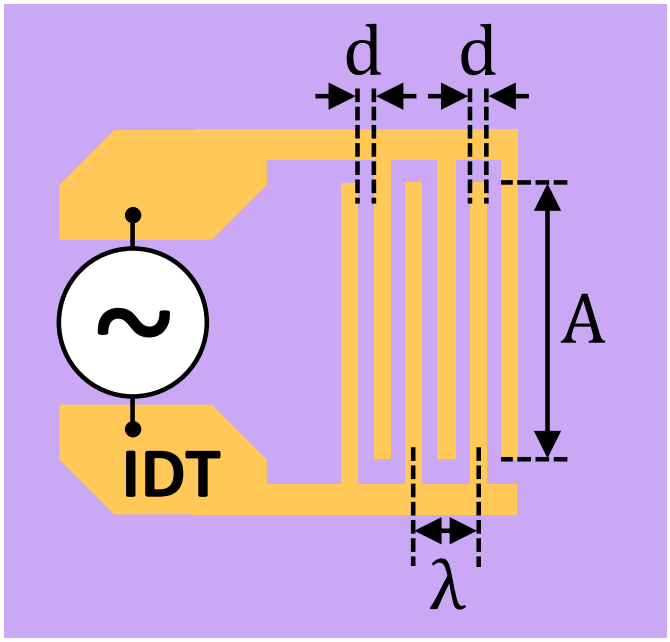

Figure 1.4: A schematic depiction of an interdigital transducer (IDT). Two electrically isolated pads are shown with an alternating voltage applied between them. Six overlapping fingers, three per pad, can be seen with width d. The finger spacings, in this case, are also given by d, resulting in a periodicity in the structure of $4d$, which sets the fundamental wavelength of the transducer λ. The dimension A gives the aperture size of the IDT.

Returning to Fig. 1.4, we can see that the structure has a periodicity of $4d$. This periodicity sets the fundamental wavelength, λ, and, therefore, fundamental frequency, f, ($v = f\lambda$ where v is the wave's velocity) of the transducer. IDTs can also be operated at higher harmonics of the fundamental frequency. As a net electric field between the fingers is required to excite a SAW, the wavelengths of these higher-order harmonics are given by λ/n, where n is an odd integer. Finally, the bandwidth of an IDT is determined predominately by the number of finger pairs; the more pairs, the narrower the bandwidth.

1.1.3 Zinc oxide (ZnO)

Having discussed the generation of SAWs, a piezoelectric material suitable for exciting them is required. We chose to use ZnO given it is a well-established piezoelectric material, capable of generating high-frequency SAWs on account of its relatively high acoustic wave velocity and electromechanical coupling coefficient [39–43].

Zinc oxide predominantly crystallises into the stable, electrically insulating, hexagonal wurtzite structure, pictured in Fig. 1.5. This structure has point group symmetry $6mm$ and space group $P6_3mc$. It is characterised by the two lattice parameters shown, $a = 0.32495\,\text{nm}$ and $c = 0.52069\,\text{nm}$ [27, 44]. If we flip the c-axis, we can see there is a lack of inversion symmetry, which gives rise to an electric dipole moment associated with this axis. Therefore, the c-axis defines the piezoelectric axis.

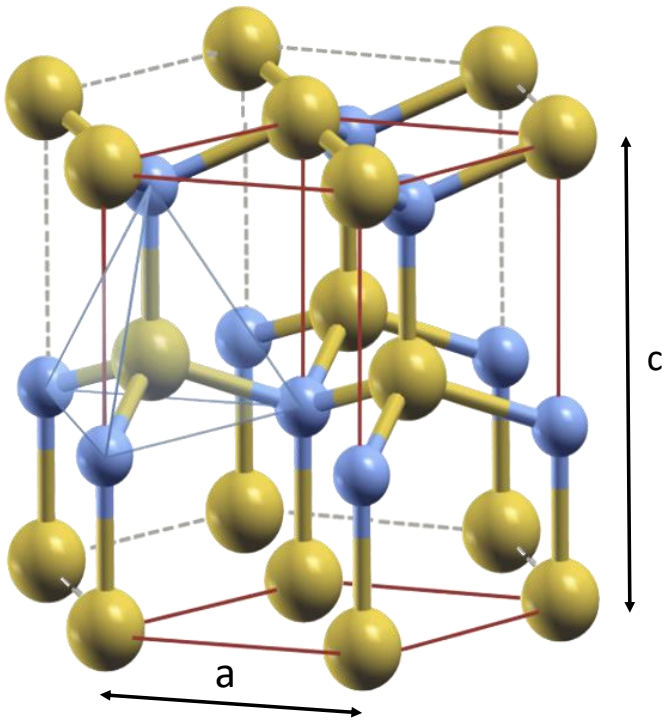

Figure 1.5: The atomic arrangement in the hexagonal wurtzite structure of zinc oxide. The zinc atoms are represented by the blue spheres, and the oxygen atoms by the yellow spheres. The two hexagonal lattice parameters, $a = 0.32495\,\text{nm}$ and $c = 0.52069\,\text{nm}$, are also shown. The c-axis is in the (0001) direction. On reversing the c-axis, it is evident that there is a lack of inversion symmetry, which gives rise to the piezoelectricity of ZnO. Figure adapted from [45].

It is important to note that the c-axes must align globally for piezoelectric action. If the c-axes are either randomly oriented or with equal numbers of aligned and anti-aligned axes, the global piezoelectric action will cancel. It is, therefore, important to ensure that there is good c-axis alignment when growing thin films of ZnO. Fortunately, using radio frequency magnetron sputtering, it is possible to

grow thin films of ZnO that preferentially form out-of-plane c-axis aligned columnar grains, as will be discussed further in Section 2.1.5.

1.2 Spin waves

1.2.1 The magnetic moment

As mentioned, electrons carry a form of intrinsic angular momentum known as spin, and associated with this spin, an intrinsic magnetic dipole moment given by

$$\boldsymbol{\mu}_{\mathrm{S}} = -\frac{g_{\mathrm{e}} e}{2m_{\mathrm{e}}}\boldsymbol{S}, \tag{1.1}$$

where $\boldsymbol{S}$ is the spin angular momentum, g_{e} the electron spin g-factor, e the elementary electron charge, and m_{e} the mass of the electron. For the more general case with an additional orbital angular momentum $\boldsymbol{L}$ and, therefore, total angular momentum $\boldsymbol{J} = \boldsymbol{L} + \boldsymbol{S}$ the magnetic momentum is given by

$$\boldsymbol{\mu} = -\frac{g_{\mathrm{J}} e}{2m_{\mathrm{e}}}\boldsymbol{J} = -\gamma \boldsymbol{J} \tag{1.2}$$

where g_{J} is the Landé g-factor and γ the gyromagnetic ratio.

1.2.2 The Landau-Lifshitz-Gilbert equation

The torque, $\boldsymbol{\tau}$, exerted on a magnetic moment by a magnetic field, $\boldsymbol{H}$, is given by

$$\boldsymbol{\tau} = \mu_0(\boldsymbol{\mu} \times \boldsymbol{H}), \tag{1.3}$$

where μ_0 is the permeability of free space. Using the classical mechanics definition of torque, the rate of change of angular momentum, we can write

$$\boldsymbol{\tau} = \frac{\mathrm{d}\boldsymbol{J}}{\mathrm{d}t} = -\frac{1}{\gamma}\frac{\mathrm{d}\boldsymbol{\mu}}{\mathrm{d}t} = \mu_0(\boldsymbol{\mu} \times \boldsymbol{H}). \tag{1.4}$$

Now, if considering a system of magnetic moments, we can introduce the magnetisation,

$$\boldsymbol{M} = \frac{\sum \boldsymbol{\mu}}{V}, \tag{1.5}$$

where V is the volume of the sample. This leads us to the Landau-Lifshitz equation [46]

$$\frac{\mathrm{d}\boldsymbol{M}}{\mathrm{d}t} = -\mu_0\gamma(\boldsymbol{M} \times \boldsymbol{H}), \tag{1.6}$$

which describes the precession of the magnetisation around a magnetic field.

This equation does not account for any energy loss from the spin system; instead, the magnetisation precesses indefinitely. This is not physically realistic as the spin lattice and crystal lattice are coupled, as will be discussed in Section 1.3, which results in energy dissipation from the system, driving the precessing spins into alignment with the magnetisation. Therefore, a phenomenological damping term must be included, giving the Landau-Lifshitz-Gilbert equation (LLG) [47]

$$\frac{\mathrm{d}\boldsymbol{M}}{\mathrm{d}t} = -\mu_0\gamma\left(\boldsymbol{M} \times \boldsymbol{H}\right) + \frac{\alpha}{M_\mathrm{S}}\left(\boldsymbol{M} \times \frac{\mathrm{d}\boldsymbol{M}}{\mathrm{d}t}\right), \tag{1.7}$$

where the damping strength depends on the material-dependent Gilbert damping constant α, and M_S is the saturation magnetisation. The resulting spiralling motion induced by the damping term can be seen in Fig. 1.6.

The LLG equation is extremely successful in explaining the nonlinear dynamics of a system of spins from both a mathematical and a physical viewpoint, accommodating a wide array of dynamical structures, including spin waves [48].

1.2.3 Yttrium iron garnet

The Gilbert damping term discussed above is of fundamental importance when deciding on a suitable material in which to study spin waves. The vast majority of materials have such large Gilbert damping that observing propagating spin waves over a meaningful distance is not possible. Fortunately, there exist a number of materials with sufficiently low damping; perhaps the most popular of which is yttrium iron garnet (YIG), our material of choice.

YIG is a room-temperature ferrimagnetic insulator with extremely low Gilbert damping, exhibiting spin-wave propagation lengths of up to millimetres [49, 50]. YIG has a cubic crystal structure, lattice constant of $a_0 = 1.2376\,\mathrm{nm}$, and unit cells

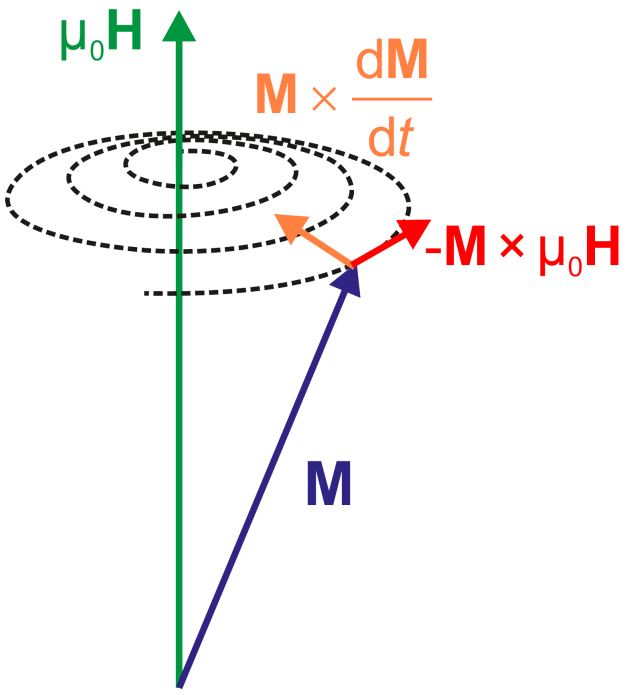

Figure 1.6: Diagram depicting the magnetisation dynamics of the Landau-Lifshitz-Gilbert equation. The effective magnetic field is shown by the green arrow around which the magnetisation, blue arrow, precesses according to the term shown by the red arrow. The additional damping term, in orange, causes the magnetisation to spiral inwards, aligning with the magnetic field; adapted from [6].

containing eight $Y_3Fe_2^{3+}(Fe_2^{3+}O_4^{2-})_3$ chemical formula units and, therefore, 160 atoms. The Fe^{3+} ions are the source of YIG's magnetism, with each containing a half-filled $3d$-orbital and, therefore, an angular momentum $J = S = 5/2$. The 40 Fe^{3+} ions per unit cell are divided into two antiferromagnetically coupled sublattices, giving rise to the ferrimagnetism, with each of the 16 Fe^{3+} ions in an octahedral O^{2-} environment and the remaining 24 Fe^{3+} ions in tetrahedral O^{2-} environments [51, 52]. Part of the unit cell is shown in Fig. 1.7, where the two Fe^{3+} environments are shown.

1.3 The magnetoelastic interaction of SAWs with spin waves

Having introduced SAWs and a material suitable for their generation, alongside spin waves and a material in which to observe their propagation, the missing piece of the puzzle is a method for coupling these two types of waves in a YIG/ZnO

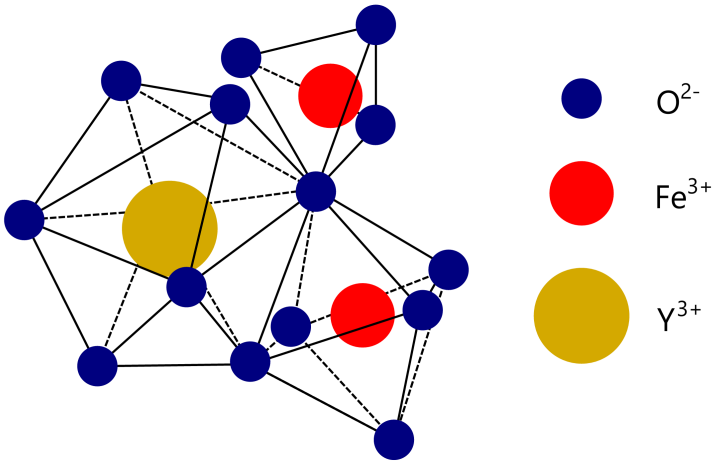

Figure 1.7: Diagram showing the crystal structure of yttrium iron garnet (YIG). The Fe^{3+} ions are the source of YIG's magnetism and are shown in their two different environments - an octahedral O^{2-} environment and a tetrahedral O^{2-} environment. Adapted from [53].

heterostructure.

As mentioned, one method for generating spin waves is to apply a microwave-frequency alternating current to a stripline antenna. According to Maxwell's equations, this current generates a perpendicular oscillating magnetic field in the antenna, which can apply torque to the magnetic moments, thus exciting a spin wave under the right conditions.

SAWs propagating in YIG will similarly generate a driving magnetic field that can apply torque to the magnetic moments by virtue of the magnetoelastic effect; where the magnetoelastic effect describes the coupling between the mechanical strains in the crystal lattice and the magnetic moments [54]. Therefore, instead of opting for the direct approach of current-driven magnon excitation, we can introduce an additional step by employing microwave-frequency electric fields to generate SAWs in a piezoelectric material. These SAWs then induce magnetoelastic driving fields to excite magnons. This interconversion scheme is illustrated in Fig. 1.8.

1.3.1 Possible origins of magnetoelasticity in YIG

Although the exact physical origin of the magnetoelastic interaction in YIG is unknown, three possible contributions are discussed below.

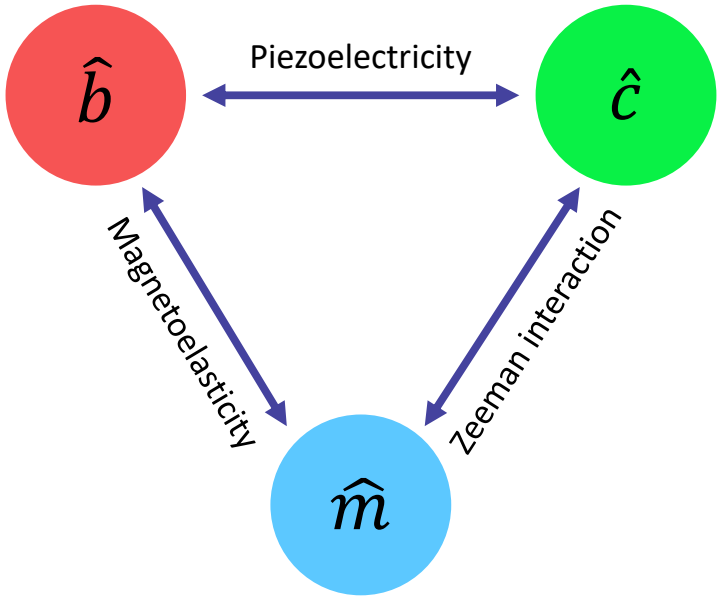

Figure 1.8: Diagram showing the interconversion between microwave photons, $\hat{c}$, phonons, $\hat{b}$, and magnons, $\hat{m}$. A direct conversion via the Zeeman interaction is possible; however, in addition, it is possible to convert microwave photons to phonons via the piezoelectric effect and then convert these phonons to magnons via the magnetoelastic effect. This indirect path is the subject of the first part of this thesis. Adapted from [55].

Crystal field strain anisotropy

When mechanical strain is applied to YIG, it induces a deformation in the crystal lattice structure. This deformation alters the interatomic distances and the bond angles, which affects the local environment experienced by the magnetic Fe^{3+} ions. Specifically, the distortion leads to a perturbation in the crystal field surrounding the Fe^{3+} S-state ions. As S-state ions are non-degenerate and have a symmetrical orbital charge distribution, their wavefunctions cannot mix on the application of the strain to minimise the electrostatic repulsion from the surrounding anions. However, mixing can occur for excited energy levels in the upper half of the $3d$-orbital. As the probability of such an excitation occurring is quite low, the magnetoelastic coupling is expected to be small. This agrees with experimental observations and is one of the reasons the spin-wave damping in YIG is exceptionally low.

Dipole-dipole interaction

The dipole-dipole interaction may also modulate YIG's magnetic properties in response to strain. When a strain is applied, the spin separation and, therefore, the dipole-dipole interaction energy are modulated, giving rise to a magnetoelastic interaction. Although this effect averages to zero in a perfect cubic lattice [56], the presence of the strain lowers the symmetry of the lattice and thus enables a small contribution to the magnetoelasticity from the modulation of the dipole-dipole energy.

Anisotropic exchange interaction

Finally, YIG exhibits anisotropic exchange interactions between neighbouring Fe^{3+} ions, meaning that the strength and directionality of the exchange interaction depends on the relative orientation of the neighbouring magnetic moments. When mechanical strain is applied to YIG, the overlap of the neighbouring Fe^{3+} wavefunctions is modified and, thereby, the strength of the exchange interaction. Therefore, the anisotropic exchange interaction also plays a role in the magnetoelastic coupling of YIG.

1.3.2 An empirical model of the magnetoelasticity in YIG

Despite the uncertain significance of each of these contributions to the magnetoelastic coupling in YIG, the magnetoelastic interaction can be described empirically as a perturbation of the magnetic system's total energy and, as such, approximated using a Taylor expansion.

Given that energy is even under time-reversal symmetry, while magnetisation is odd, the first-order energy terms in the expansion of the magnetoelastic coupling Hamiltonian, H_{me}, must be quadratic in magnetisation. Therefore, H_{me} can be expressed as

$$H_{me} = \sum_{i,j,k,l} \frac{b_{ijkl}}{M_S^2} M_i M_j S_{kl} + \sum_{p,q,r,s} \frac{a_{pqrs}}{M_S^2} \frac{\partial M_p}{\partial x_r} \frac{\partial M_q}{\partial x_s} S_{rs}, \tag{1.8}$$

where M_i are the components of the magnetisation, x_r the spatial components, and b_{ijkl} and a_{pqrs} the magnetoelastic coefficients [11, 57]. The strain tensor, S_{kl}, is given by

$$S_{kl} = \frac{1}{2}\left(\frac{\partial u_k}{\partial x_l} + \frac{\partial u_l}{\partial x_k}\right), \tag{1.9}$$

where u_k are the mechanical displacements. Note that in the literature, ε_{ij} is commonly used to express the strain in the context of magnetoelasticity; however, this notation is not adopted so as to avoid confusion with the permittivity tensor that will be introduced in Chapter 3.

As Eq. (1.8) must remain invariant under YIG's cubic crystal symmetry operations, the magnetoelastic coupling Hamiltonian can be greatly simplified, with the majority of terms being set to zero. In addition to this simplification, the terms involving spatial derivatives of magnetisation can also be neglected for typical spin wave experiments in the gigahertz regime due to their dependence on the wavenumber. This gives the following expression for the magnetoelastic coupling Hamiltonian

$$H_{me,\mathrm{YIG}} = \frac{b_1}{M_\mathrm{S}^2}\sum_i M_i^2 S_{ii} + \frac{b_2}{M_\mathrm{S}^2}\sum_{i\neq j} M_i M_j S_{ij}, \tag{1.10}$$

which has been well-verified experimentally [58, 59]. There are now only two magnetoelastic coefficients: the uniaxial term, described by b_1, which gives the change in length along an axis when a magnetic field is applied parallel to that axis; and the biaxial term, described by b_2, which gives the change in length along the two perpendicular axes to the direction of the applied magnetic field.

1.3.3 Physical considerations for achieving SAW-spin wave coupling

With a description of the magnetoelastic interaction in YIG in mind, one particularly important factor must be noted for a SAW-spin wave interconversion scheme to function. As energy and momentum must be conserved, the wavevector and frequency of the SAWs and spin waves must be well-matched for a linear conversion process.

Ferromagnetic resonance (FMR) occurs at the frequency at which the 'wavevector' is zero, indicating the uniform precession of all spins, and depends on the size of the external magnetic field. The FMR gives the point at which the spin-wave dispersion curves meet the y-axis in Fig. 1.2. Although thickness-dependent, in thin films of YIG, with an external magnetic field large enough to give an approximately uniformly magnetised film, the FMR frequency is typically a few gigahertz [60]. Given we expect a SAW velocity of $\sim$3000 ms^{-1} in ZnO [61], this means we require a SAW wavelength or IDT periodicity of $\sim$1 μm. This requirement for narrow IDT fingers prevented previous studies from observing the direct coupling of SAWs and spin waves in YIG/ZnO heterostructures [62, 63]. To overcome this, as we will discuss in Chapter 2, high-resolution electron beam lithography is required to pattern the IDTs.

Finally, we note that designing a system to hit the exact coupling point based on modelling would be challenging at best. Fortunately, however, the spin-wave dispersion relations are tunable with magnetic field strength. As the magnetic field around which the spins precess increases in magnitude, the frequency of precession increases. This is predominately a result of increased energy in the spin system stemming from the Zeeman effect.

Therefore, by sweeping an externally applied magnetic field, the spin-wave dispersion relation will vary in frequency, allowing the approximately linear SAW dispersion relation to match the spin-wave dispersion relation for the fixed excitation wavevector of the IDT. This process is illustrated in Fig. 1.9.

With this introduction in mind, we will return to discuss the mechanism of the SAW-spin wave coupling in depth in Chapter 4. Prior to this, the sample fabrication of, and SAW characterisation in, the YIG/ZnO heterostructure will be discussed in Chapters 2 and 3, respectively. Finally, a study of the samples using micro-focused Brillouin Light Scattering will be presented in Chapter 5.

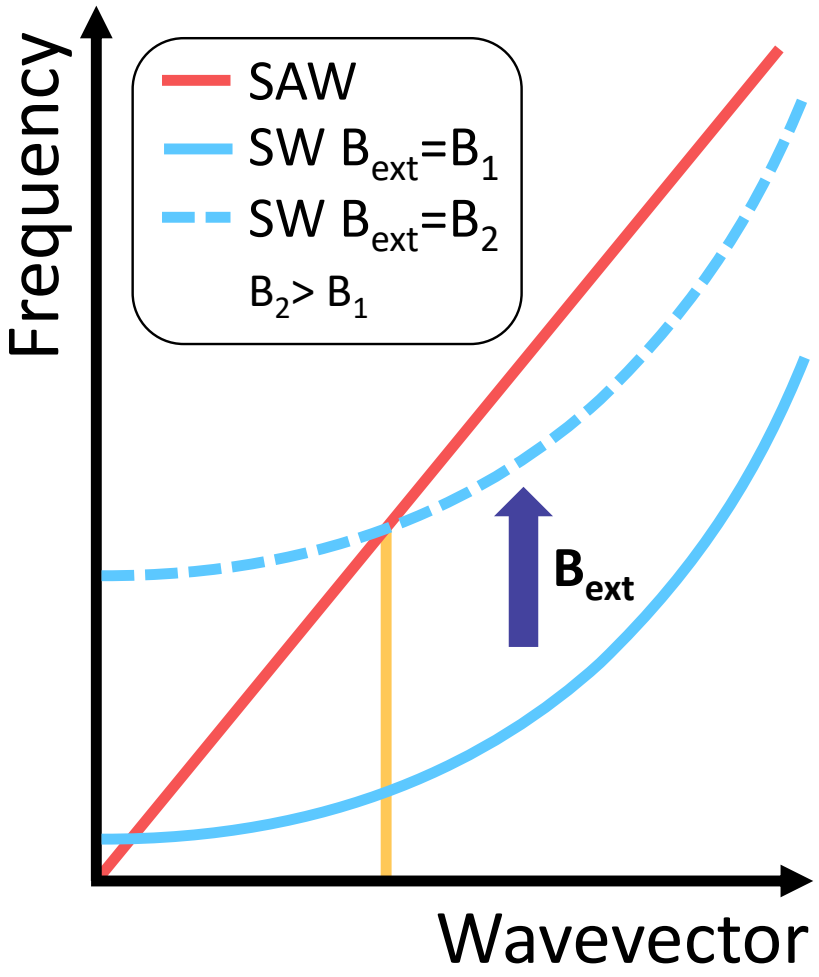

Figure 1.9: Schematic depicting the application of an external magnetic field to enable the coupling of SAWs and spin waves. The SAW dispersion relation, which is linear to first order, is shown in red. The fixed wavevector of an IDT is depicted in yellow, and the magnon dispersion relation is represented in blue. The dashed blue line shows the dispersion relation when the external magnetic field is increased compared to its value for the solid blue line. This allows the matching of the frequencies of the SAW and the spin wave for a fixed excitation wavevector, enabling the coupling.

2

Sample fabrication and characterisation

Two thin-film multilayer samples capable of exciting SAWs were prepared to study SAW-spin wave coupling. First, IDTs were fabricated via electron beam lithography on two YIG/GGG bilayers with different YIG thicknesses. Second, these were covered with piezoelectric ZnO films of slightly different thicknesses by radio frequency (RF) magnetron sputtering. Finally, chemical etching was employed to remove the ZnO from the contact pads of the IDTs. A schematic of the main steps and sample structure can be seen in Fig. 2.1. This chapter provides an in-depth description of the fabrication process and presents X-ray diffraction (XRD) results used to characterise the samples.

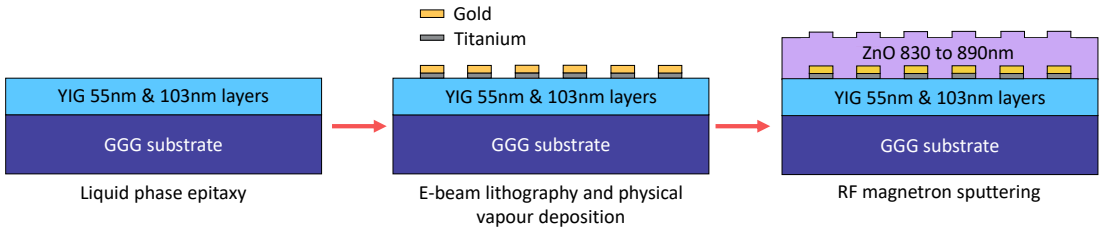

Figure 2.1: A schematic of the main sample preparation steps. The YIG layers were first grown on gadolinium gallium garnet (GGG) substrates by liquid phase epitaxy. Following this, IDTs were patterned by electron beam lithography on top of the YIG layer. These transducers had wavelengths of 2.8 μm and two different designs were fabricated with 6 and 20 finger pairs. After patterning, the samples were coated with a layer of piezoelectric ZnO by radio frequency magnetron sputtering.

2.1 Fabrication techniques

In this section, brief overviews of the most important fabrication techniques are provided, with a particular focus on the RF magnetron sputtering of the ZnO that took place in Oxford.

2.1.1 Liquid phase epitaxy

Liquid phase epitaxy (LPE) is a technique for growing thin films of high crystalline quality with precise control over thickness and composition. A substrate is dipped into a molten solution, or melt, containing the constituents of the thin film. To enable epitaxial growth, a substrate with a matching lattice structure is immersed in the molten solution, and atoms or molecules from the solution adhere to the substrate surface, forming a thin crystalline layer. The growth process is highly controlled, with parameters such as temperature, solution composition, and cooling rate carefully adjusted to achieve the desired thickness, composition, and crystal orientation of the thin film.

2.1.2 Spin coating

Spin coating is used to deposit thin layers of materials onto flat substrates with good control over thickness and uniformity. In the context of lithography, a small amount of resist in solvent is placed onto the centre of a substrate. This substrate is then spun rapidly, spreading the liquid over the surface; any excess liquid is expelled off the edges, leaving behind a thin, uniform film of the deposited material. The thickness of the resulting film can be controlled by adjusting parameters such as the viscosity of the solution, the spinning speed, and the duration of spinning. Once the substrate is coated, the sample is typically placed on a hot plate to evaporate the remaining solvents from the resist. Note that the uniformity of the coating at the substrate edges is typically poor.

2.1.3 Electron beam lithography

Electron beam lithography (EBL) is a patterning technique used to create features with sub-10 nm resolution. Electromagnetic lenses and deflection systems are used to precisely position and shape a beam of electrons. This focused electron beam is scanned across a resist-coated substrate, selectively exposing the resist layer in the desired patterns. Following exposure, the resist, commonly polymethyl methacrylate (PMMA), can be developed in a developer solution such as MIBK/IPA to remove the parts that were exposed, uncovering the substrate.

2.1.4 Electron beam evaporation

Electron beam evaporation is a physical vapour deposition technique for the fabrication of thin films with precise thickness control and high uniformity. An electron beam generated from an electron gun heats the material to be deposited in a vacuum chamber. The high-energy electron beam bombards the material source, causing it to evaporate. The vaporised material then condenses onto a substrate positioned in the deposition chamber, where it forms a thin film. A high vacuum environment ensures high-purity films and the deposition can be carefully controlled by adjusting parameters such as the beam current and substrate temperature.

2.1.5 Radio frequency (RF) magnetron sputtering

RF magnetron sputtering is a physical vapour deposition technique that involves the deposition of thin films by sputtering material from a target onto a substrate in a vacuum chamber. We will discuss the physics at play during the deposition and then describe the sputtering chamber used in Oxford, including the critical parameters to enable the successful deposition of ZnO.

Sputtering theory

RF magnetron sputtering takes place in a vacuum chamber, where the magnetron is located. A schematic of a magnetron can be seen in Fig. 2.2. To begin the

sputtering, the sputtering gas, typically argon, at pressures of order 10^{-2} mbar is allowed into the vacuum chamber.

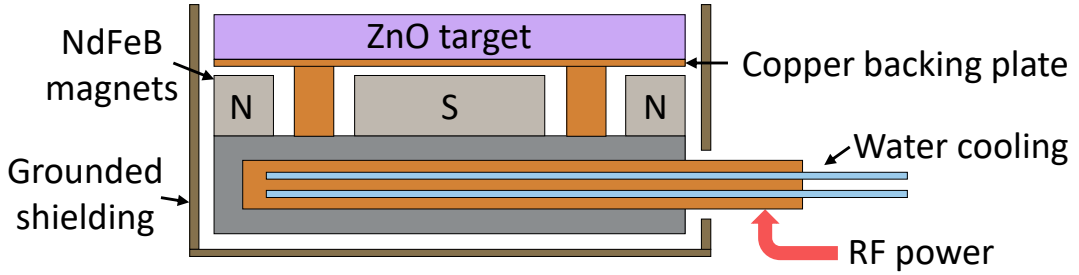

Figure 2.2: Schematic of the magnetron employed in Oxford. The magnetron is located in a vacuum chamber with the illustrated copper pipe, where the RF power is applied, passing through an insulated vacuum feedthrough to allow connection of the power and water cooling externally. The main body, in dark grey, is made from soft iron and water-cooled. Neodymium iron boron magnets, magnetised perpendicularly to the target surface, are used to provide the magnetic field required to trap free electrons. The RF power gives these electrons sufficient energy to ionise the sputtering gas. The ZnO target is bonded to a copper backing plate, which is mounted to the main body of the magnetron with a copper annulus. This ensures good thermal conductivity, keeping the target cool. Finally, the magnetron is surrounded by earthed brass shielding. Adapted from [64].

As can be seen, the magnetron has a central magnet with the south pole oriented upwards and an outer ring of magnets with the opposite polarity. This generates closed loops of magnetic flux between these magnets, providing a ring above the target in which any free electrons, usually generated by cosmic radiation, in the chamber, are confined. This region is known as the racetrack. These magnets are placed on the main body of the magnetron, which is made of a material with high magnetic permeability, such as soft iron, to minimise the magnetic flux leakage below the magnetron.

Once the sputtering gas has been let into the chamber, a high-power RF source is connected to the magnetron outside the chamber. The magnetron is electrically isolated from the chamber, and as such, the walls of the chamber are connected to the earth, completing the circuit. The RF source operates at 13.56 MHz with a power per target area typically on the order of 2 - 10 Wcm^{-2} required.

The application of the RF power gives rise to a time-varying electric field perpendicular to the surface of the target. This provides the confined electrons

with an oscillating kinetic energy in one dimension. As the electrons collide with the sputtering gas atoms, this energy is fed into the two other dimensions until sufficient energy is reached to allow an electron to ionise a sputtering gas atom. A chain reaction then occurs, creating a plasma discharge. As ions in the plasma de-excite, photons in the visible range are emitted, allowing the plasma to be observed. An example of this can be seen in Fig. 2.3. The colour of the plasma discharge depends on the gas composition and the pressure.

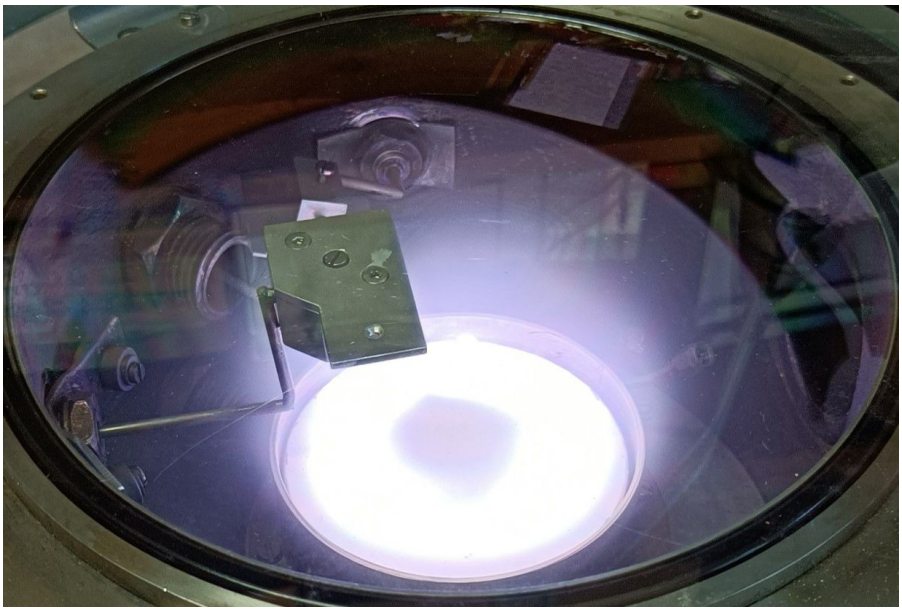

Figure 2.3: Photograph of the plasma formed while sputtering ZnO. The glowing ring indicates the racetrack region on the magnetron, around which the edge of the earthed brass shielding can be seen. The lilac colour of the plasma is as desired for the pressure and sputtering gas composition used to sputter ZnO. The aluminium substrate holder can be seen just below the glass plate above the magnetron on a rotatable sliding metal arm. This arm passes through an insulated electrical vacuum feedthrough to allow manipulation and connection to the RF power for pre-sputtering externally.

Although the RF potential oscillates between negative and positive values over the RF cycle, the target's average potential remains negative. This occurs because the electrons have a much higher mobility than the ions and, therefore, respond more readily to the applied electric field. During the positive portion of the cycle, the electrons are drawn towards the target, resulting in a higher electron density near the target surface. On the negative portion of the cycle, the ions cannot respond on a timescale fast enough to match this process, giving rise to the negative target bias.

This negative target bias ensures that the positive ions in the plasma are attracted towards the target surface during the sputtering process. These ions collide inelastically with the target, transferring sufficient kinetic energy to dislodge atoms or molecules from the target surface. This dislodging of the target material is known as 'sputtering'. Around the racetrack, the electron densities and, therefore, plasma densities are highest. The combination of this higher ion density and greater target negativity results in a greater rate of momentum transfer and, therefore, the highest sputtering rates occur around the racetrack.

As the momentum transfer process is inelastic, large amounts of heat are generated in the target. Therefore, targets are typically bonded with a thermally conductive material, such as indium, to a thin copper backing plate, and the entire magnetron is water-cooled, as shown in Fig. 2.2, to prevent damage, such as cracking, to the target. To minimise unwanted bombardment of the magnetron body, grounded shielding is used around the sides and bottom of the magnetron, as per the schematic in Fig. 2.2.

Once the target atoms and molecules are sputtered from the target, they are transported away from the target surface and deposited onto the nearby substrate. Typically, the minimum sputtering gas pressure to maintain a stable plasma discharge is used; this ensures the sputtered atoms and molecules undergo the minimum number of collisions on their path to the substrate, meaning the transport is approximately ballistic, which helps to promote high-quality thin film growth. The thin film properties, such as thickness, composition, and structure, can be controlled by adjusting parameters such as RF power, sputtering gas pressure and composition, target material composition, substrate temperature, and substrate to target distance.

Finally, we note that the impedance of the plasma is typically inductive [65] and requires matching to the resistive $50\,\Omega$ output impedance of a typical RF source to maximise the power transfer to the plasma. A circuit diagram of an example matching network is shown in Fig. 2.4.

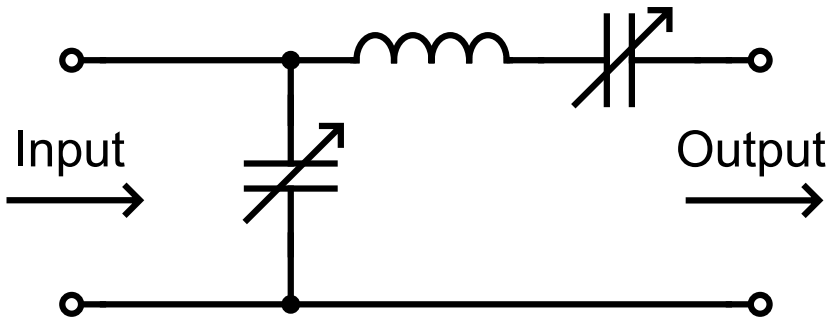

Figure 2.4: Circuit diagram of a matching network used for RF magnetron sputtering. To enable maximum power transfer, the capacitors can be tuned to allow impedance matching between the RF power source (input) and the plasma (output).

Sputtering ZnO

Zinc oxide can either be sputtered reactively with a zinc target and pure oxygen atmosphere to ensure the correct stoichiometry [40] or sputtered with a zinc oxide target and a sputtering gas mixture of argon and oxygen. Sputtering a pure zinc target is generally less favoured as the lower mass of the oxygen compared to argon means the sputtering rate is significantly reduced.

Reviewing the literature on RF magnetron sputtered piezoelectric ZnO films [41, 66–73] indicates that, as expected, using the minimum sputtering gas pressure to maintain a stable discharge leads to the highest quality c-axis aligned films, showing ballistic transport is important. In addition, when sputtering a pure ZnO target, the sputtering rate of the zinc atoms is greater than that of the oxygen atoms, and, therefore, a sputtering gas mixture of argon with oxygen is required to oxidise any remnant zinc atoms, ensuring the correct stoichiometry is achieved.

The ratio of the argon to oxygen in the sputtering gas mixture is important. Ratios between 1:1 and 4:1 of Ar:O_2 have been shown to produce piezoelectric films. One study trialled different ratios and found 3:1 to produce films with the best properties [41]; given this, and our group's previous successful use of a ratio of 1:1 [64], we chose to use a ratio of 2:1 when sputtering ZnO.

Finally, we note that the angle of the substrate relative to the target surface sets the angle of the piezoelectric c-axis of the ZnO [67, 68]. For an out-of-plane

c-axis, the substrate surface should be aligned parallel to the target surface.

The sputtering chamber and process

We used a small vacuum chamber dedicated to the sputtering of ZnO. A photograph of the magnetron and substrate holder in the chamber can be seen in Fig. 2.3, and a close-up of the substrate holder with a sample mounted prior to deposition in Fig. 2.5. A base pressure of 10^{-5} mbar can be achieved by the use of a diffusion pump backed by a rotary vane vacuum pump. The diffusion pump operates by heating a reservoir of oil at its base, causing it to evaporate. This forms a high-speed vapour jet that travels upwards and is then redirected downwards at an angle by baffles within the pump. Gas molecules present in the vacuum chamber are unable to diffuse against the vapour jet. Instead, they are carried downwards with the vapour flow and extracted by the rotary vane backing pump.

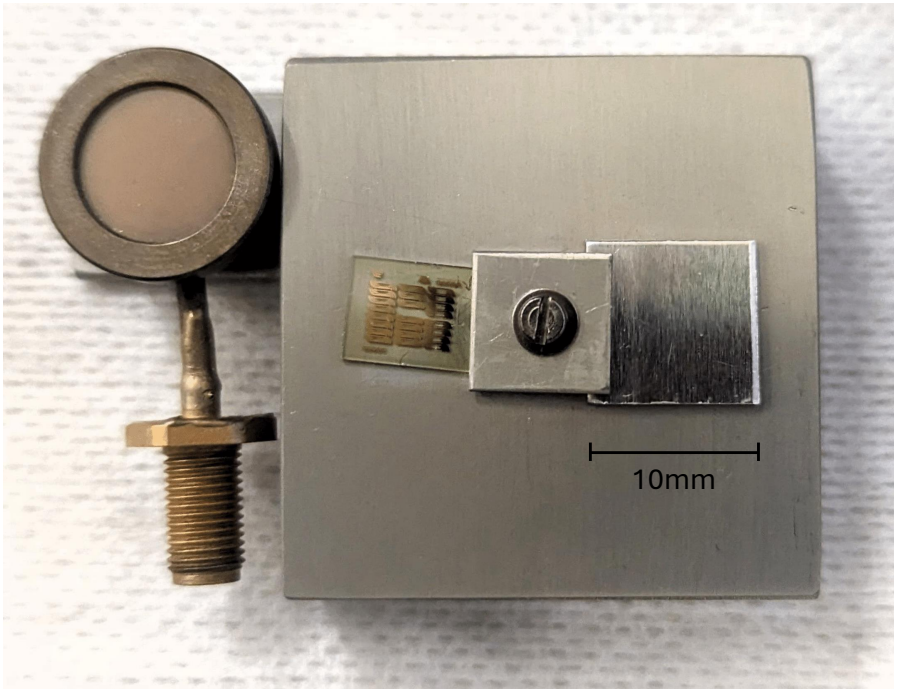

Figure 2.5: Photograph of a sample mounted to the aluminium substrate holder for sputtering. The gold IDTs can be seen on the YIG thin film to the left of the central mounting screw. An aluminium plate is used to the right of the YIG thin film to ensure the thin film remains flat when clamped. The circular disc to the left is the quartz thickness monitor.

Once sufficiently low base pressures are reached, the premixed argon and oxygen

sputtering gas mixture is let into the chamber via a leak valve. A pressure of approximately 4×10^{-3} mbar is used. The sputtering gas flow rate is reduced by partially closing a butterfly valve between the main chamber and the diffusion pump. Following this, an Advanced Energy AE RFX 600 RF source is connected to the substrate via the matching network to initiate a low-energy plasma discharge to sputter clean the substrate at 30 W, a process known as pre-sputtering. After pre-sputtering, the RF source is connected to the magnetron and used to initiate a full-powered plasma discharge. We use between 100 and 140 W, on the 89 mm diameter, 6.6 mm thick ZnO target and a substrate to target distance of 45 mm. The power levels are chosen based on literature values and the group's previous work [64].

Following a deposition, it is important to allow the sample to cool sufficiently for a few hours to avoid thermal shock when opening the chamber, which could result in damage to the ZnO film.

The removal of contaminants

Contaminants, such as oil or water, can outgas during the deposition, degrading the c-axis texture of ZnO films. The plant has several mechanisms built in to minimise this contamination.

Firstly, a liquid nitrogen cryopump prevents oil vapour from backstreaming into the chamber. Gas molecules that hit this trap condense, causing any rising oil vapour to return to the bottom of the trap. In addition, the cryopump aids in achieving a lower base pressure by similarly trapping gases and vapours in the main chamber - cryopumping the chamber. This is effective in removing water vapour.

Secondly, prior to any deposition, the chamber is heated with baking tape for approximately 6 hours. This encourages contaminants to evaporate, allowing them to be extracted or trapped.

Thirdly, a Peltier device on the input line of the sputtering gas cools the gas and helps to condense any water vapour that might be present.

Finally, the chamber has a Meissner trap. The trap consists of a coil of tubing which is filled with liquid nitrogen just before starting a deposition. Water vapour

will condense on this surface. This is another reason it is important to wait a few hours to return the chamber to atmospheric pressure after a deposition; if there is liquid nitrogen remaining in the Meissner trap, water in the atmosphere will condense on the trap when opening the chamber, increasing the time taken to pump down the chamber for the next deposition. Additionally, note that pure nitrogen gas should be used to return the chamber to atmospheric pressure.

Mass spectrometry is used to check there are no oil vapour contaminants present, and that water vapour is at an acceptably low level.

Measuring pressure

We employ two different methods to measure the base and sputtering gas pressures. An Edwards Penning gauge and a BALZERS IMG 060 B ionisation gauge.

Penning gauges are suitable for measuring pressures in the range of approximately 10^{-2} to 10^{-9} mbar. They emit electrons from a heated cathode filament, which are subsequently accelerated by a high voltage applied between the cathode and anode. When these electrons collide with gas atoms or molecules, they cause ionisation. The electric field attracts the positively charged ions towards the cathode, creating an ion current proportional to the gas pressure that can be measured. To increase sensitivity at lower pressures, a magnetic field perpendicular to the electric field is introduced. This causes the electrons to spiral towards the anode, increasing their path length and, therefore, the likelihood of ionising a gas molecule.

The BALZERS ionisation gauge works on a similar principle and over a similar pressure range; however, it uses a triode configuration. There is a hot cathode, a grid, and a collector plate. The electrons emitted from the cathode are attracted towards the helical grid, ionising gas atoms and molecules on their journey. These ions are then attracted to the collector plate, which is held at an intermediate potential, and the ion current is measured.

The main disadvantage of these two types of pressure gauges is that the ionisation current and, therefore pressure reading, depends on the composition of the gases.

Quartz monitor for estimating sputtering rates

Finally, a quartz thickness monitor, shown in Fig. 2.5, is used to calibrate the sputtering rate. Quartz is another piezoelectric material; therefore, with the correct oscillator circuit, a quartz disc can be made to vibrate at its resonance frequency. As material is deposited onto the quartz disc, the mass will increase, lowering the resonance frequency. By measuring this frequency change, the thickness of the deposited film and, therefore, the sputtering rate can be determined.

The following equation gives the thickness, t, in nanometres of a deposited thin film of ZnO on a quartz disc [74],

$$t = \frac{1000 \cdot N_{\mathrm{AT}} \cdot \rho_{\mathrm{quartz}}}{\pi \cdot \rho_{\mathrm{ZnO}} \cdot Z \cdot f_{\mathrm{f}}} \arctan\left(Z \tan\left(\frac{f_{\mathrm{i}} - f_{\mathrm{f}}}{f_{\mathrm{i}}}\pi\right)\right), \tag{2.1}$$

where f_{i} is the initial frequency in MHz before the deposition, f_{f} is the frequency after the deposition in MHz, and the Z-ratio is given by

$$Z = \sqrt{\frac{\rho_{\mathrm{quartz}}\mu_{\mathrm{quartz}}}{\rho_{\mathrm{ZnO}}\mu_{\mathrm{ZnO}}}}.$$

The values and definitions of the constants are given in Tab. A.1 in Appendix A.

2.2 Sample preparation

2.2.1 Prior to ZnO deposition

The two thin films of YIG used in this thesis were grown by LPE on a (111) oriented 500 μm GGG substrate [75]. Sample 1, a 103 nm film, was purchased from Matesy GmbH in Jena, Germany; Sample 2, a 55 nm film, was grown at INNOVENT e.V., Germany.

Prior to the IDT structuring process, the YIG thin films were cleaned with acetone and isopropanol in an ultrasonic bath at 35 kHz. Subsequently, a double resist layer consisting of PMMA 600K 4% and PMMA 950K 2% was spin-coated onto the YIG. The different resists result in an undercut after the EBL, which is needed for a successful lift-off process. An additional layer of Espacer300Z is applied to the PMMA surface in order to prevent surface charge-up effects during the EBL.

As discussed, to reach the gigahertz frequencies required to observe SAW-spin wave coupling, SAW wavelengths on the μm scale are required. To achieve this, a RAITH VOYAGER EBL system was used to fabricate IDTs with finger widths and separations of 700 nm ($\lambda = 2.8\,\mu$m), and an aperture size of 50 μm, remembering the IDT geometry shown in Fig. 1.4. Two different types of IDT were fabricated, one with 6 fingers and the other with 20 fingers. Following resist development, small PMMA residues that might remain in the mask grooves are removed via plasma ashing.

The sample was then covered with a 10 nm titanium, 80 nm gold stack using electron beam evaporation. After the electron beam evaporation of the two metals, the resist lift-off takes place using acetone in an ultrasonic bath, after which only the metal in the mask grooves, that is in contact with YIG, remains on the sample surface.

The IDT structuring process took place in collaboration with the Rheinland-Pfälzische Technische Universität Kaiserslautern-Landau (RPTU) in their Nano Structuring Center.

2.2.2 RF magnetron sputtering of ZnO

Following the IDT structuring process, the samples were covered with thin films of piezoelectric ZnO using the dedicated RF magnetron sputtering plant discussed in Section 2.1.5. A sample mounted prior to the deposition can be seen in Fig. 2.5. The samples were mounted in the chamber such that their surfaces were parallel to the target surface, promoting out-of-plane c-axis alignment. The base pressure in the sputtering chamber was 10^{-5} mbar, and the sputtering gas pressure was approximately 4×10^{-3} mbar. The samples were first pre-sputtered at 30 W for 5 minutes before sputtering was performed at power levels of 140 W for 80 minutes for Sample 1 and 100 W for 115 minutes for Sample 2.

2.2.3 Post ZnO deposition

The insulating ZnO also covered the contacting pads of the IDTs and, therefore, needed to be removed to allow direct electrical contact. This was accomplished

by creating an etch mask consisting of AZ5214E photoresist. Following resist development under ultraviolet light, the sample was immersed in a 32% HCl solution for a few seconds, removing the ZnO from the contact pads. Note that capacitive coupling to the contact pads is possible; however, we found that direct electrical contact greatly enhanced the SAW signals.

The ZnO film thicknesses were measured using a profilometer and found to be 890±25 nm for Sample 1 and 830±25 nm for Sample 2. The relatively large errors in the thickness result from a combination of surface defects and non-uniformity in the thickness due to the sputtering process; to increase the accuracy, we averaged 5 measurements of the thickness taken close to the IDTs used to excite SAWs in the experimental measurements.

2.3 The final sample structures

A schematic of the final layer structures of the two samples and a microscope image of one of the IDTs can be seen in Fig. 2.6. The thicknesses of the layers of Sample 1 and Sample 2 can be found in Tab. 2.1.

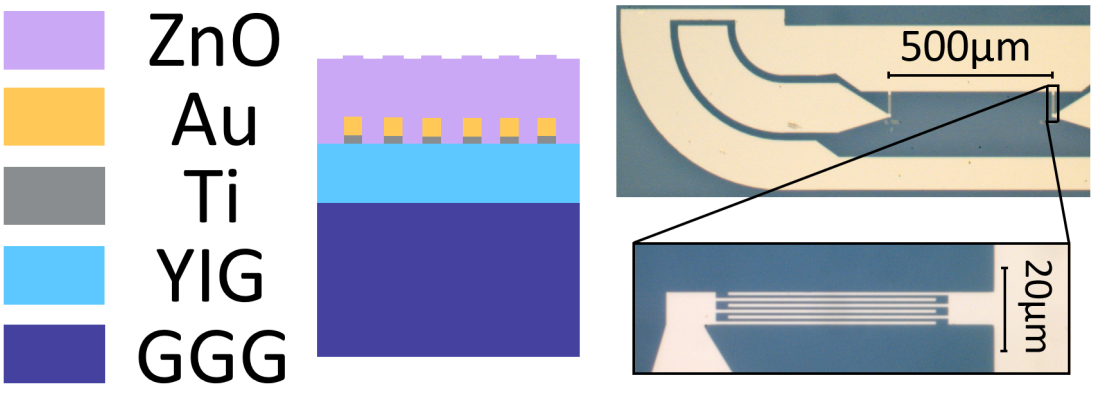

Figure 2.6: Left: schematic of the sample structure showing the layers in the structure and the position of the embedded IDTs. Right: microscope image of one of the samples, a gold IDT structure can be seen as the lighter colour with the 6 finger IDT highlighted by the inset. The central pad is the signal pad, and the outer pad, which surrounds the signal pad to minimise stray fields, is the ground pad.

Table 2.1: The thicknesses of the material layers and IDTs of the two samples.

Sample	GGG	YIG	IDT		ZnO
			Ti	Au	
Sample 1	500 μm	103nm	10nm	80nm	890nm
Sample 2	500 μm	55nm	10nm	80nm	830nm

2.4 X-ray diffraction characterisation

In the following sections, we build on results from the group's previous work as laid out in Fung's thesis [64]. The reader can find a thorough discussion of the use of XRD to study ZnO sputtered samples in that thesis, and as such, only a brief overview is given here.

2.4.1 Theoretical overview

XRD characterisation is based on the principle of Bragg reflection. When an X-ray beam interacts with the regularly spaced atomic planes within a crystal lattice, it can undergo constructive interference. This phenomenon is described by Bragg's law, which states that for a given angle, θ, between the incoming X-ray beam and the lattice planes, and X-ray wavelength, λ, constructive interference occurs when the path difference between waves scattered from adjacent atomic planes is an integer multiple of the wavelength. This can be expressed mathematically by,

$$n\lambda = 2d\sin\theta, \tag{2.2}$$

where d is the spacing between adjacent crystal planes and n is an integer representing the order of the reflection.

We have used two different types of XRD scans in this thesis: $\theta/2\theta$ scans and ω scans, also known as rocking curves. A $\theta/2\theta$ scan is a coupled scan in which both the sample bed and detector move simultaneously so that $\theta = \omega$, where ω is the angle between the sample bed and the incident X-ray beam, and 2θ is the angle between the incident X-ray beam and the detector. The resulting diffraction peaks in the diffraction pattern occur due to the constructive interference mentioned, and correspond to specific crystallographic planes within the thin film structure.

For rocking curves, the value of 2θ is fixed to satisfy the Bragg condition for the lattice plane of interest. The sample bed is then rocked, varying the angle ω. The area under the rocking curve is proportional to the number of crystallites that are approximately aligned in the film, and the width gives an indication of how well-aligned the crystallographic planes of the crystallites are.

2.4.2 Experimental results

Piezoelectric ZnO with a hexagonal wurtzite structure and out-of-plane c-axis has a characteristic $\theta/2\theta$ peak at approximately 34.4° arising from reflections off the (002) lattice plane [72, 73]. We note that although this peak confirms the alignment of the c-axis, it gives no indication as to the orientation of the electric dipoles, meaning it is possible that a seemingly perfect sample could have an equal number of oppositely oriented electric dipoles such that there is no net piezoelectric action. The only way to confirm this is not the case is by direct measurement of SAWs.

$\theta/2\theta$ scans were taken of both of the samples with a Rigaku SMARTLab diffractometer. In both samples, peaks at approximately 34.4° were observed. The results for Sample 1 can be seen in Fig. 2.7. We can also see the ZnO (004) peak at about 73° arising from second-order Bragg diffraction from the (002) plane. There is also a clear GGG substrate peak from the (444) plane at approximately 51°, and corresponding (222) GGG reflection at about 25° [76].

2.4.3 The 'dead layer'

In Fung's work, a dead layer of ZnO, where the c-axes are not aligned, was found to exist in the sputtered films. This dead layer was identified by sputtering a thickness series of ZnO on sapphire substrates and measuring the rocking curves for these samples. As mentioned, the area under the rocking curve is proportional to the total volume of the approximately aligned c-axis crystallites. This was measured for the thickness series, and by plotting the thickness against the area, a straight line with an x-axis intercept at approximately 200 nm was found to fit the data.

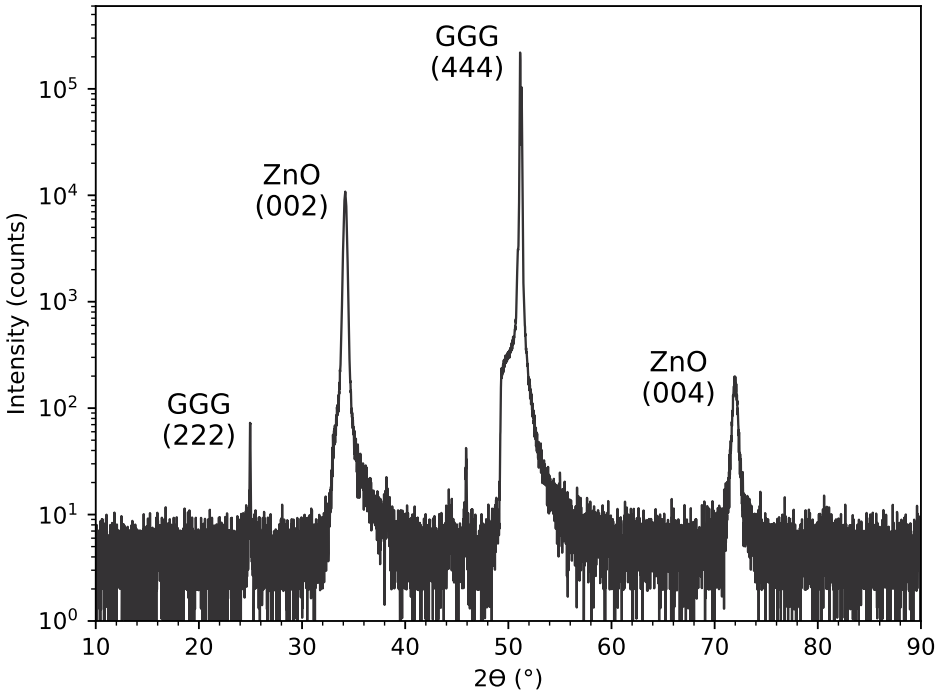

Figure 2.7: $\theta/2\theta$ X-ray diffraction pattern for Sample 1. There is a pronounced substrate peak from the GGG at approximately 51°. The Bragg diffraction peak from the ZnO (002) plane can also be seen at 34° with the second-order (004) peak at 73°, indicating the successful deposition of ZnO on YIG with an out-of-plane c-axis. A small peak at 25° corresponding to the (222) GGG reflection is also visible.

This indicated there was an approximately 200 nm thick layer of ZnO with no c-axis alignment. The so-called 'dead layer'.

Fung's study concluded that the sputter deposition of ZnO followed a 'survival of the fastest' growth mechanism. In this case, the surface mobility is low but still sufficient to allow adsorbed atoms to diffuse within the grains. At the beginning of the deposition, all possible orientations of ZnO can grow, producing the amorphous dead layer. However, as the deposition goes on, the (0001) planes, with an out-of-plane c-axis, have the highest surface energy and, therefore, a faster vertical growth rate; as such, they grow at the expense of planes with lower surface energy, leading to the c-axis aligned columnar grain structures observed in ZnO sputtered films [77].

Based on this, we grew a thickness series of 3 samples of ZnO (200, 470, and 740 nm) sputtered at 100 W on glass substrates, alongside a sample of 960 nm ZnO sputtered on unpatterned YIG. The rocking curves for the samples in the thickness

series were measured and fitted to a Gaussian distribution of the form

$$Ae^{-\frac{(x-\mu)^2}{2\sigma^2}} + y_0, \tag{2.3}$$

where A, μ, σ, and y_0 are constants. The area under the curve was then calculated using the formula $\sqrt{2\pi}\sigma A$, alongside an associated error calculated from the fitting errors of A and σ. The ZnO film thickness as a function of the area under the rocking curves, proportional to the total volume of the approximately aligned c-axis crystallites, is shown in Fig. 2.8 by the green points. These points were fitted to a straight line (dark blue), which intercepts the x-axis at 200 nm, consistent with the previous study and the presence of a 200 nm dead layer of ZnO.

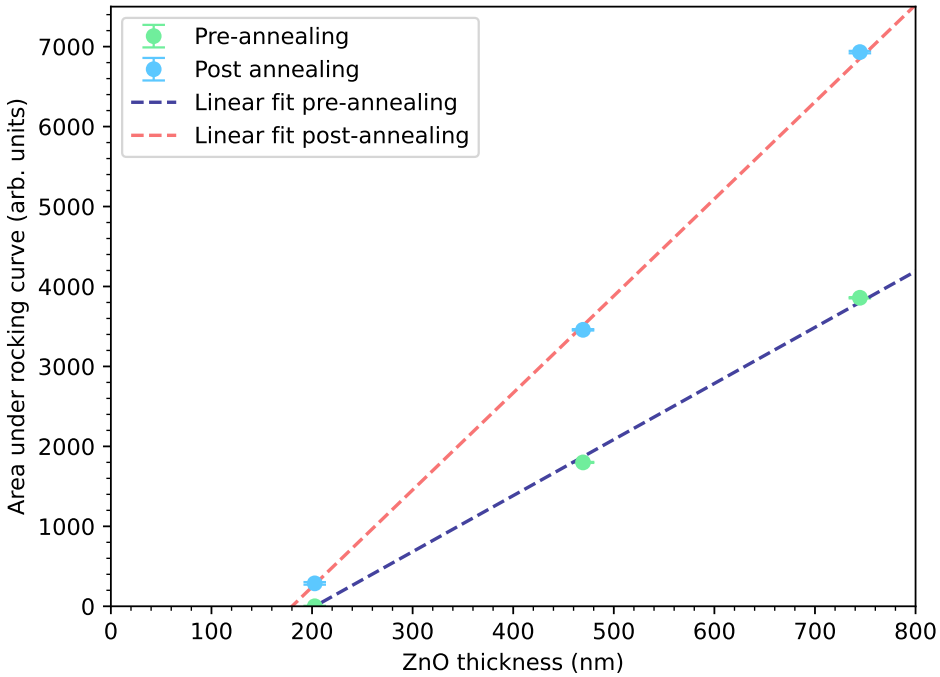

Figure 2.8: ZnO film thickness as a function of the area under the rocking curve for a thickness series of three ZnO films sputtered on glass substrates. The green points show the rocking curve areas before annealing the samples, while the light blue points show the rocking curve area post-annealing at 350°C in air for two hours. Straight line fits to the data pre-annealing (dark blue) and post-annealing (red) are shown. The annealing process has increased the area under the rocking curves in all three samples, although the x-axis intercept (indicating the dead layer thickness) is only decreased by 20 nm.

2.4.4 Annealing

Based on previous studies [72, 73], using either a heated substrate or annealing samples post-deposition can increase the c-axis alignment of thin films of sputtered ZnO. This makes sense, as increasing the substrate temperature would increase the adsorbed atom mobility, thus increasing diffusion within the grains and, therefore, the rate at which the c-axis aligned grains can outpace the growth of unaligned grains. Equally, annealing can provide additional energy to allow a reordering of the crystal structure into a lower energy configuration.

As annealing is easier to realise, we attempted annealing in air at 350°C for two hours. The temperature was ramped up and down at a rate of 50°C per hour. We found that the annealing consistently led to an increase in the ZnO (002) peak height, indicating an increase in the c-axis alignment of the samples. An example $\theta/2\theta$ scan for a 200 nm thick ZnO sample sputtered on glass can be seen in Fig. 2.9, where the X-ray intensity before annealing is shown in blue and after annealing in red. Firstly, we note that there is practically no alignment of the c-axis before annealing, confirming the presence of the approximately 200 nm dead layer. Secondly, we see the enhancement in the (002) peak post-annealing.

The rocking curves and corresponding areas under the curves were also measured post-annealing, shown by the light blue points in Fig. 2.8. As can be seen, the increase in area for the 200 nm sample is small. Furthermore, fitting a straight line, shown in red, to the data gives an x-intercept of 180 nm, indicating that annealing cannot be used to reduce the dead layer thickness significantly. However, the gradient of the line compared to the pre-annealing value is increased by a factor of 1.7, showing that the annealing is quite effective at increasing c-axis alignment. Note that electrical measurements would be required to confirm whether the annealing also results in an increase in the electromechanical coupling coefficients. Also note that for temperatures below 350°C, no improvement in the alignment was found.

Following this, annealing of the unpatterned YIG/ZnO thin film was attempted. Unfortunately, the 960 nm ZnO film was visibly damaged due to the annealing, with the appearance of small pin-sized holes observed on the sample. This is likely due

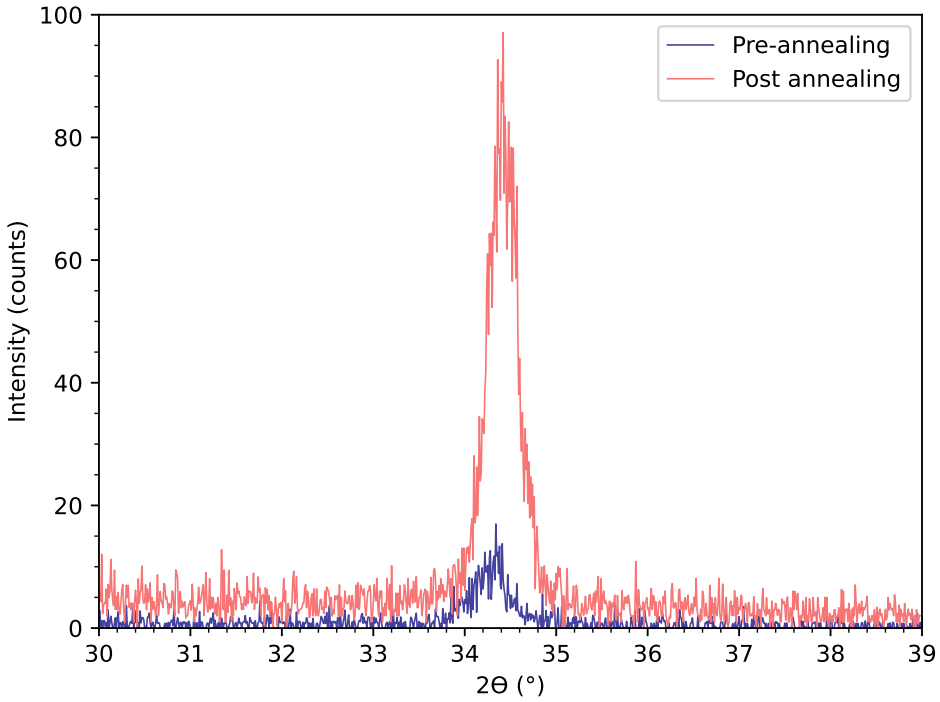

Figure 2.9: $\theta/2\theta$ X-ray diffraction pattern of a 200nm ZnO layer sputtered at 140 W onto glass before (blue) and after (red) annealing. The (002) peak at 34.4° before annealing shows only 10 counts, indicating a lack of c-axis alignment and, therefore, the presence of an approximately 200 nm dead layer of ZnO. The peak post-annealing has increased in size, indicating some improvement to the c-axis alignment; however, the peak is still relatively small, showing annealing cannot be used to eliminate the dead layer of ZnO.

to a combination of stresses in the ZnO film and the lattice mismatch between the cubic YIG and the hexagonal ZnO, which is different from the amorphous glass. After the sample is heated, the stresses in the film are increased by the improved c-axis alignment and, on cooling, are sufficient to cause the ZnO film to crack.

So, while annealing may be useful in some cases to improve the c-axis alignment, this technique does not work for YIG/ZnO layers of this thickness. It is possible that increasing the thickness of the ZnO would sufficiently relax the film so it does not crack during annealing. However, as the SAW amplitude exponentially decays with distance from the surface, any benefit is likely to be outweighed by a decreased amplitude and, therefore, magnetoelastic driving field in the YIG layer.

As the dead layer appears to be inherent to the RF magnetron sputtered films of ZnO, it needs to be accounted for in any modelling of the samples. This will be discussed in Section 3.3.

3

Calculating SAW properties in thin film multilayers

In this chapter, a model to predict the properties of SAWs in thin-film multilayers is developed. The dispersion relations, group velocities, and electromechanical coupling coefficients of the SAWs in multilayers of YIG/ZnO on GGG substrates are calculated. Finally, some thoughts are given on the tunable properties of ZnO and their effect on the SAW characteristics.

3.1 The mathematical model

The model presented here follows the methodology of Farnell and Adler [78], giving a relatively simple technique to numerically calculate the SAW properties in a multilayer system. The main advantage of this method is that it does not rely on computationally intensive finite-element modelling software. Although this software might produce more accurate results, as we will later show, our method is sufficient, within the assumptions made, to accurately interpret our experimental data.

The relevant geometry of the thin-film multilayer structures can be seen in Fig. 3.1, where a two-layer YIG/ZnO thin film on a GGG substrate is shown. $\boldsymbol{x_3}$ is the direction normal to the surface, with the interface between the first layer and the substrate at $x_3 = 0$, and a total YIG/ZnO film layer thickness given by

$x_3 = h$. The GGG substrate is assumed to extend to $+\infty$ in the $-\boldsymbol{x_3}$ direction, and the layers are assumed to extend to $+\infty$ in the $\pm\boldsymbol{x_1}$ and $\pm\boldsymbol{x_2}$ directions. The waves propagate in the $\boldsymbol{x_1}$ direction. Note that this model can be easily extended to any similar system of n-layers.

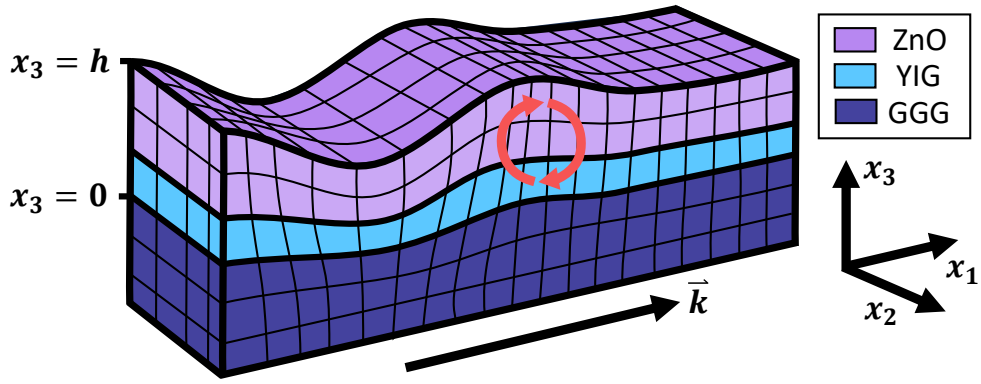

Figure 3.1: Schematic of the geometry of the thin film structures used in the numerical model. Thin layers of YIG and ZnO on a GGG substrate are shown. The direction of wave propagation and the coordinate system are indicated by $\boldsymbol{k}$, $\boldsymbol{x_1}$, $\boldsymbol{x_2}$, $\boldsymbol{x_3}$. A Rayleigh wave is shown propagating in the $\boldsymbol{x_1}$ direction, where the red arrows indicate the characteristic elliptical motion of the lattice in the $\boldsymbol{x_1}$, $\boldsymbol{x_3}$ plane. The YIG/GGG interface is at $x_3 = 0$, and the ZnO free surface is at $x_3 = h$.

The equations of motion for a piezoelectric material are given by

$$\begin{aligned} \rho\frac{\partial^2 u_j}{\partial t^2} =& c_{ijkl}\frac{\partial^2 u_k}{\partial x_i \partial x_l} + e_{kij}\frac{\partial^2 \phi}{\partial x_i \partial x_k} \\ e_{ikl}\frac{\partial^2 u_k}{\partial x_i \partial x_l} =& \epsilon_{ik}\frac{\partial^2 \phi}{\partial x_i \partial x_k}, \end{aligned} \tag{3.1}$$

where u_j are the mechanical displacements, ϕ the electric potential, ρ the density, and c_{ijkl}, e_{kij} and ϵ_{ik} the elastic, piezoelectric, and permittivity tensors respectively.

As we are looking for SAWs, we propose the ansatz

$$\begin{aligned} u_j &= a_j e^{ikbx_3} e^{ik(x_1 - vt)} \\ \phi &= a_4 e^{ikbx_3} e^{ik(x_1 - vt)}, \end{aligned} \tag{3.2}$$

where we have a wave of amplitude a_j propagating in the x_1 direction with wavevector k and phase velocity v. The exponentially decaying component in the x_3 direction, with complex coefficient b, gives the SAW characteristic. Substituting this ansatz

into the equations of motion yields the Christoffel equation

$$\begin{pmatrix} \Gamma_{11}-\rho v^2 & \Gamma_{12} & \Gamma_{13} & \Gamma_{14} \\ \Gamma_{12} & \Gamma_{22}-\rho v^2 & \Gamma_{23} & \Gamma_{24} \\ \Gamma_{13} & \Gamma_{23} & \Gamma_{33}-\rho v^2 & \Gamma_{34} \\ \Gamma_{14} & \Gamma_{24} & \Gamma_{34} & \Gamma_{44} \end{pmatrix} \begin{pmatrix} a_1 \\ a_2 \\ a_3 \\ a_4 \end{pmatrix} = 0. \tag{3.3}$$

Γ_{ij} are given by quadratic equations in b with components of the elastic, piezoelectric, and permittivity tensors as the coefficients.

For a nontrivial solution, the determinant of the matrix in Eq. (3.3) must be zero; therefore, for each value of v, there is an eighth-order polynomial in b to solve. The amplitude coefficients, a_j, can then be found by solving Eq. (3.3) for each solution of b; giving a solution that is a superposition of partial waves

$$\begin{aligned} u_j &= \sum_m C_m a_j^{(m)} e^{ikb^{(m)}x_3} e^{ik(x_1-vt)} \\ \phi &= \sum_m C_m a_4^{(m)} e^{ikb^{(m)}x_3} e^{ik(x_1-vt)}, \end{aligned} \tag{3.4}$$

rather than the simple monochromatic wave proposed in Eq. (3.2).

As we are considering thin layers, where the wavelengths are comparable to the thicknesses, all the solutions of $b^{(m)}$ are taken, such that the index m runs from 1 to 8. However, in the substrate, only the $b^{(m)}$ in the lower half of the complex plane are considered, as the wave must vanish as $x_3 \to -\infty$, hence the index m runs from 1 to 4. Therefore, in total, the index m runs from 1 to 8×(number of layers)+4.

The solutions found thus far only give the relations between $b^{(m)}$, $a_i^{(m)}$, and v. As we are interested in the dispersion relations, we must additionally consider the boundary conditions. To do so, we use the linearised coupled strain-charge equations

$$\begin{aligned} T_{ij} &= c_{ijkl} S_{kl} - e_{kij} E_k \\ D_i &= e_{ikl} S_{kl} + \epsilon_{ik} E_k, \end{aligned} \tag{3.5}$$

where T_{ij} is the stress tensor, S_{kl} the strain tensor, E_k the electric field, and D_k the electric displacement with

$$S_{kl} = \frac{1}{2}\left(\frac{\partial u_k}{\partial x_l} + \frac{\partial u_l}{\partial x_k}\right) \quad \text{and} \quad E_k = -\frac{\partial \phi}{\partial x_k}. \tag{3.6}$$

At each layer interface, u_j, ϕ, D_3, T_{23}, T_{13}, and T_{33} are continuous, giving 8 boundary condition equations. At the free surface, there is no restriction on the

mechanical displacements, while the same three stress components are zero, and D_3 is again continuous, giving four boundary condition equations. Therefore, in total, there are 8×(number of layers)+4 boundary condition equations.

Substituting Eq. (3.4) into the boundary condition equations gives linear equations in the relative amplitudes C_m, and hence can be written in the form of a matrix equation

$$BC_{pm}C_m = 0, \tag{3.7}$$

where BC_{pm} is the boundary condition matrix and the index p runs over the boundary condition equations. As before, for nontrivial solutions, the determinant of BC_{pm} must be zero. Solving this equation gives the phase velocity of the structures in terms of the wavevector, from which the dispersion relation and group velocity can be easily determined, $v = \omega/k$ and $v_g = \frac{\partial\omega}{\partial k}$, where ω is the angular frequency and v_g the group velocity. Note that the group velocity is determined by numerically calculating the gradient.

In addition to these relations, we can also find the electromechanical coupling coefficients, K, which are given by [27]

$$K^2 = 2\left(1 - \frac{v_{\text{metalised}}}{v_{\text{free}}}\right), \tag{3.8}$$

where v_{free} is the phase velocity previously calculated, and $v_{\text{metalised}}$ is the phase velocity calculated with an infinitesimally thin perfect conductor layer at the position of the IDT. This metallic film modifies the boundary conditions such that the electric potential, ϕ, at the conductor is zero. If the film is on the free surface, the size of the boundary condition matrix is unchanged, whereas, in the case of an interlayer IDT, an additional 8 equations must be added. K^2 gives an estimate of the conversion efficiency between electrical and acoustic energy.

Finally, by solving Eq. (3.7), the relative amplitudes, C_m, of the partial waves can be calculated. With all the coefficients calculated, Eq. (3.4) can then be solved to find the normalised mechanical displacements as a function of depth. From these, the strains can be calculated using Eq. (3.6).

3.1.1 Material properties

In order to calculate the numerical solutions, a large number of material properties are required for each layer. Namely, the density, ρ; elastic constants, c_{ijkl}; piezoelectric constants, e_{kij}; and permittivities, ϵ_{ik}. The material properties used in the numerical calculation are given in Tab. A.2 in Appendix A.

3.1.2 Rotating crystallographic axes

The literature values of the material properties are defined for a particular crystallographic direction. Therefore, it is typically necessary to rotate the crystallographic axes to find the correct values of the material parameters for the crystal orientation of the thin film sample in question. Practically, this involves rotating the permittivity, piezoelectric, and elastic tensors.

To do so, Eq. (3.5) should be considered in the matrix form using the fact that the strain, stress, and piezoelectric tensors are symmetric. Voigt notation gives a way to represent a symmetric tensor by reducing its order, such that the strain and stress tensors are reduced to 6×1 vectors, the elasticity tensor to a 6×6 matrix, c, and the piezoelectric tensor to a 6×3 matrix, e.

If we consider an arbitrary rotation α about $\boldsymbol{x_1}$, followed by β about $\boldsymbol{x_2}$, and finally γ about $\boldsymbol{x_3}$ we find the 3x3 rotation matrix

$$a = \begin{pmatrix} \cos\gamma & -\sin\gamma & 0 \\ \sin\gamma & \cos\gamma & 0 \\ 0 & 0 & 1 \end{pmatrix} \begin{pmatrix} \cos\beta & 0 & \sin\beta \\ 0 & 1 & 0 \\ -\sin\beta & 0 & \cos\beta \end{pmatrix} \begin{pmatrix} 1 & 0 & 0 \\ 0 & \cos\alpha & -\sin\alpha \\ 0 & \sin\alpha & \cos\alpha \end{pmatrix} = \begin{pmatrix} a_{11} & a_{12} & a_{13} \\ a_{21} & a_{22} & a_{23} \\ a_{31} & a_{32} & a_{33} \end{pmatrix}.$$

The corresponding 6x6 rotation matrix is given by [27]

$$M = \begin{pmatrix} a_{11}^2 & a_{12}^2 & a_{13}^2 & 2a_{12}a_{13} & 2a_{13}a_{11} & 2a_{11}a_{12} \\ a_{21}^2 & a_{22}^2 & a_{23}^2 & 2a_{22}a_{23} & 2a_{23}a_{21} & 2a_{21}a_{22} \\ a_{31}^2 & a_{32}^2 & a_{33}^2 & 2a_{32}a_{33} & 2a_{33}a_{31} & 2a_{31}a_{32} \\ a_{21}a_{31} & a_{22}a_{32} & a_{23}a_{33} & a_{22}a_{33}+a_{23}a_{32} & a_{21}a_{33}+a_{23}a_{31} & a_{22}a_{31}+a_{21}a_{32} \\ a_{31}a_{11} & a_{32}a_{12} & a_{33}a_{13} & a_{12}a_{33}+a_{13}a_{32} & a_{13}a_{31}+a_{11}a_{33} & a_{11}a_{32}+a_{12}a_{31} \\ a_{11}a_{21} & a_{12}a_{22} & a_{13}a_{23} & a_{12}a_{23}+a_{13}a_{22} & a_{13}a_{21}+a_{11}a_{23} & a_{11}a_{22}+a_{12}a_{21} \end{pmatrix}.$$

The permittivity, piezoelectric, and elastic tensors are then transformed according to

$$\epsilon' = a\epsilon a^T, \quad e' = aeM^T, \quad c' = McM^T. \tag{3.9}$$

3.2 Using the model to calculate SAW properties

We now have all the required tools to calculate the dispersion relations for thin-film multilayers. Practically, this involves proposing an initial guess for k at a fixed v; if a solution for k is then converged upon, we continue to make small steps in v over a predefined range, finding $k(v)$. The dispersion relation is then calculated numerically from $v = \omega/k = 2\pi f/k$, where f is the frequency. The calculation is undertaken in MATLAB, although Python would be equally suitable.

Note that the abrupt endpoints of all the following curves calculated using this model result from the modelling itself. The start and end points of the phase velocity are chosen over a fixed range, which defines the endpoints of the curves. Setting such a range is necessary to ensure the model converges on only one solution.

In this section, results are calculated for Sample 1 with the geometry shown in Fig. 3.1, remembering this sample has an 890 nm thick layer of ZnO and a 103 nm layer of YIG, the GGG substrate is taken to be infinite in accordance with the model. The GGG and YIG are oriented with the (111) direction normal to the film and the $(11\bar{2})$ direction aligned with the SAW propagation direction. The ZnO c-axis is normal to the film, and the dead layer is neglected.

In Fig. 3.2, the dispersion relations calculated for Sample 1 over a range of 8 GHz in frequency are shown. First, note the deviation from the simple first-order approximation of a linear dispersion relation, shown by the subtle curvature. Second, it can be seen that there are multiple solutions. These solutions can be grouped into two classes depending on the type of particle displacement induced.

The first are the 'Rayleigh modes', which result in an elliptical particle motion in the $\boldsymbol{x_1}$, $\boldsymbol{x_3}$ plane for isotropic materials [26, 78], as previously shown schematically in Fig. 3.1 by the red arrows. Note that due to the anisotropic layered structures, there

is additional particle motion [78]; hence, we use the term 'Rayleigh-like'. The zeroth-order mode, shown by the blue line, always exists in the structure. By contrast, the higher-order Rayleigh-like modes, known as the 'Sezawa' modes, are only introduced when the shear wave speed in the layer exceeds that of the substrate [79]. The green line shows the first-order Sezawa-like mode. For simplicity, throughout the rest of this thesis, the zeroth-order Rayleigh-like mode will be referred to as the Rayleigh-like mode and the higher-order mode as the Sezawa-like mode.

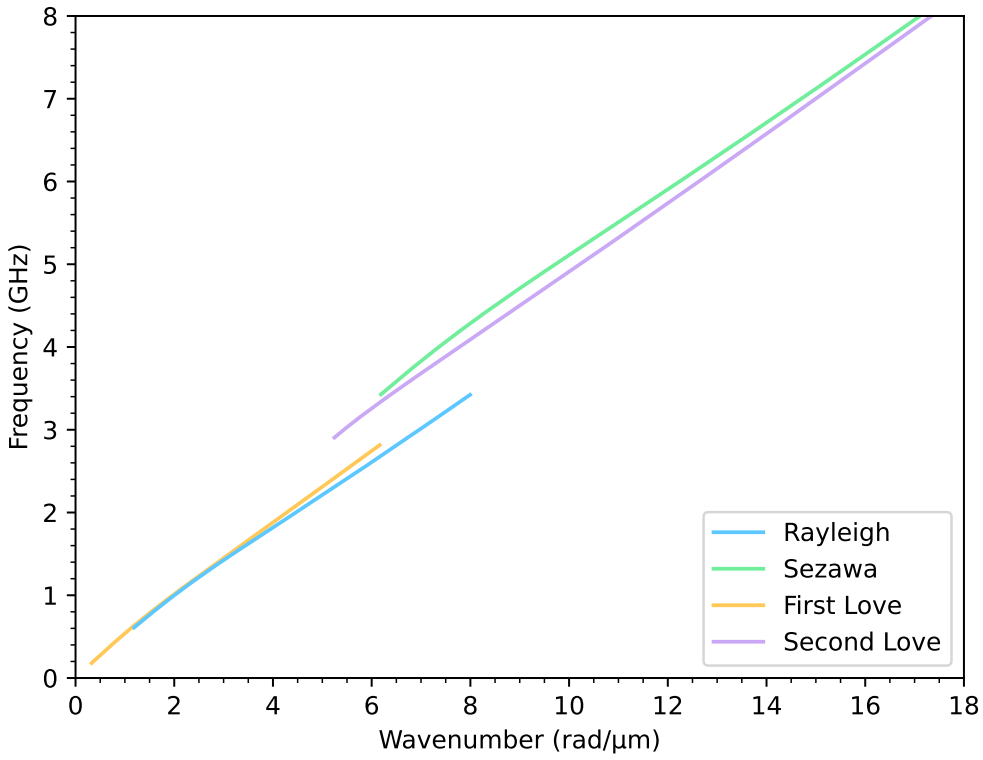

Figure 3.2: The calculated dispersion relations for Sample 1 using the model described in Section 3.1. The four lowest-order solutions in frequency are shown. The 'Rayleigh' and 'Sezawa' modes belong to one class of solutions, while the first and second Love modes belong to another. The slight curvature of the dispersion relations indicates the deviation from the first-order approximation that acoustic waves have a constant velocity.

The second class of solutions are 'Love modes', which have particle motion perpendicular to the direction of propagation for isotropic materials [80]. Given the narrow separation in frequency between Love-like and Rayleigh-like modes, differentiating between the two using simple IDT frequency response data, for example, would not be possible due to the finite linewidths.

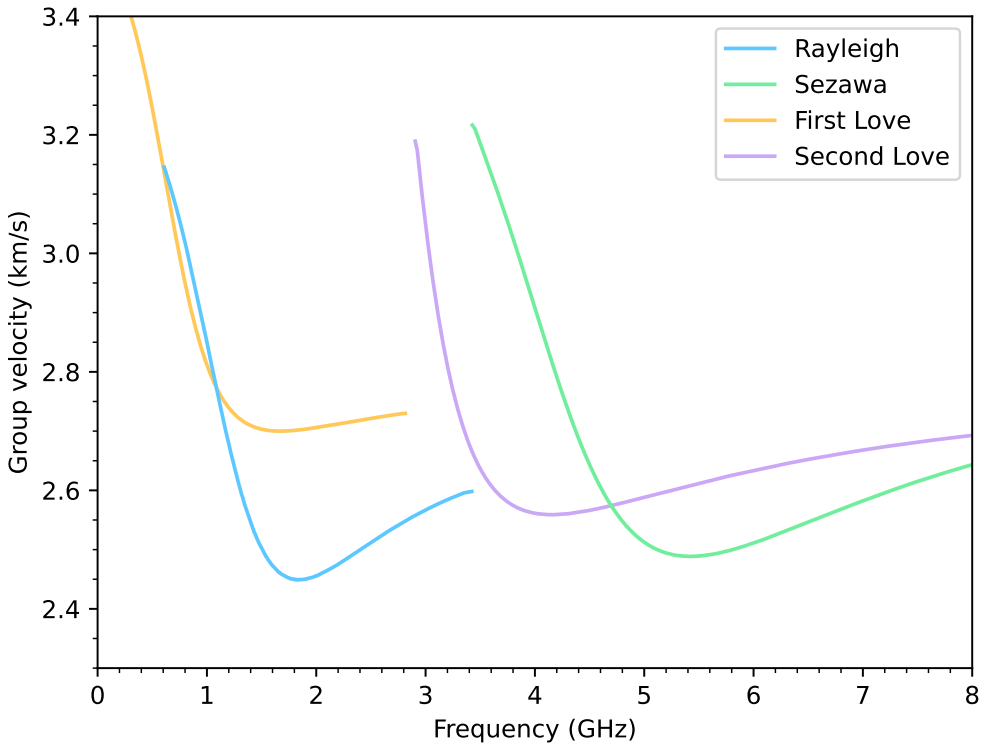

Figure 3.3: The calculated group velocities for Sample 1. The four lowest-order solutions in frequency are shown. The group velocities are calculated from the dispersion relations in Fig. 3.2 numerically using the expression $v_g = \frac{\partial \omega}{\partial k}$. The previously subtle curvature of the dispersion relations becomes much more evident when taking the derivatives, as does the difference between the two classes of solutions.

Instead, by numerically calculating the derivative of the angular frequency with respect to the wavevector to find the group velocity, the difference between the Rayleigh and Love-like modes becomes significantly more pronounced. Fig. 3.3 shows the group velocities for the four lowest-order modes in Sample 1. It is clear from this figure that if we measure the group velocities, differentiating between the modes is more feasible.

Finally, in Fig. 3.4, the calculated electromechanical coupling coefficients for Sample 1 are shown. We see here that the Love-like modes have expected coupling coefficients that are two to six orders of magnitude smaller than those of the Rayleigh-like modes. This, combined with the fact that the Love-like modes did not fit well with the experimental group velocity data shown in Section 5.4.2, means we choose to ignore this class of solutions henceforth. Also, note that the Rayleigh-like

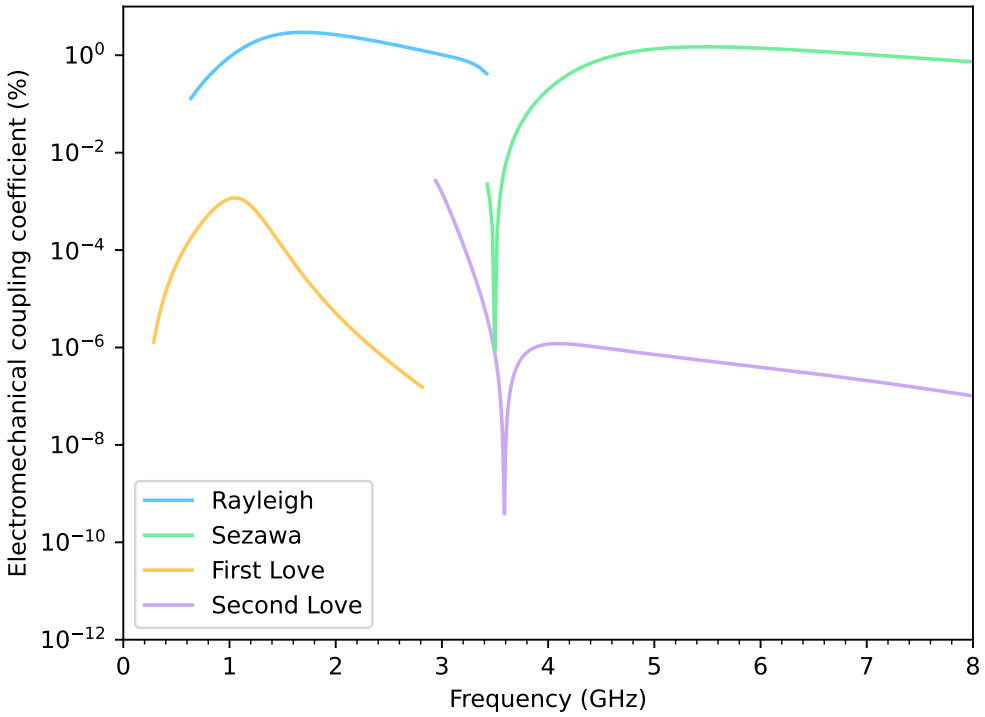

Figure 3.4: The electromechanical coupling coefficients calculated for Sample 1 using Eq. (3.8). The four lowest-order solutions in frequency are shown with the electromechanical coupling coefficients plotted on a logarithmic scale. The zeroth order Rayleigh-like mode shows the highest electromechanical coupling coefficient, followed by the Sezawa mode, while the Love modes show electromechanical coupling coefficients two to six orders of magnitude lower.

mode demonstrates the largest electromechanical coupling coefficients.

3.3 Modelling the dead layer

As discussed in Section 2.4.3, the dead layer appears to be inherent to the RF magnetron sputtered film of ZnO. To account for this in the model, an additional 200 nm layer between the YIG and the c-axis aligned ZnO was introduced. This layer is treated as polycrystalline ZnO with randomly oriented c-axes. To calculate the material properties of an arbitrarily aligned c-axis crystallite in this layer, we apply the transformations to the permittivity and elastic tensors given in Eq. (3.9) for arbitrary angles and then find the average properties by integrating over all possible angles [81]. This gives the following expressions for the permittivity

and elastic tensors

$$\epsilon'_{\text{dead}} = \int_0^{2\pi}\int_0^{2\pi}\int_0^{2\pi} \epsilon'(\alpha,\beta,\gamma)\, d\alpha\, d\beta\, d\gamma, \quad c'_{\text{dead}} = \int_0^{2\pi}\int_0^{2\pi}\int_0^{2\pi} c'(\alpha,\beta,\gamma)\, d\alpha\, d\beta\, d\gamma. \quad (3.10)$$

These transformations lead to relatively small changes in the material properties and tend to symmetrise the matrices, as expected. Any action of the electric dipoles is assumed to cancel globally, and thus, the piezoelectric tensor is set to zero. Finally, the density of the ZnO is assumed to remain unchanged. The calculated properties of the dead layer can be found in Tab. A.2 in Appendix A.

The effect on the group velocity with the addition of a 200 nm thick dead layer can be seen in Fig. 3.5a. The yellow and lilac curves show the previous Sample 1 group velocities where the dead layer was neglected, while the blue and yellow curves show the group velocities with the dead layer included. There is a fairly minimal change with the addition of the dead layer, a deepening of the dip in the curves is observed.

Physically, rather than a uniform layer of completely randomised c-axes, a gradual increase in c-axis alignment from the initial complete randomisation would be expected; however, given the minor change in the dispersion relation, we consider this simple model adequate as a first-order approximation. It is likely that the real group velocity curve lies somewhere between these curves as the model takes the worst-case scenario, where the dead layer has no coherence in the alignment of the electric dipoles.

This is also likely true of the coupling coefficients, shown in Fig. 3.5b, where a drop in the expected coupling by one to two orders of magnitude can be seen. This decrease is expected, given the electrical excitation from the embedded IDTs is concentrated around this dead layer, where there is no macroscopic alignment of electric dipoles and the piezoelectric tensor has been set to zero.

Although the model for the dead layer is not a perfect physical representation, we consider it more accurate to include rather than to neglect entirely, given it was consistently observed in XRD results.

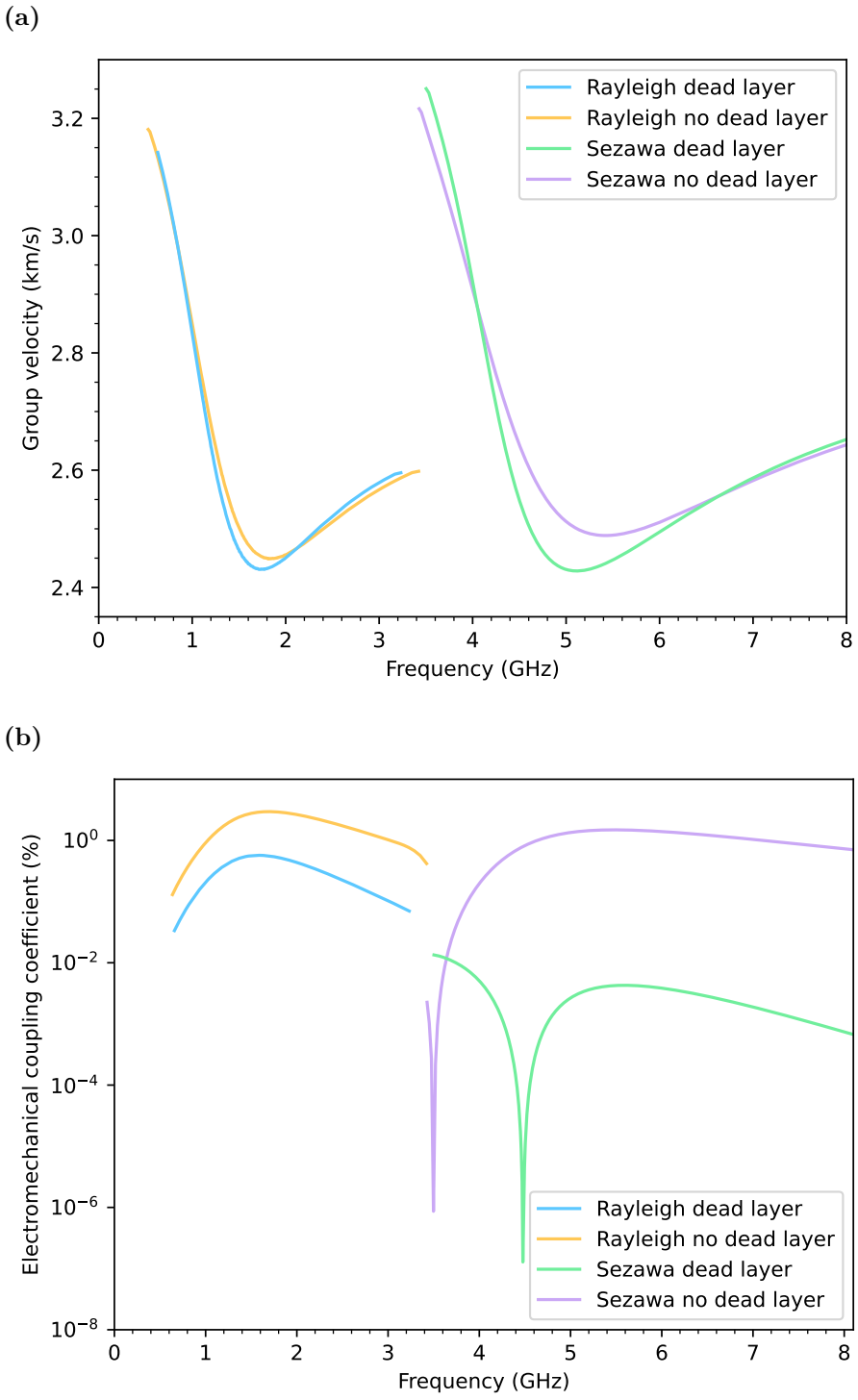

Figure 3.5: Comparison between the calculated (a) group velocities and (b) electromechanical coupling coefficients for Sample 1 with (blue and green) and without (yellow and lilac) the 200 nm dead layer of ZnO, where the c-axis is not aligned, included. The dead layer is modelled according to the description in Section 3.3. The change to the group velocities is relatively minor, with only a slight deepening of the dip. The electromechanical coupling constants, however, are decreased significantly (noting the logarithmic scale), as expected, given the dead layer is in direct contact with the interlayer IDTs.

3.4 Caveats

It is important to note three caveats regarding our methodology. First, the simple numerical model neglects the IDTs, particularly their finite thickness. Second, as mentioned, literature values for the elastic, piezoelectric, and permittivity tensors and density are used rather than measured values for our films, which will result in an error. However, as the model uses 23 material parameters, generally measured in bulk samples, there is no sensible method to estimate this error in the numerical calculation. Third, the model for the dead layer is only a first-order approximation.

3.5 Considerations when designing ZnO SAW transducers

With a working model to calculate the SAW dispersion relations, we consider some of the parameters that can be experimentally varied to tune the SAW properties. The results herein all include a 200 nm dead layer in their calculation.

3.5.1 The ZnO thickness

Firstly, the thickness of the ZnO is varied. Fig. 3.6 shows the group velocities calculated at three different thicknesses of ZnO on a 103nm layer of YIG with a GGG substrate. As the thickness increases, the frequency response is downshifted; this is as we would expect, given the mass of the ZnO layer is increasing. The group velocities, rather than the dispersion relations, are shown as it is much easier to differentiate between the curves.

For a fixed IDT excitation wavelength, this suggests that if we wish to couple to higher-order modes, the thickness of the ZnO should be increased. However, the characteristic SAW penetration depth for higher-order modes is typically smaller than that of the Rayleigh-like mode and, especially with thicker ZnO layers, will, therefore, induce smaller magnetoelastic driving fields in the YIG film. Therefore, to couple to higher order modes, the best first step is to minimise the IDT finger

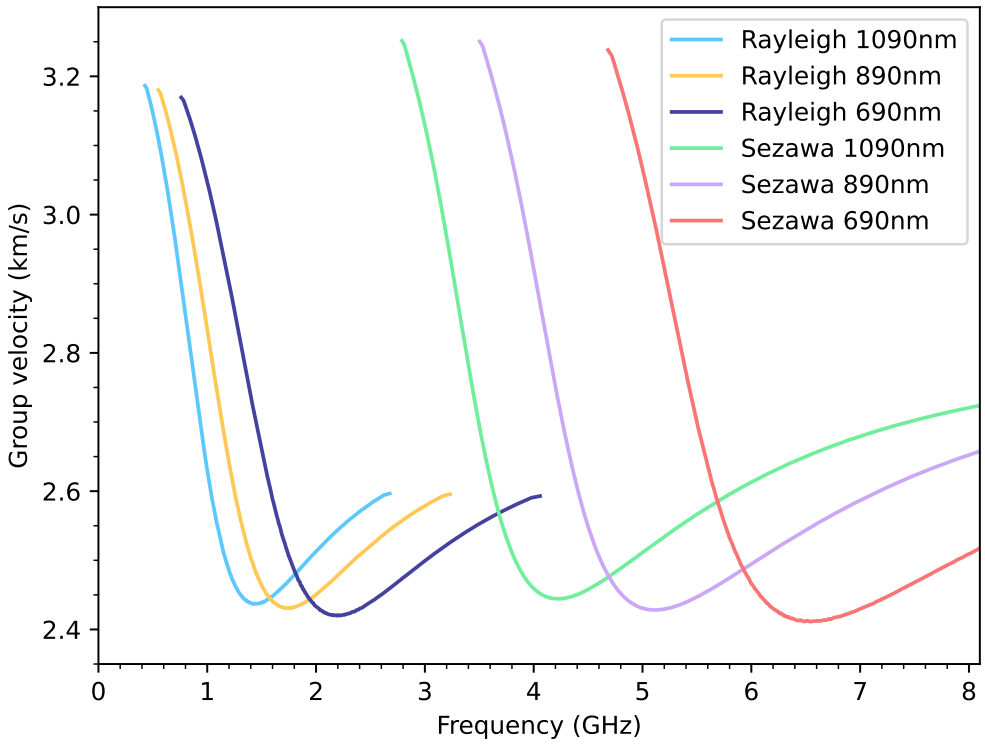

Figure 3.6: The calculated group velocities of the Rayleigh-like and first Sezawa-like modes for three different thicknesses of ZnO including the 200 nm dead layer on a 103nm layer of YIG with a GGG substrate. The increasing ZnO thickness can be seen to downshift the frequency of the mode, as expected, given the increasing mass.

size. Following this, working at higher-order harmonics of the IDT is likely to prove more effective than increasing the ZnO thickness much beyond one wavelength.

If, instead, the maximum coupling strength at higher frequencies is desired, based on the electromechanical coupling coefficients, the best approach is to use the Rayleigh-like mode and minimise the thickness of the ZnO. However, the 200 nm dead layer sets a limit on the minimum usable film thickness.

3.5.2 The orientation of the piezoelectric ZnO c-axis

The perhaps more interesting property to vary is the ZnO piezoelectric c-axis orientation. This is commonly studied in the case of bulk acoustic wave transducers and has a significant effect on the electromechanical coupling coefficient. In the case of an out-of-plane c-axis, the bulk acoustic waves are purely longitudinal, whereas, with the c-axis aligned at $\sim 40^\circ$ to the normal of the plane, the waves

are purely shear [27, 82, 83].

Rotation about the x_2-axis is considered, where 0° corresponds to an out-of-plane oriented c-axis. The dispersion relations were found from 0° to 90°, and the slowness curves were then calculated. Slowness is defined as the inverse of the velocity and is commonly used in the literature when discussing the rotation of crystallographic axes [27]; we consider both group and phase velocities. These curves can be seen in Fig. 3.7a for the Rayleigh-like mode at 2.7 GHz, and Fig. 3.7b for the Sezawa-like mode at 5.65 GHz. In both cases, the waves travel at maximum velocity when the c-axis is oriented at 48°. This suggests changing the orientation angle of the c-axis to approximately 48° may be sensible to avoid beam steering effects [84, 85].

The electromechanical coupling coefficients were also calculated as a function of the ZnO c-axis orientation angle over a range of frequencies. The resulting coupling coefficients for the Rayleigh-like mode can be seen in Fig. 3.8a and for the Sezawa-like mode in Fig. 3.8b. For both the Rayleigh and Sezawa-like modes, maxima are observed in the calculated coupling coefficients with a c-axis angle of approximately 50°. This suggests $\sim 50°$ is the optimum c-axis angle for maximum velocity and SAW excitation efficiency.

In the case of the Rayleigh-like mode, an unexpected minimum in the intensity is observed at around 50° and 1.3 GHz; this occurs due to mode mixing [78, 86] between the Rayleigh-like mode and the first Love-like mode as their phase velocities intersect. This demonstrates the value of carrying out these calculations before choosing the IDT wavelength, as one could inadvertently design an IDT to work at such a minimum.

Note that for the data shown in Fig. 3.8a, a sharp discontinuity occurred where the calculation converged between the Rayleigh-like and Love-like solutions at different positions for the free and metallic phase velocities, before consistently converging on the Rayleigh-like solution as the phase velocities of the two modes diverged. This occurred over a small range, approximately 0.05 GHz centred on ~ 1.4 GHz between 37° and 59°. The points over the discontinuity were removed and then interpolated between the ranges to eliminate this discontinuity. An example of

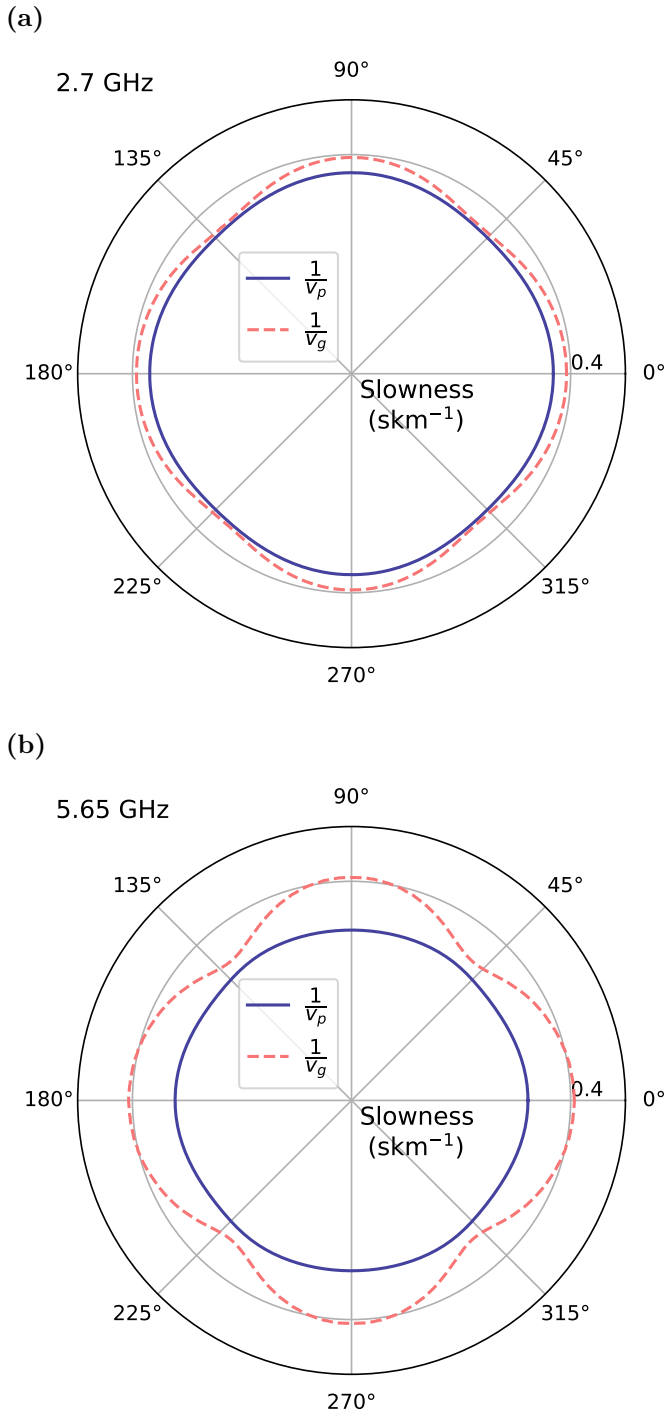

Figure 3.7: Slowness as a function of the ZnO c-axis orientation at fixed frequencies for Sample 1. (a) Slowness curves for the Rayleigh-like mode at 2.7 GHz. (b) Slowness curves for the Sezawa-like mode at 5.65 GHz. Rotation is about the $\boldsymbol{x_2}$ axis, and 0° corresponds to an out-of-plane oriented c-axis. The symmetry of the ZnO means the curves repeat every 90°. The dark blue curves show the phase velocity slowness, $1/v_p$, and the red curves show the group velocity slowness, $1/v_g$. Both plots have minima in the slowness at 48°.

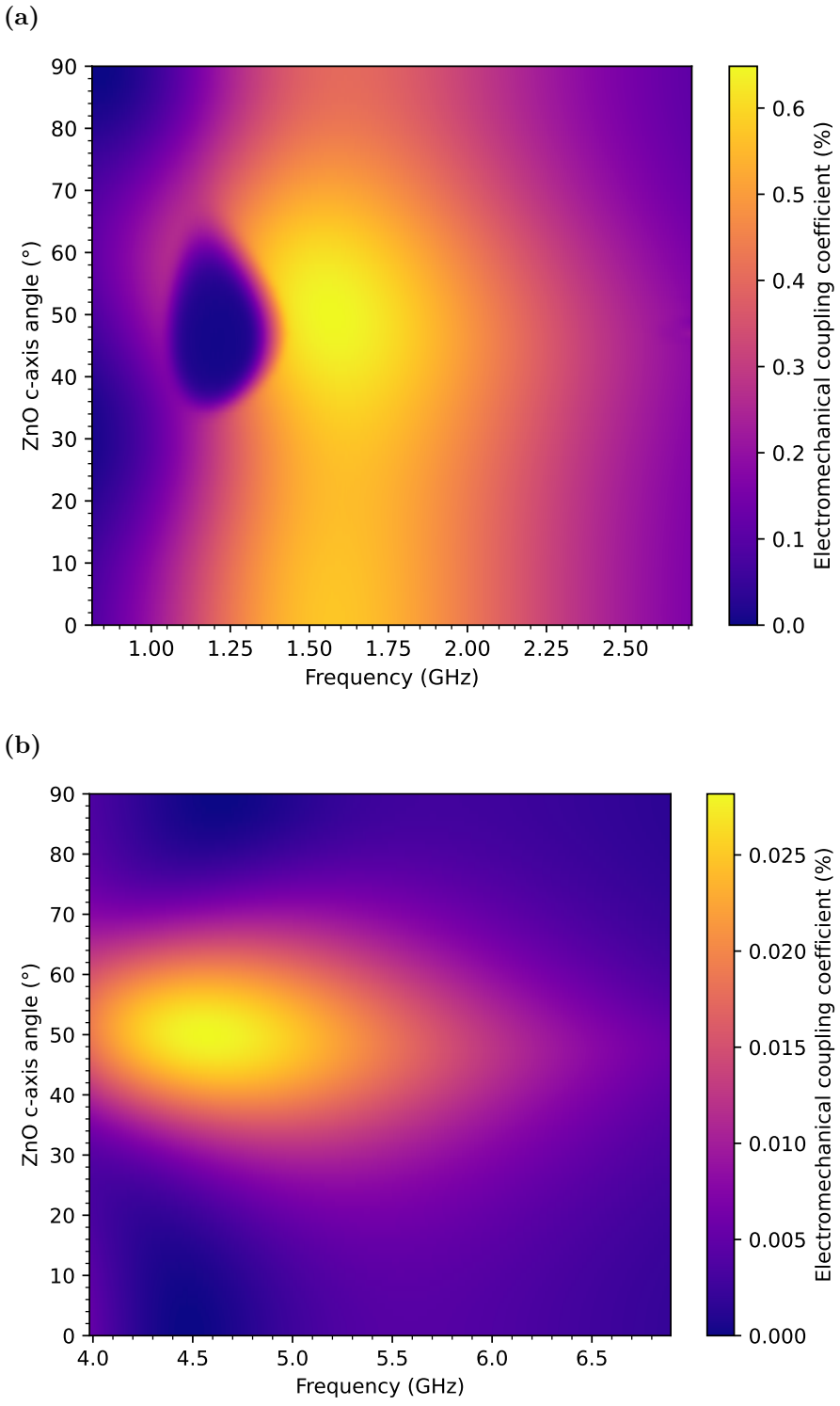

Figure 3.8: Electromechanical coupling constant as a function of ZnO c-axis angle and frequency for Sample 1. (a) The Rayleigh-like mode and (b) the Sezawa-like mode. Rotation is about the x_2 axis, and 0° corresponds to an out-of-plane oriented c-axis. Maxima occur at approximately 50° and 1.6 GHz for the Rayleigh-like mode and 50° and 4.6 GHz for the Sezawa-like mode. The minimum at approximately 1.2 GHz and 50° for the Rayleigh-like mode occurs due to mode mixing with the Love-like mode.

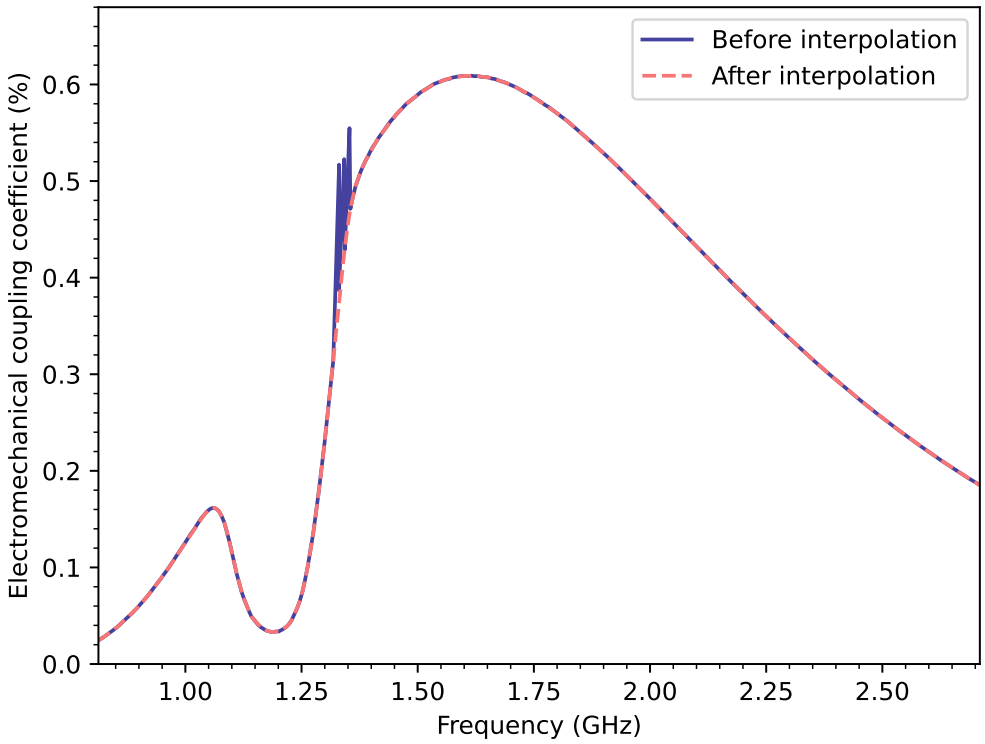

Figure 3.9: The electromechanical coupling coefficient as a function of frequency with the ZnO c-axis angled at 38° to the surface normal calculated for Sample 1. The raw results of the calculation from the MATLAB script are shown in dark blue, and the results after the interpolation, used to produce Fig. 3.8a, are shown in dashed red. The discontinuity in the raw calculation occurs due to mode mixing between the Rayleigh-like mode and the Love-like mode when their phase velocities intersect.

the interpolation can be seen in Fig. 3.9. The characteristic shape of the coupling coefficient does not change, and hence, we consider this a valid methodology.

To conclude, based on these results, with the ZnO c-axis aligned at approximately 50° to the surface normal, the electromechanical coupling can be maximised. This could potentially increase the IDT efficiency and, therefore, both the SAW and spin-wave intensities. Although these results are useful for designing future samples, it was decided that a normally oriented c-axis would serve as a more viable proof of concept, hence the orientations of Samples 1 & 2.

Note, the in-plane orientation of the GGG/YIG crystallographic axes was considered by rotating the relevant GGG and YIG tensors about the out-of-plane x_3-axis. Both the phase and group velocities were found to be isotropic with the rotation of this axis.

4

The coupling of SAWs and spin waves

In this chapter, a theoretical model to describe the coupling between SAWs and spin waves is developed. The expected spin-wave excitation, as a function of both the magnitude of the magnetic field and the angle between the direction of the SAW propagation and the applied magnetic field, for a fixed SAW excitation frequency, is shown by considering solutions to the LLG equation.

4.1 The context and approach

Before launching into the theory, we note that there has been increasing research on the coupling between SAWs and spin waves in thin magnetic films [87–99]. This has led to the observation of several intriguing phenomena, such as non-reciprocal spin-wave generation/ SAW absorption as a result of a mismatched helicity between the SAW-induced magnetoelastic driving fields and the fixed precession of the magnetisation [87, 90, 92], with possible application as acoustic isolators or circulators [100–103]. However, these SAW-spin wave studies have suffered from relatively high spin-wave damping in the magnetic materials of interest. For example, thin films of CoFeB have propagation lengths typically on the order of micrometres [104, 105]. Therefore, it is hoped that the reduced damping in YIG could enable improved future observation of propagating spin waves. Furthermore,

it may be possible to study effects such as the strong coupling between SAWs and spin waves via the patterning of a resonator structure, for example [106, 107].

Based on the success of Dreher et al. [108] and Küß et al. [91] in modelling similar systems, the same approach is taken here and will be laid out in detail in the following sections. Prior to this, however, we note that there are two main assumptions to their approach. Firstly, as the thin film of YIG is only 103 nm thick, roughly 10 times smaller than the wavelength of the 2.9 GHz SAW, the strain is considered to be uniform throughout the layer; the SAW is treated as a bulk acoustic wave. Secondly, as ZnO is non-magnetic, the acoustic wave propagation and magnetisation dynamics are only considered in the YIG layer, rather than solving the coupled equations for the two-layer system with ZnO.

4.2 The theoretical model

To find the expected coupling, the LLG equation needs to be solved for the YIG layer, taking into account the dynamical strains induced by the SAW. First, the geometry of the system and the terms contributing to the magnetic field will be discussed, before a small amplitude perturbation to the magnetisation will be considered to allow the LLG equation to be solved, giving the spin-wave solutions.

4.2.1 The geometry

Fig. 4.1 shows the geometry to be used in the model. The (x, y, z) coordinate system is used to define the SAW propagation direction, x, and normal to the film, z; equivalent to the (x_1, x_2, x_3) coordinate system previously defined in Fig. 3.1. An additional coordinate system $(1, 2, 3)$ is also introduced, where the equilibrium magnetisation of the YIG points along the 3-axis and the 2-axis remains in the plane of the film. The magnetisation $\boldsymbol{m} = \boldsymbol{M}/M_\mathrm{S}$ is used, and the precession cone of the magnetisation is shown, which will be discussed further later.

The matrix U, is used to transform between the coordinate systems. The magnetisation, $\boldsymbol{m}$, in the (x, y, z) coordinate system is therefore given by

$$\boldsymbol{m} = U\boldsymbol{m}_{123} = \begin{pmatrix} \cos\theta_0\cos\phi_0 & -\sin\phi_0 & \sin\theta_0\cos\phi_0 \\ \cos\theta_0\sin\phi_0 & \cos\phi_0 & \sin\theta_0\sin\phi_0 \\ -\sin\theta_0 & 0 & \cos\theta_0 \end{pmatrix} \boldsymbol{m}_{123}, \tag{4.1}$$

where $\boldsymbol{m}_{123}$ is used to express the magnetisation in the $(1, 2, 3)$ coordinate system.

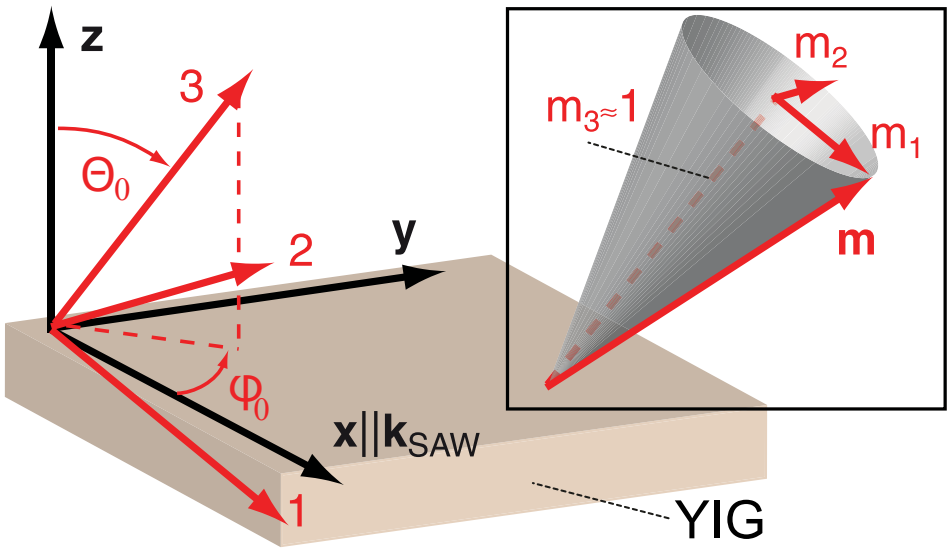

Figure 4.1: The geometry and coordinate systems used in the SAW-spin wave coupling model. The (x, y, z) coordinate system is equivalent to the (x_1, x_2, x_3) coordinate system as previously defined for the SAW in Fig. 3.1. The $(1, 2, 3)$ coordinate system is introduced with the 3-direction corresponding to the equilibrium magnetisation direction. The inset shows the precession cone of the magnetisation about the equilibrium direction, with transverse magnetisation components m_1 and m_2, adapted from [108].

4.2.2 The effective magnetic field

When previously discussing the LLG equation in Section 1.2.2, we neglected to discuss the form of the magnetic field, $\boldsymbol{H}$. Typically, an effective magnetic field, $\boldsymbol{H}_{\text{eff}}$, is defined where the equilibrium magnetisation is aligned with this field. The effective field is comprised of many individual contributions,

$$\boldsymbol{H}_{\text{eff}} = \boldsymbol{H}_{\text{ext}} + \boldsymbol{H}_{\text{demag}} + \boldsymbol{H}_{\text{ex}} + \boldsymbol{H}_{\text{ani}} + \boldsymbol{H}_{\text{me}} + ..., \tag{4.2}$$

where $\boldsymbol{H}_{\text{ext}}$ is the applied external magnetic field, $\boldsymbol{H}_{\text{demag}}$ the demagnetising field, $\boldsymbol{H}_{\text{ex}}$ the exchange field, $\boldsymbol{H}_{\text{ani}}$ the anisotropy field, and $\boldsymbol{H}_{\text{me}}$ the magnetoelastic driving field.

It is also possible to define the effective field in terms of the free energy density, F_{tot} [109], where

$$\mu_0 \boldsymbol{H}_{\text{eff}} = -\frac{1}{M_{\text{S}}} \nabla_{\boldsymbol{m}} F_{\text{tot}} \tag{4.3}$$

and $\nabla_{\boldsymbol{m}}$ is the gradient operator taken with respect to the magnetisation. As in Eq. (4.2), the free energy density can be broken down into a sum of individual contributions.

To find the effective field, the terms that contribute to the free energy density in the (x, y, z) coordinate system are defined. These are broken down into the static components and the dynamic components that enable the precession of the magnetisation and, therefore, the excitation of spin waves.

4.2.3 The equilibrium magnetisation

Before finding the effective field, the equilibrium magnetisation direction should be determined. The contributing free energy density terms are defined, and by minimising their sum, the direction of the equilibrium magnetisation can be found.

The external magnetic field free energy density

For the micro-focused Brillouin Light Scattering set-up that will be described in Chapter 5, the external field is applied in the plane of the YIG and, therefore, given by

$$\boldsymbol{H}_{\text{ext}} = H_{\text{ext}} \begin{pmatrix} \cos\phi_{\text{ext}} \\ \sin\phi_{\text{ext}} \\ 0 \end{pmatrix}, \tag{4.4}$$

where ϕ_{ext} gives the angle between the external magnetic field and the SAW propagation direction.

In terms of the free energy density, it can be expressed as

$$F_{\text{ext}} = -\mu_0 M_{\text{S}} \boldsymbol{H}_{\text{ext}} \cdot \boldsymbol{m}. \tag{4.5}$$

The demagnetising free energy density

The demagnetising field arises from the magnetisation of a material and acts to oppose the external magnetic field, effectively reducing the net magnetic field inside the material. It aims to minimise the magnetostatic energy of the system and is highly geometry-dependent. In the case of an infinite, uniformly magnetised thin film, the demagnetising free energy density can be expressed as [110],

$$F_{\text{demag}} = \frac{\mu_0 M_{\text{S}}^2}{2} m_z^2. \tag{4.6}$$

The anisotropy free energy density

Magnetocrystalline anisotropy arises from the crystal structure of the material, with certain directions exhibiting preferred directions for magnetic alignment. YIG has a relatively small cubic magnetocrystalline anisotropy with an easy axis along the (111) direction [111], which we approximate as a uniaxial out-of-plane anisotropy. Note the (111) direction is out-of-the-plane for thin-film Samples 1 & 2.

For uniaxial anisotropy directed along the unit vector $\boldsymbol{u}$, the free energy density is given by

$$F_{\text{ani}} = K_{\text{u}} M_{\text{S}} \left(\boldsymbol{m} \cdot \boldsymbol{u}\right)^2, \tag{4.7}$$

where K_{u} is the magnetocrystalline anisotropy constant.

The equilibrium magnetisation

Taking these contributions into account gives the free energy density,

$$\begin{aligned} F_{\text{eq}} =& F_{\text{ext}} + F_{\text{demag}} + F_{\text{ani}} \\ =& -\mu_0 M_{\text{S}} \boldsymbol{H}_{\text{ext}} \cdot \boldsymbol{m} + \frac{\mu_0 M_{\text{S}}^2}{2} m_z^2 + K_{\text{u}} M_{\text{S}} \left(\boldsymbol{m} \cdot \boldsymbol{u}\right)^2, \end{aligned} \tag{4.8}$$

which can be minimised to find the equilibrium magnetisation direction.

4.2.4 Spin-wave contributions to the free energy density

To find the effective field, contributions to the free energy density from dipolar and exchange spin waves should also be included [91, 110].

Dipolar spin waves

For dipolar spin waves propagating in the x-direction, there is a contribution given by [112]

$$F_{\mathrm{dip}} = \frac{\mu_0 M_{\mathrm{S}}^2}{2}\left((1-G_{\mathrm{SW}})m_x^2 + G_{\mathrm{SW}}m_z^2\right), \tag{4.9}$$

where

$$G_{\mathrm{SW}} = \frac{1-e^{-|k_{\mathrm{SW}}|d}}{|k_{\mathrm{SW}}|d}, \tag{4.10}$$

with wavevector k_{SW} and thin film thickness d.

Exchange spin waves

The free energy density associated with the exchange spin waves is given by [110],

$$F_{\mathrm{ex}} = -A_{\mathrm{ex}}M_{\mathrm{S}}k_{\mathrm{SW}}^2\left(m_x^2 + m_y^2 + m_z^2\right), \tag{4.11}$$

where A_{ex} is the exchange stiffness.

4.2.5 The static free energy density

Taking these contributions into account gives the static free energy density for the system,

$$\begin{aligned} F_{\mathrm{st}} =& F_{\mathrm{ext}} + F_{\mathrm{ani}} + F_{\mathrm{dip}} + F_{\mathrm{ex}} \\ =& -\mu_0 M_{\mathrm{S}}\boldsymbol{H}_{\mathrm{ext}}\cdot\boldsymbol{m} + K_{\mathrm{u}}M_{\mathrm{S}}\left(\boldsymbol{m}\cdot\boldsymbol{u}\right)^2 \\ &+ \frac{\mu_0 M_{\mathrm{S}}^2}{2}\left((1-G_{\mathrm{SW}})m_x^2 + G_{\mathrm{SW}}m_z^2\right) - A_{\mathrm{ex}}M_{\mathrm{S}}k_{\mathrm{SW}}^2\left(m_x^2+m_y^2+m_z^2\right). \end{aligned} \tag{4.12}$$

4.2.6 The dynamic free energy density

The dynamic contribution to the free energy density arising from the magnetoelastic coupling with the SAW is now required. As discussed in Section 1.3.2, the equation for the dynamic contribution to the magnetoelastic free energy is given by

$$\begin{aligned} F_{\mathrm{dyn}} = F_{\mathrm{me}} = M_{\mathrm{S}}\Big\{& b_1\Big(S_{xx}(x,t)m_x^2 + S_{yy}(x,t)m_y^2 + S_{zz}(x,t)m_z^2\Big) \\ &+ b_2\Big(S_{xy}(x,t)m_xm_y + S_{xz}(x,t)m_xm_z + S_{yz}(x,t)m_ym_z\Big)\Big\}, \end{aligned} \tag{4.13}$$

where S_{ij} are components of the strain tensor.

It is also necessary to consider a contribution from the magnetorotational tensor [90, 113], ω_{ij}, which describes the rotational deformation of the lattice, where

$$\omega_{ij} = \frac{1}{2}\left(\frac{\partial u_i}{\partial x_j} + \frac{\partial u_j}{\partial x_i}\right) \tag{4.14}$$

and u_i are the mechanical displacements as defined in Section 3.1. However, as this contribution to the free energy depends on the magnetocrystalline anisotropy, which in the case of YIG is much smaller than the magnetoelastic coupling coefficients, we choose to neglect this contribution.

4.2.7 Solving the Landau-Lifshitz-Gilbert equation

Allowing small transverse perturbations from the equilibrium magnetisation, $\boldsymbol{m_0}$, the magnetisation can be expressed in the $(1, 2, 3)$ coordinate system as

$$\boldsymbol{m} = \begin{pmatrix} 0 \\ 0 \\ m_0 \end{pmatrix} + \begin{pmatrix} m_1 \\ m_2 \\ 0 \end{pmatrix} + \mathcal{O}(m_1^2, m_2^2), \tag{4.15}$$

where m_1 and m_2 describe the precession of the magnetisation cone, as shown by the inset in Fig. 4.1, and $m_1, m_2 \ll m_0$. Using this expression for the magnetisation, it is now possible to use Eq. (4.3) to find the effective magnetic field.

The expression for $\nabla_{\boldsymbol{m}} F_{\mathrm{st}}$ can be expanded at the equilibrium position of $\boldsymbol{m}$, where only terms up to first order in m_1 and m_2 are considered [109]. This gives an expression for the static effective magnetic field,

$$\begin{aligned} \mu_0 \boldsymbol{H}_{\mathrm{eff,\,st}} = -\frac{1}{M_{\mathrm{S}}} \nabla_{\boldsymbol{m}} \left(F_{\mathrm{st}}\right) &= \begin{pmatrix} m_1 \frac{\partial^2 F_{\mathrm{st}}}{\partial m_1^2}\big|_{\boldsymbol{m}=\boldsymbol{m_0}} + m_2 \frac{\partial^2 F_{\mathrm{st}}}{\partial m_1 \partial m_2}\big|_{\boldsymbol{m}=\boldsymbol{m_0}} \\ m_2 \frac{\partial^2 F_{\mathrm{st}}}{\partial m_2^2}\big|_{\boldsymbol{m}=\boldsymbol{m_0}} + m_1 \frac{\partial^2 F_{\mathrm{st}}}{\partial m_1 \partial m_2}\big|_{\boldsymbol{m}=\boldsymbol{m_0}} \\ \frac{\partial F_{\mathrm{st}}}{\partial m_3} \end{pmatrix} \\ &= \begin{pmatrix} m_1 F_{11} + m_2 F_{12} \\ m_2 F_{22} + m_1 F_{12} \\ F_3 \end{pmatrix}. \end{aligned} \tag{4.16}$$

Similarly, $\nabla_{\boldsymbol{m}} F_{\mathrm{dyn}}$ can be expanded. In this case only terms that are zeroth order in m_1 and m_2 are kept. This gives the expression for the dynamic effective field,

$$\mu_0 \boldsymbol{H}_{\mathrm{eff,\,dyn}} = -\frac{1}{M_{\mathrm{S}}} \nabla_{\boldsymbol{m}} \left(F_{\mathrm{dyn}}\right) = -\begin{pmatrix} \frac{\partial F_{\mathrm{dyn}}}{\partial m_1}\big|_{\boldsymbol{m}=\boldsymbol{m_0}} \\ \frac{\partial F_{\mathrm{dyn}}}{\partial m_2}\big|_{\boldsymbol{m}=\boldsymbol{m_0}} \\ \frac{\partial F_{\mathrm{dyn}}}{\partial m_3}\big|_{\boldsymbol{m}=\boldsymbol{m_0}} \end{pmatrix} = \mu_0 \begin{pmatrix} h_1 \\ h_2 \\ 0 \end{pmatrix}. \tag{4.17}$$

Giving the following explicit expressions for the magnetoelastic driving fields in terms of the SAW-induced strains,

$$\begin{aligned}\mu_0 h_1 =& -2b_1\Big(S_{xx}\cos^2\phi_0 + S_{yy}\sin^2\phi_0 - S_{zz}\Big)\sin\theta_0\cos\theta_0 \\ & -2b_2\Big\{\Big(S_{xz}\cos\phi_0 + S_{yz}\sin\phi_0\Big)\cos 2\theta_0 + 2S_{xy}\sin\theta_0\cos\theta_0\sin\phi_0\cos\phi_0\Big\} \\ \mu_0 h_2 =& +2b_1\Big(S_{xx} - S_{yy}\Big)\sin\theta_0\sin\phi_0\cos\phi_0 \\ & -2b_2\Big\{\Big(S_{yz}\cos\phi_0 - S_{xz}\sin\phi_0\Big)\cos\theta_0 + S_{xy}\sin\theta_0\cos 2\phi_0\Big\}.\end{aligned} \tag{4.18}$$

These driving fields strongly depend on the strain components, and therefore, their form is influenced by whether the propagating SAW is Rayleigh-like or Love-like. Furthermore, the values of b_1, b_2, S_{ij}, and the equilibrium magnetisation direction determine the helicity of the driving field. As the spin waves can also have a certain preferred helicity of the precession of magnetisation, under certain conditions, there can be a helicity mismatch resulting in low coupling efficiency. This preferred helicity of the precession of magnetisation is reversed upon reversal of the equilibrium magnetisation direction, determined by the external magnetic field when sufficiently large, which can result in highly non-reciprocal SAW-spin wave coupling.

Referring back to Eq. (1.6) and using the magnetisation $\boldsymbol{m} = \boldsymbol{M}/M_\mathrm{S}$, the LLG equation can be expressed as

$$\frac{\mathrm{d}\boldsymbol{m}}{\mathrm{d}t} = -\mu_0\gamma\left(\boldsymbol{m}\times\boldsymbol{H}_\mathrm{eff}\right) + \alpha\left(\boldsymbol{m}\times\frac{\mathrm{d}\boldsymbol{m}}{\mathrm{d}t}\right). \tag{4.19}$$

To look for spin-wave solutions, we propose a plane wave ansatz for the transverse magnetisation with

$$m_1 = m_1^0 e^{i(k_\mathrm{SW}x - \omega_\mathrm{SW}t)} \quad \& \quad m_2 = m_2^0 e^{i(k_\mathrm{SW}x - \omega_\mathrm{SW}t)}, \tag{4.20}$$

where the wave is propagating in the x direction, with wavevector k_SW, angular frequency ω_SW, and amplitudes m_1^0 and m_2^0 for the m_1 and m_2 components, respectively. Substituting this ansatz into the LLG equation, along with the expression for the effective field, gives the equation

$$\begin{pmatrix} F_{11} - F_3 - \frac{i\omega_{SW}\alpha}{\gamma} & F_{12} + \frac{i\omega_{SW}}{\gamma} \\ F_{12} - \frac{i\omega_{SW}}{\gamma} & F_{22} - F_3 - \frac{i\omega_{SW}\alpha}{\gamma}\end{pmatrix}\begin{pmatrix} m_1 \\ m_2\end{pmatrix} = \mu_0\begin{pmatrix} h_1 \\ h_2\end{pmatrix}. \tag{4.21}$$

This equation can then be solved to find the transverse magnetisation, giving the expression

$$\begin{aligned}\begin{pmatrix} M_1 \\ M_2 \end{pmatrix} &= \frac{\mu_0 M_\mathrm{S}}{D} \begin{pmatrix} F_{22} - F_3 - \frac{i\omega_{SW}\alpha}{\gamma} & -F_{12} - \frac{i\omega_{SW}}{\gamma} \\ -F_{12} + \frac{i\omega_{SW}}{\gamma} & F_{11} - F_3 - \frac{i\omega_{SW}\alpha}{\gamma} \end{pmatrix} \times \begin{pmatrix} h_1 \\ h_2 \end{pmatrix} \\ &= \bar{\chi} \begin{pmatrix} h_1 \\ h_2 \end{pmatrix},\end{aligned} \tag{4.22}$$

where

$$D = \left(F_{11} - F_3 - \frac{i\omega_{SW}\alpha}{\gamma} \right) \left(F_{22} - F_3 - \frac{i\omega_{SW}\alpha}{\gamma} \right) - F_{12}^2 - \left(\frac{\omega_{SW}}{\gamma} \right)^2 \tag{4.23}$$

and $\bar{\chi}$ is the Polder susceptibility tensor, which describes the linear response of the magnetisation to small time-varying magnetic fields [114]. The Polder susceptibility tensor is only dependent on the static component of the free energy density, while the dynamic free energy density determines the driving fields.

Eq. (4.22) can be solved numerically as a function of the angle and magnitude of the applied external magnetic field to find the out-of-plane magnetisation component, M_z. For sufficiently large in-plane external magnetic fields, that is to say, the fields used in the experiments presented in Chapter 5, the equilibrium magnetisation will be in the plane, and therefore, the M_z component will depend only on the spin waves. Thus, by solving Eq. (4.22), the expected spin wave excitations induced by the magnetoelastic SAW driving fields can be calculated.

4.3 Parameters for the theoretical model

The theoretical model describing the spin waves requires a number of input parameters to find the solutions. These parameters are given below, and their validity for use in the model is discussed.

4.3.1 YIG parameters

The relevant parameters of the YIG thin film required for the spin-wave calculation are given in Tab. 4.1. The values of the saturation magnetisation, uniaxial anisotropy field, Landé g-factor, and Gilbert damping were determined by

Prof. Dr. Weiler's group at RPTU from FMR measurements on an unpatterned YIG (103 nm)/ZnO (960 nm) thin-film heterostructure. These values should be comparable to those of the samples used in this thesis, given that, besides the absence of IDT structures, the sample is almost identical. Furthermore, given the small errors, these values should enable accurate calculation of the spin wave dispersion in the YIG sample.

The value of the exchange constant is taken from Klinger et. al. [115] measured for 900 nm to 2600 nm LPE grown thin YIG films. This is fairly similar to the samples used here, and in addition, as the length scales are relatively large compared to the exchange length, this is considered sufficiently accurate for the calculation. Finally, the values for the magnetoelastic constants, as defined in Section 1.3.2, are taken from Comstock [116] as measured for single-crystal YIG. Given that the samples used here are high-quality single-crystal LPE-grown films, using these values should give accurate results.

Table 4.1: The relevant parameters used in the spin-wave calculations for YIG. The Gilbert damping coefficient was measured on a similar unpatterned GGG/YIG/ZnO heterostructure by FMR.

Parameter	Symbol	Value
Exchange stiffness coefficient [115]	A_{ex}	$(3.7 \pm 0.4) \cdot 10^{-12}\,\mathrm{Jm}^{-1}$
Saturation magnetisation	M_S	$146.27 \pm 0.05\,\mathrm{kAm}^{-1}$
Uniaxial anisotropy field	H_uni	$0.43 \pm 0.02\,\mathrm{kAm}^{-1}$
Landé g-factor	g_J	2.02700 ± 0.00004
Uniaxial magnetoelastic constant [116]	b_1	$3.48\times10^5\,\mathrm{Jm}^{-3}$
Biaxial magnetoelastic constant [116]	b_2	$6.96\times10^5\,\mathrm{Jm}^{-3}$
Gilbert damping coefficient	α	$(5.13 \pm 0.02) \cdot 10^{-4}$

4.3.2 SAW parameters

In addition to the parameters for YIG, the strains induced by the SAWs should be calculated using the model from Chapter 3. As will be shown in Chapter 5, this model agrees well with experiment, and therefore, the strains used in the calculation should be reasonably accurate; however, this is likely to be the least accurate part of the calculation due to the caveats discussed in Section 3.4.

As shown in Section 3.1, Eq. (3.4) can be solved to find the normalised mechanical displacements as a function of depth. Fig. 4.2 shows these mechanical displacements calculated for the Rayleigh-like mode at 2.9 GHz in Sample 1. These displacements have been normalised by the maximum value of the displacement, given by the real component of u_x at the surface. We can see that, as expected for typical Rayleigh mode solutions [78, 91], the dominant contributions are u_x and u_z, with the usual phase differences indicated by the real and imaginary components. There is also a small contribution to u_y introduced by the anisotropic layered structure. The characteristic exponential decay of the amplitude can also be seen.

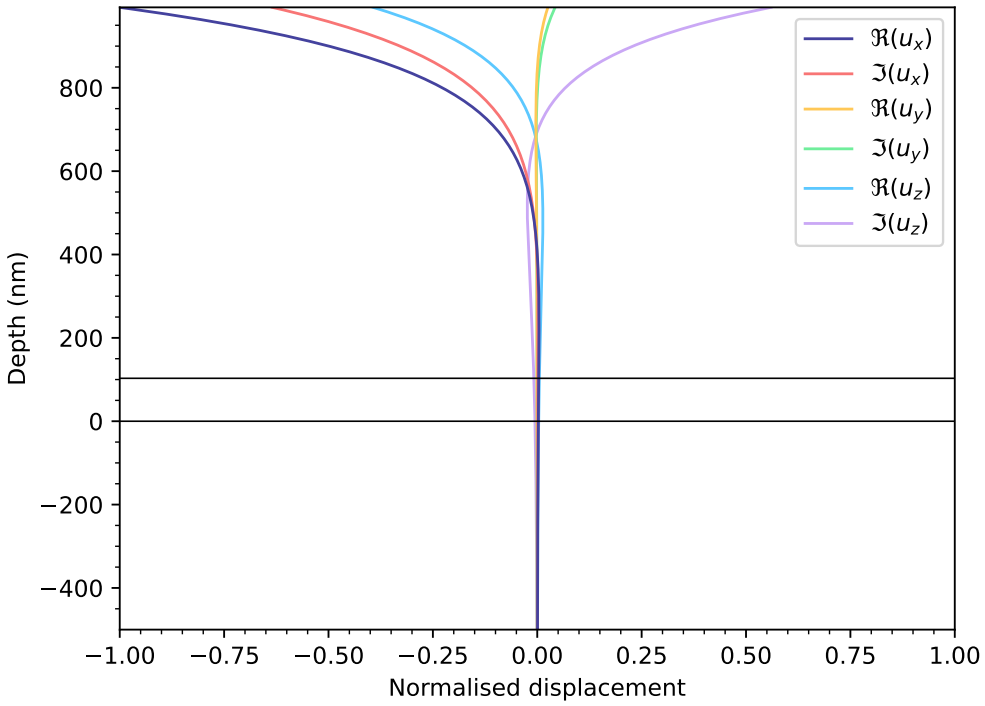

Figure 4.2: The real ($\Re$) and imaginary ($\Im$) components of the normalised mechanical displacements (u_i) as a function of depth in Sample 1 for the Rayleigh-like mode at 2.9 GHz. The two horizontal black lines indicate the position of the YIG layer with depth zero at the GGG/YIG interface. These displacements are calculated using the model described in Section 3.1 and show the characteristic exponential decay in amplitude of the SAW.

The strains can be calculated from these displacements using Eq. (3.6). Tab. 4.2 shows the normalised strains for the Rayleigh-like mode at 2.9 GHz in Sample 1 averaged over the YIG layer. The S_{xx}, S_{zz}, and S_{xz} strain components are dominant, with an approximately 90° phase shift between S_{xx} and S_{xz}, as expected [108].

Table 4.2: The normalised real ($\mathfrak{R}$) and imaginary ($\mathfrak{I}$) strain components (S_{ij}) for the Rayleigh-like mode at 2.9 GHz in Sample 1 averaged over the YIG layer.

	S_{xx}	S_{yy}	S_{zz}	S_{xy}	S_{xz}	S_{yz}
$\mathfrak{R}(S_{ij})$	-0.52	0.00	0.67	0.00	-1.00	0.02
$\mathfrak{I}(S_{ij})$	-0.73	0.00	0.94	-0.01	0.74	-0.01

Additionally, the wavevector of the 2.9 GHz SAW is calculated to be 6.7×10^6 m^{-1} from the dispersion relation.

Note that a SAW frequency of 2.9 GHz is chosen as this is the frequency used in the experiments in Chapter 5.

4.4 The calculated spin-wave intensity

Using these parameters, the expected spin-wave excitation, as a function of the angle and magnitude of the applied external magnetic field, is calculated for the magnetic driving field induced by a 2.9 GHz Rayleigh-like SAW in Sample 1. Fig. 4.3 shows the resulting colour map of the normalised $|M_z|^2$ component. Note a limit of 2% intensity has been set, below which the normalised $|M_z|^2$ component is set to white to aid in visualisation. Additionally, note that the value of $|M_z|^2$ is calculated as the integrated micro-focused Brillouin Light Scattering intensity is proportional to the spin-wave intensity and, therefore, $|M_z|^2$ in this case, which will aid with later comparison to experimental results.

Referring back to Fig. 1.2, with the magnetic field parallel to the SAW and, therefore, the spin-wave propagation direction, we are in the backward volume magnetostatic spin wave (BVMSW) geometry. By comparison, when the magnetic field is in-plane and perpendicular to the spin-wave propagation direction, the magnetostatic surface spin wave (MSSW) geometry is realised. To aid in the following discussion, the dispersion relations for a 103 nm YIG film are plotted in Fig. 4.4, using the parameters from Section 4.3, for the simple case of dipolar spin waves [10]. Magnetic fields of 20 mT and 50 mT are chosen as these are approximately the lower and upper limits of the excitation fields shown in Fig. 4.3.

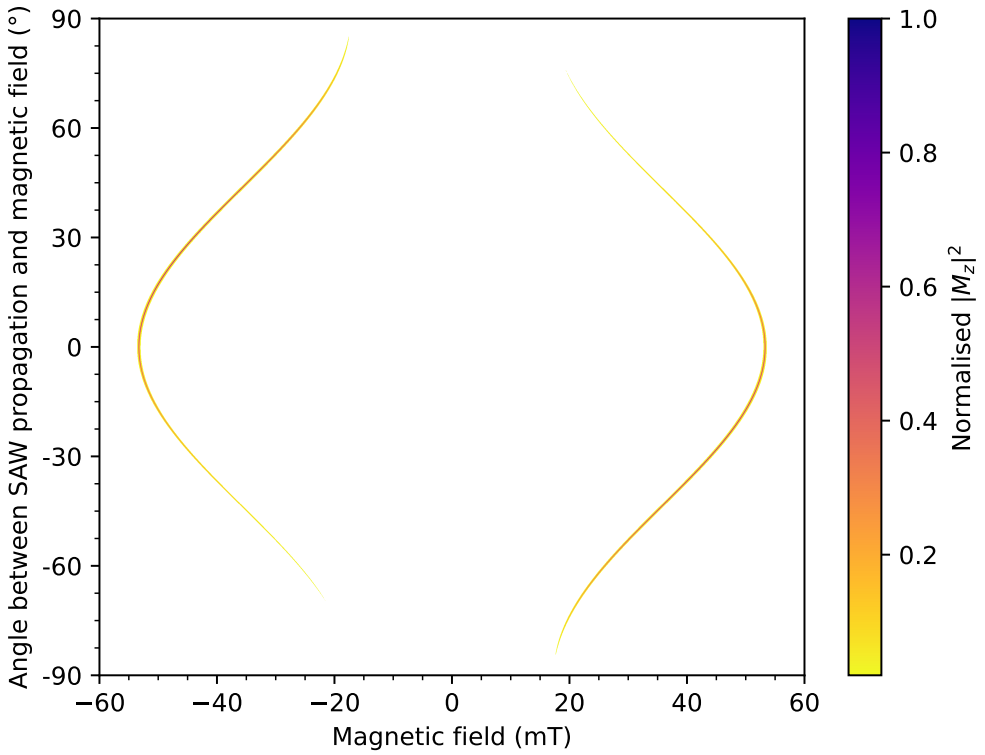

Figure 4.3: Colour map showing the normalised $|M_z|^2$ component as a function of both the magnitude of the magnetic field and the angle between the direction of the SAW propagation and the applied magnetic field. The values are calculated for a 103 nm YIG film with a SAW excitation frequency of 2.9GHz; the other parameters are described in Section 4.3. At 0°, the non-zero $|M_z|^2$ value is reciprocal for positive and negative magnetic field values. Moving towards 90°, the non-zero $|M_z|^2$ component becomes non-reciprocal, with a larger value at negative magnetic fields. The magnetic field values also decrease in magnitude. Close to ±90°, the $|M_z|^2$ component is zero everywhere, indicating no spin waves are excited. Note a limit of 2% intensity has been set, below which the $|M_z|^2$ component is set to zero/white.

From Eq. (4.18), if we take the equilibrium magnetisation to be in-plane, $\theta_0 = 90°$, due to the relatively large external fields at which spin-wave excitation takes place, we have the following expression for the driving magnetic fields,

$$\begin{aligned}\mu_0 h_1 =& 2b_2\Big(S_{xz}\cos\phi_0 + S_{yz}\sin\phi_0\Big)\\ \mu_0 h_2 =& 2b_1\Big(S_{xx} - S_{yy}\Big)\sin\phi_0\cos\phi_0 - 2b_2\Big(S_{xy}\cos 2\phi_0\Big).\end{aligned} \tag{4.24}$$

Furthermore, from Tab. 4.2, $S_{yy} = 0$, $S_{xy} \approx 0$, and $S_{yz} \approx 0$, giving the approximate expression,

$$\begin{aligned}\mu_0 h_1 &\approx 2b_2 S_{xz}\cos\phi_0\\ \mu_0 h_2 &\approx 2b_1 S_{xx}\sin\phi_0\cos\phi_0.\end{aligned} \tag{4.25}$$

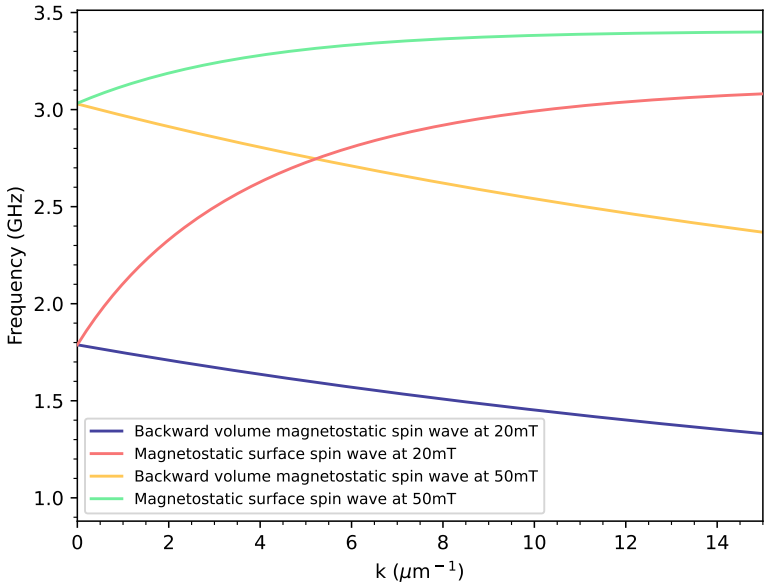

Figure 4.4: The calculated dispersion relations for dipolar spin waves propagating in a 103 nm thick YIG film with the parameters from Section 4.3. In blue (20 mT) and yellow (50 mT), the dispersion relations for the backward volume magnetostatic spin waves are shown, where the magnetic field is parallel to the propagation direction. In red (20 mT) and green (50 mT), the dispersion relations for the magnetostatic surface spin wave are plotted, where the magnetic field is in-plane and perpendicular to the propagation direction.

Referring to Fig. 4.3 and considering the zero degree excitation values, the BVMSW geometry, we see reciprocal spin-wave excitation at positive and negative field values due to the symmetry of the driving field; $\phi_0 = 0$, giving $\mu_0 h_1 \approx 2b_2 S_{xz}$ and $\mu_0 h_2 \approx 0$. As the angle between the propagation direction and magnetic field is increased, both components, h_1 and h_2, of the driving field are non-zero, giving rise to the observed non-reciprocity in Fig. 4.3 due to the helicity mismatch.

As the angle increases, the geometry approaches that of the MSSWs. As seen in Fig. 4.4, the MSSWs are higher in frequency for the same magnetic field and wavevector when compared to the equivalent BVMSWs. However, comparing the 20 mT (red) curve to 50 mT (green) curve, we see that by decreasing the magnetic field, the spin-wave frequency is downshifted. This explains the decreasing magnetic field values of the spin-wave excitation from 0° to 90° seen in Fig. 4.3. Finally, with the magnetic field perpendicular to the propagation direction, the MSSW geometry, the driving fields are zero, and hence, no spin-wave excitation is observed. Based

on this discussion, the calculated spin-wave excitation frequencies and observed non-reciprocity appear sensible.

As a final note, the spin-wave velocity decreases with increasing YIG film thickness. Although this reduced velocity could prove an issue if trying to measure the spin waves directly, it does not inhibit the coupling of SAWs with spin waves. Furthermore, as will be shown in the following chapter, no direct measurements of the spin waves are made, and as such, an analysis of the spin wave velocities is not required.

5

Micro-focused Brillouin light scattering

In this chapter, micro-focused Brillouin Light Scattering (μ-BLS) results from Samples 1 & 2 are presented. First, we discuss the relevant theory behind μ-BLS and describe the experimental set-up used. Following this, experimental results showing the IDT frequency response and the group velocity as a function of frequency are presented and compared to the numerical model. Finally, results showing the coupling between the SAWs and the spin waves are shown.

5.1 Theoretical overview

In the quantum mechanical picture, the basic principle on which μ-BLS is founded is relatively simple. An inelastically scattered photon can create a phonon or magnon, the Stokes process, or annihilate a phonon or magnon, the anti-Stokes process. This is shown schematically in Fig. 5.1. As momentum and energy are conserved, we can see from the diagram that information about the phonon or magnon can be inferred by probing the scattered light. For example, with laser light of known frequency, the frequency of the phonon or magnon can be determined by calculating the difference in frequency between the incident and scattered light.

In addition to this, magnons cause a 90° rotation in the polarisation of light [99]. Therefore, by using polarising filters, it is possible to differentiate between phonons,

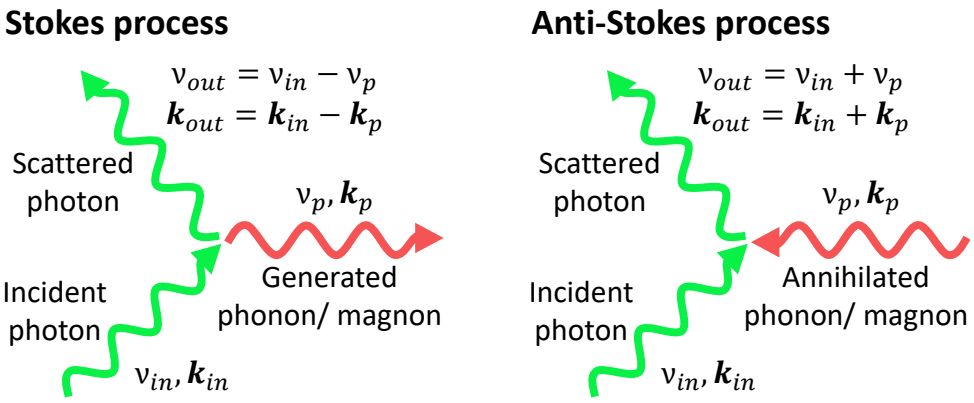

Figure 5.1: Schematic depicting the inelastic scattering of light with phonons or magnons, ν denotes the frequency and $\boldsymbol{k}$ the wavevector. The Stokes process (left) shows the generation of a phonon or magnon from the inelastic scattering, while the anti-Stokes process (right) shows the annihilation of a phonon or magnon. By detecting the scattered light in a Brillouin light scattering (BLS) microscope it is possible to infer information about the phonon or magnon.

which cause no rotation in the polarisation, and magnons, which do cause a rotation in the polarisation. Finally, we note that the intensity of the inelastically scattered light is directly proportional to the intensity of the acoustic or spin wave from which it was scattered, meaning the waves can be directly visualised. For further information on BLS, Demokritov et al. [14] and Sebastian et al. [117] provide excellent overviews of the theory and experimental methods.

5.2 The micro-focused Brillouin light scattering microscope

Although conceptually simple, the design of an optical set-up to measure the inelastically scattered photons is rather complicated. This is primarily due to the challenge of resolving the small frequency shift between the incident and scattered light. Typically, and indeed in the case of this thesis, a 532 nm wavelength green laser is used, which has a corresponding frequency of about 600 THz. As the SAWs we are interested in imaging are of the order of a few gigahertz, we need to resolve frequency shifts of around 1 part in 10^8 for satisfactory resolution. To achieve this resolution, the core of the BLS setup consists of a tandem Fabry-Pérot interferometer (TFPI).

5.2.1 The tandem Fabry-Pérot interferometer

As the name suggests, the TFPI consists of two Fabry-Pérot interferometers (FPIs) mounted with a small angle between them. A FPI consists of two partially reflective parallel mirrors or etalons; when light enters the interferometer, it is partially transmitted through the first mirror and then partially reflected back and forth between the two mirrors. As the light waves reflect back and forth between the mirrors, they interfere with each other. For constructive interference, the condition

$$d = \frac{n\lambda}{2} \tag{5.1}$$

must be satisfied, where d is the mirror spacing, λ the wavelength, and the integer n is the transmission order. By scanning the mirror spacing, this condition can be met for different wavelengths of light, thus enabling the detection of scattered light.

However, when using a single FPI, it is not possible to differentiate between the transmission orders, and, as such, it cannot be determined whether a transmission peak was generated by a Stokes or anti-Stokes process. An illustration of the transmission function from an example signal, with a central reference peak, and the arising ambiguity is shown in the top panel of Fig. 5.2. To overcome this, the TFPI is used.

The TFPI contains two FPIs mounted with a small angle, α, and a mirror between them, as depicted schematically in Fig. 5.3. By adjusting the position of the mirror, the transmission condition for a reference signal can be fulfilled simultaneously by both FPIs for one transmission order, enabling mode discrimination as is shown in the bottom panel of Fig. 5.2.

The reference signal directly enters the TFPI without being scattered from the sample, providing the zero position in the measured spectrum. The inelastically scattered light passes through each etalon three times to increase contrast. Finally, note that the frequency range the TFPI can access, the free spectral range, and the frequency resolution are coupled. Therefore, the minimum acceptable frequency range should be chosen to maximise the resolution.

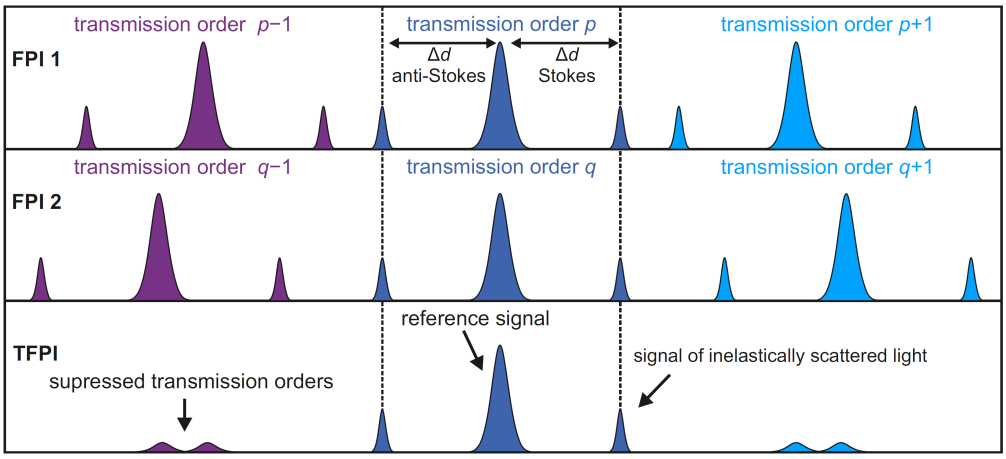

Figure 5.2: Schematic of the transmission spectra in a tandem Fabry-Pérot interferometer. The top and middle display the spectra of the two individual Fabry-Pérot interferometers (FPIs). The bottom shows how, by measuring with the two FPIs simultaneously, the higher/lower transmission orders can be suppressed, allowing mode discrimination. The central reference peak corresponds to directly measured unscattered laser light, while the peak to the left is the anti-Stokes signal, and the peak to the right is the Stokes signal. Figure adapted from [6].

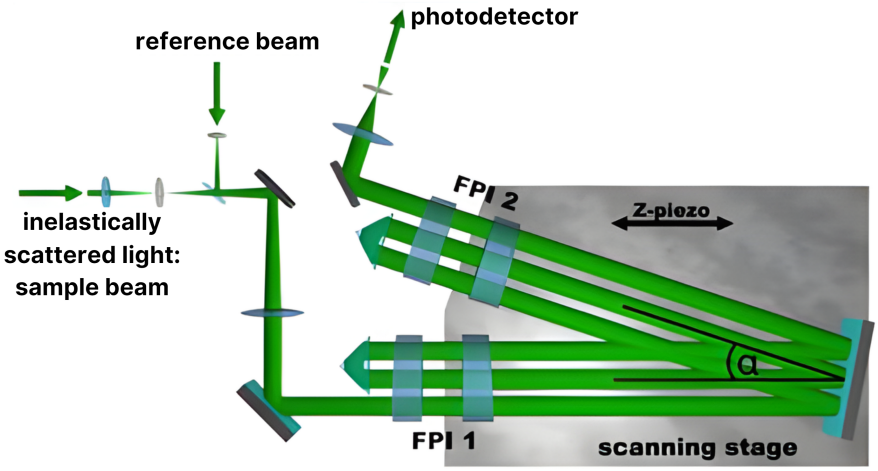

Figure 5.3: Schematic of a tandem Fabry-Pérot interferometer (TFPI). The unscattered reference laser beam and inelastically scattered light enter the TFPI. The light then passes through each etalon three times to increase the contrast before travelling to the photodetector. The scanning stage of the mirror between the individual FPIs is varied to fulfil the transmission condition for the two FPIs, mounted with the angle α between them, simultaneously. Adapted from [117].

5.2.2 Micro-focused Brillouin light scattering

There are two main types of BLS microscope: k-resolved and spatially resolved or micro-focused [117–119]. In this thesis, μ-BLS was used to image the spatial distribution of SAWs across the sample. To realise this, the laser beam is focused onto the sample through a microscope objective to probe a small spot size; the spatial resolution is around 250 nm. As the microscope lens is fully illuminated and has a small working distance, the direction of the back-scattered light is not well defined and, therefore, resolution of the wavevector is not possible; only the frequency and spatial position of the detected phonon or magnon can be measured. This is a realisation of Heisenberg's Uncertainty Principle.

5.2.3 An overview of the microscope

The general idea, therefore, is that a collimated polarised laser beam is first passed through a beam splitter to generate the reference beam that travels directly to the TFPI, and the beam that passes through the microscope objective to be focused onto the sample. The back-reflected light is guided back through the TFPI, and a spectrum such as that shown in the lower panel of Fig. 5.2 is generated by scanning the mirror spacings and using a single photon detector to measure the intensity of the transmitted light.

The sample is mounted on a three-dimensional translational stage to allow focusing and movement in the film plane. Simultaneous imaging of the sample surface by an LED coupled to a CCD camera allows the identification of the region of interest. Additionally, a rotatable $\lambda/2$ plate is used to enable differentiation between phonons and magnons using the aforementioned polarisation-dependent scattering [99]. A detailed description of the set-up can be found in Schneider's thesis [6].

5.3 The experimental set-up

A schematic of the experimental arrangement can be seen in Fig. 5.4, where the IDT is directly excited by a microwave signal. This generates SAWs in the sample,

and the SAW intensity is measured by the 532 nm wavelength μ-BLS microscope. A half-wave plate suppresses possible magnon-induced signals.

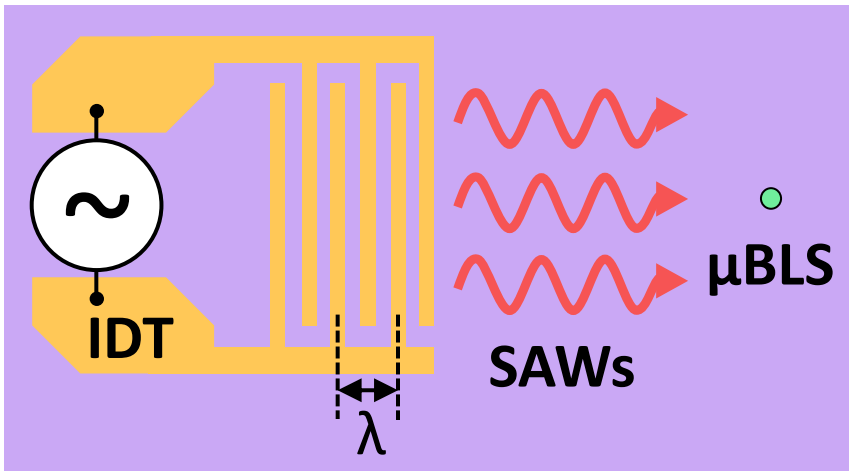

Figure 5.4: Schematic of the μ-BLS experiment showing an interdigital transducer excited by a microwave source. The red arrows indicate the excited SAWs and the μ-BLS laser spot is indicated by the green dot, which is used to measure the SAWs.

To excite SAWs, the IDT is contacted using a microwave GGB Industries Picoprobe with a ground-signal-ground footprint and pitch of 200 μm, connected to an HP Microwave Signal Generator and an amplifier. A power of 30 dBm was used for most measurements. The contacting of the sample can be seen in Fig. 5.5.

The sample is positioned on a three-dimensional translational stage, which is located between the pole faces of an electromagnet. This allows the application of a magnetic field, which can be used to look for SAW-spin wave coupling. A photograph of the sample stage prior to mounting a sample can be seen in Fig. 5.6. Note that a Hall probe is used to measure the magnetic field.

5.3.1 Time-resolved micro-focused Brillouin light scattering

In addition to standard μ-BLS measurements, time-resolved data is also required to measure the SAW group velocities. A schematic of the time-resolved μ-BLS setup is shown in Fig. 5.7. A pulse generator is used to trigger a μ-BLS measurement window; during this window, a microwave switch is opened for approximately 600 ns, allowing a microwave pulse of fixed frequency to excite the IDT. By measuring

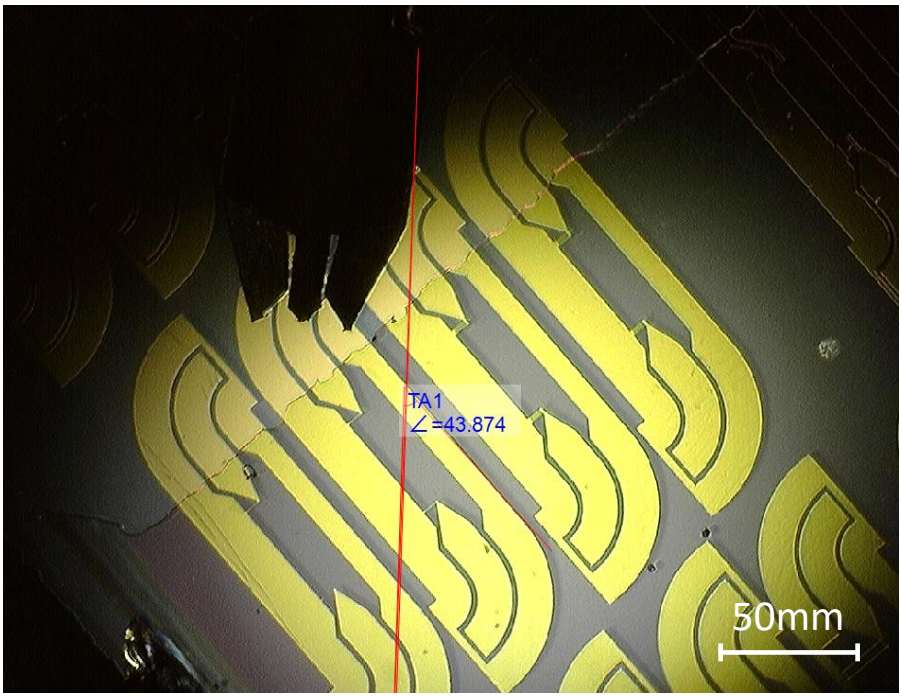

Figure 5.5: Photograph of the Picoprobe contacting a gold IDT. The Picoprobe can be seen as the three black prongs (ground-signal-ground) contacting the outer ground pads and the inner signal pad of the gold IDT. A slightly ragged line at approximately 45° across the sample, running parallel to the IDT fingers, can be seen. To the upper left of this line, in the Picoprobe region, the ZnO has been etched away to allow direct electrical contact with the gold pads.

at two different spatial positions, the resulting frequency against time μ-BLS measurement data can be used to determine the group velocity of the SAW, as will be described in Section 5.4.2.

All the μ-BLS measurement data was gathered at RPTU in collaboration with Prof. Dr. Weiler's group.

5.4 Experimental results

This section presents the experimental results used to characterise the SAWs. Note that all these measurements were taken with zero external magnetic field.

5.4.1 Frequency response data

First, the frequency response of a 6 finger IDT on Sample 1 was measured and compared to the expected excitation frequencies from the numerical calculation.

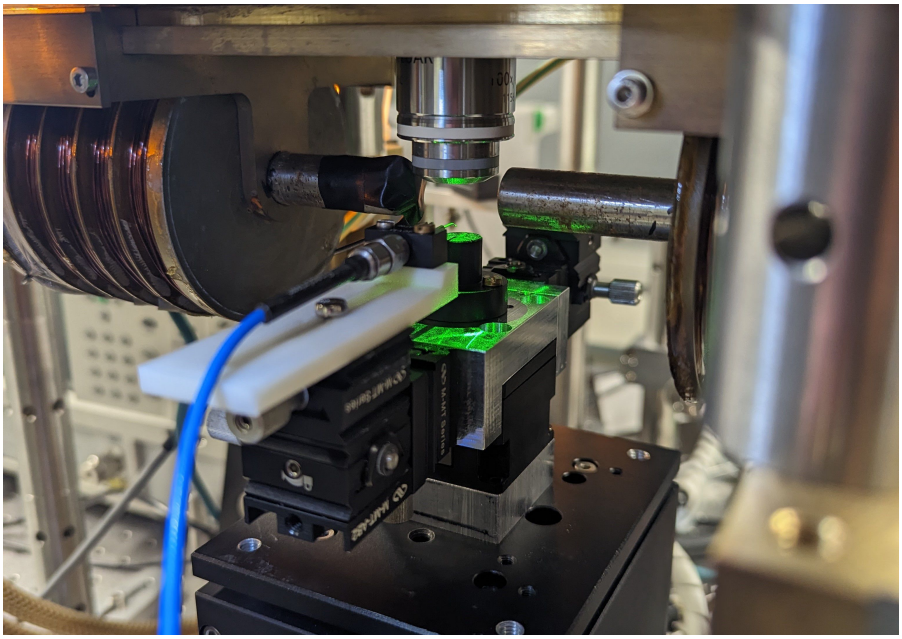

Figure 5.6: Photograph of the μ-BLS sample stage. The black upright cylindrical sample stage is illumined by the green laser light from the microscope objective above. This sample stage is mounted on an (x, y, z) translation stage. The Picoprobe can be seen attached to the blue microwave cable, with the tip above the sample stage illuminated by the laser; it is mounted to an (x, y, z) translation stage to allow accurate contacting of the IDT pads. The pole faces of the electromagnets are located on either side of the microscope objective.

This comparison is shown in Fig. 5.8b. The laser spot was positioned centrally relative to the IDT aperture and approximately 1 μm along the SAW propagation path to maximise the signal. We expect the highest intensity peak to correspond to the fundamental frequency, which is determined by the 2.8 μm periodicity/ wavelength of the IDT according to $f = v/\lambda$. Moreover, we should see higher order modes corresponding to λ/p where p is an odd integer, remembering that a net electric field between the IDT fingers is required to excite a SAW.

We see the fundamental frequency occurs at approximately 1.1 GHz. The coloured horizontal lines indicate the calculated excitation frequencies of the IDT and show good agreement with the peaks in the experimental data. Note that the first higher-order harmonic at 2.9 GHz should be sufficiently high in frequency to enable coupling to spin waves.

The additional peaks in Fig. 5.8b are attributed to sidebands in the IDT frequency response. In the spatial domain, the IDT fingers can be represented by

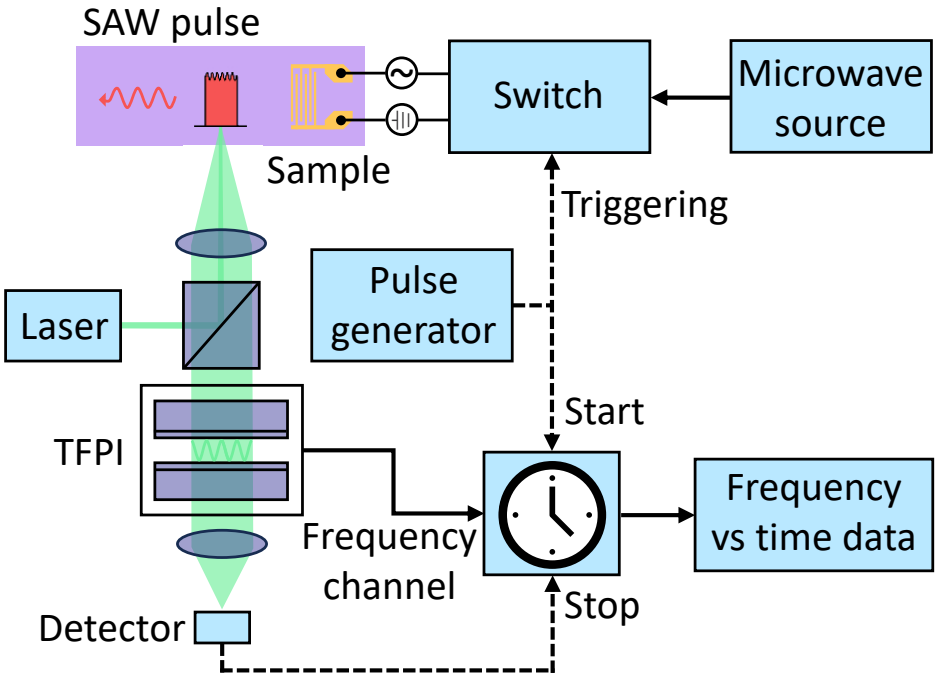

Figure 5.7: Schematic of the time-resolved μ-BLS spectroscopy setup. A pulse generator is used to trigger the start and end of a BLS measurement window during which a SAW pulse, well defined in time, is also triggered. This pulse is realised using a microwave source and a fast microwave switch. The resulting BLS spectrum comprises of frequency against time data. Figure adapted from [120].

a series of delta functions at the locations of the fingers convolved with a top hat function representing the finite finger width. The series of delta functions is given by

$$f(x) = \sum_{n=-\frac{N}{2}}^{\frac{N}{2}} \delta(x - 4dn), \tag{5.2}$$

where N is the total number of finger pairs, and $4d$ is the periodicity of the finger pairs. Taking the Fourier transform, to consider the frequency domain, and convolving with the top hat function, the intensity profile is given by

$$I = I_0 \left(\frac{\sin\left((N+1)2kd\right)}{\sin\left(2kd\right)} \right)^2 \cdot \left(\mathrm{sinc}\left(\frac{kd}{2} \right) \right)^2. \tag{5.3}$$

The oscillatory nature of this function is responsible for the sidebands observed in the IDT frequency response [121]. Furthermore, from this expression, we can see that by increasing the number of finger pairs, the Fourier transform will have more oscillations within the same frequency range, narrowing the width of the sidebands.

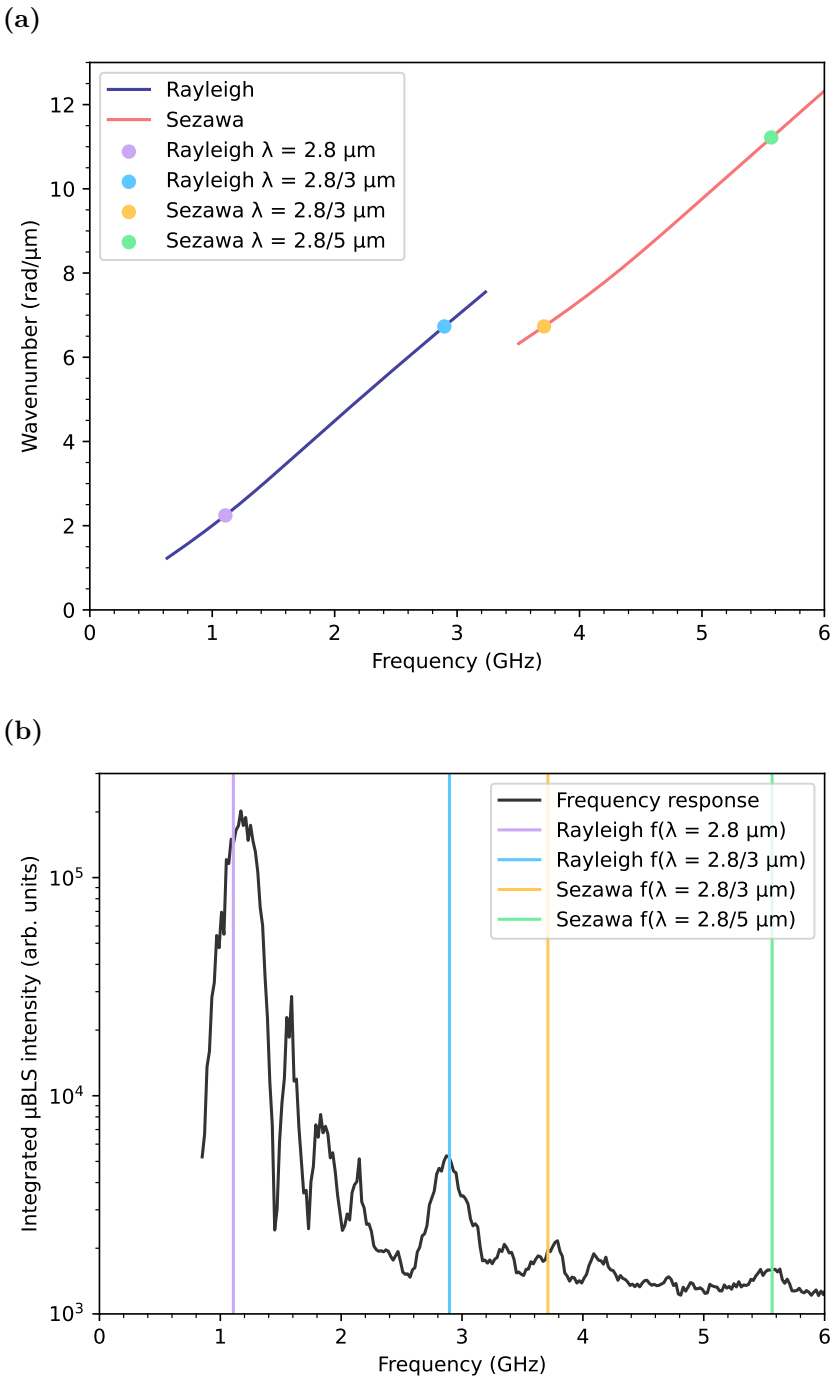

Figure 5.8: Comparison of μ-BLS data frequency response data with the theoretical model. (a) The calculated dispersion relation for the Rayleigh-like mode, dark blue line, and the first Sezawa-like mode, red line, for Sample 1. The four points indicate the expected excitation frequencies of the fixed $\lambda = 2.8\,\mu$m transducers, accounting for the accessible higher harmonics. (b) Experimental data, in dark grey, showing the frequency response of the 6 finger interdigital transducer measured on Sample 1 by μ-BLS. The coloured vertical lines indicate the resonance frequencies at which the $\lambda = 2.8\,\mu$m transducer is expected to excite surface acoustic waves based on the values calculated from (a).

For example, if the number of finger pairs increases from 6 to 20, the number of oscillations observed in the same frequency range should increase by a factor of three.

Fig. 5.9 shows data equivalent to Fig. 5.8b for a 20 finger IDT. Examining the region between approximately 1.4 GHz and 2 GHz, we can see approximately six peaks, compared to the two observed in Fig. 5.8b. This is in agreement with the explanation that these additional peaks are sidebands rather than additional modes. Note that the lack of the higher order peaks in Fig. 5.9, compared to Fig. 5.8b, is likely owing to small imperfections in the fingers. Any slight non-uniformity in the fingers will inhibit perfect constructive interference, thus reducing the intensity of the frequency response. Assuming there is an increasing total number of imperfections as a function of the number of fingers, this effect will be more significant for the 20 finger pair IDT.

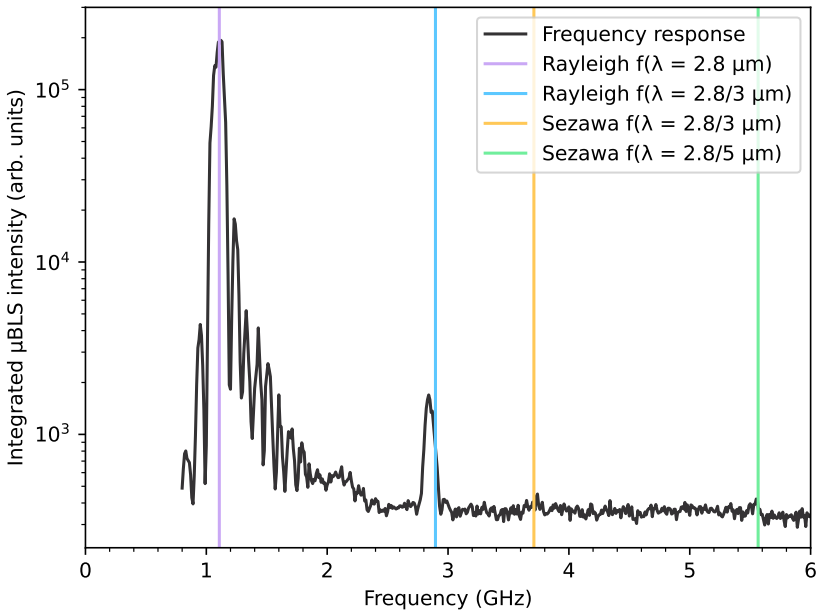

Figure 5.9: Experimental data, in dark grey, showing the frequency response of the 20 finger interdigital transducer measured on Sample 1 by μ-BLS. The coloured vertical lines indicate the resonance frequencies at which the $\lambda = 2.8\,\mu$m transducer is expected to excite surface acoustic waves. The increased number of side peaks in the same frequency range, compared to the frequency response shown in Fig. 5.8b, supports the theory that these are sidebands.

Note that calculating the Fourier transform of the frequency response will not give the spatial function directly as the phase velocity of the SAWs varies with

frequency, and there is also a frequency-dependent coupling coefficient. In addition, the higher-order modes corresponding to different spatial periodicities are present. Calculating the expected frequency response for an IDT from the geometry for a layered system is complex [121] and deemed unnecessary given the good agreement between the model and the experimental results when considering the sideband explanation for the additional peaks.

5.4.2 Group velocity data

Second, time-resolved measurements are used to calculate the phonon group velocities at fixed microwave frequencies. An example of the resultant BLS intensity as a function of time can be seen in Fig. 5.10a. Top-hat-like intensity profiles can be seen, where high intensities correspond to the presence of a SAW at the laser spot position.

The laser spot was initially positioned centrally next to the IDT and then moved away from the IDT along the SAW propagation direction in equal-sized steps. At each step, a BLS measurement is taken corresponding to the different coloured lines from purple to red in Fig. 5.10a. This data is then fitted using a least squares regression with the sigmoidal Boltzmann function to smoothly approximate the Heaviside step function

$$I = C + \frac{D - C}{1 + e^{-\frac{t - t_0}{B}}}\,, \tag{5.4}$$

where I is the BLS intensity, t is the time, and B, C, D, and t_0 are constants. An example Boltzmann fit is shown by the black dotted curve fitting the red BLS data in Fig. 5.10a.

From these fits, the constant t_0 is extracted, the position of the falling edge of the SAW pulse, with an associated fitting error. Combining this with the known laser spot position, we can plot the SAW propagation distance from the IDT as a function of t_0, Fig. 5.10b. Alongside the fitting error in t_0, we take into account experimental errors of 2 ns for time-based measurements and 1 μm for the microscope position

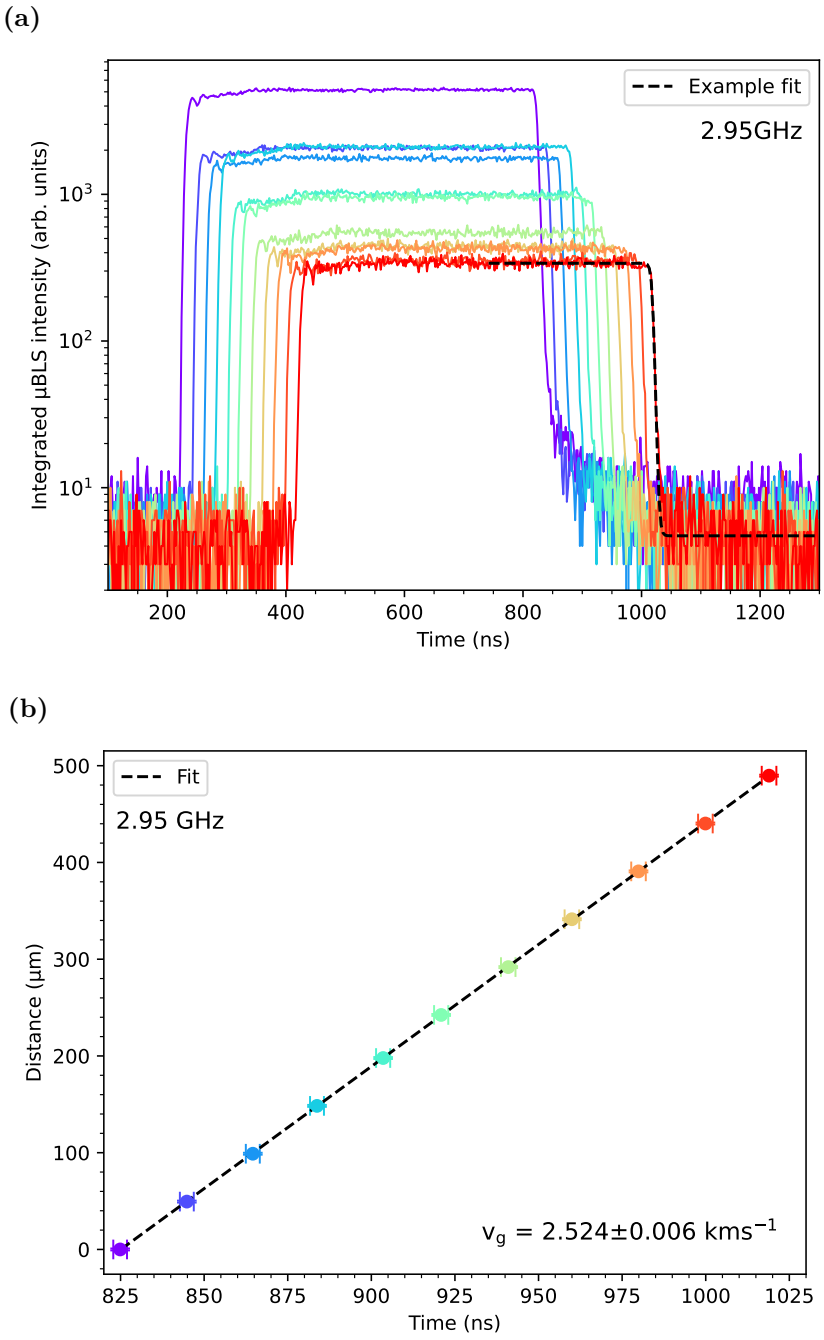

Figure 5.10: Time-resolved μ-BLS data for the 6 finger IDT on Sample 1 at 2.95 GHz. (a) Experimental data showing the measured BLS intensity as a function of time. The different colours show data taken at different laser spot positions; purple corresponds to the position closest to the IDT, and the colour progression through to red goes with increasing SAW propagation distance. The black dotted line shows a Boltzmann function fitted to the red data taken furthest from the IDT. (b) The time at the centre of the falling edge of the SAW pulse, extracted by fitting the data in Fig. 5.10a, as a function of the distance of the laser spot from the IDT. The dotted black line was fitted to the data to find the group velocity.

stabilisation. Using orthogonal distance regression, a straight line is fitted to the data to determine the group velocity at a fixed frequency.

The results of this fitting process can be seen for Sample 1 over a range of 0.85 to 5.55 GHz in Fig. 5.11a and Sample 2 over a range of 0.8 to 7.17 GHz in Fig. 5.11b. The experimentally determined group velocities are shown, with their associated errors, in light blue and green as a function of the SAW excitation frequency. For Sample 1, the group velocities were measured for two IDT structures, one with 6 fingers (light blue) and the other with 20 fingers (green). These group velocities were determined from multipoint linescans; that is to say, the laser spot was scanned over multiple points in space, as in Fig. 5.10a.

For Sample 2, all measurements were made on the same 6 finger IDT. In light blue, we again have group velocities determined from multipoint linescans. In green, however, the group velocities were calculated from two-point linescans, where the laser spot was positioned at only two points in space, one next to the IDT and the other at the maximum distance measured from the IDT of $\sim 500\,\mu$m. There is good agreement between the two-point and multipoint measurements showing the accuracy of the technique.

Fig. 5.11 also shows the numerically calculated group velocities of the Rayleigh-like mode in dark blue and the Sezawa-like mode in red for Samples 1 & 2. Given the caveats discussed in Section 3.4, the agreement between the numerical model and the experimental data is excellent, with the largest discrepancies, in general, occurring for the points with the largest measurement errors. These large errors occur due to the low excitation efficiency of the IDT at these frequencies, meaning the top-hat-like intensity profiles become more noisy. In particular, the narrower bandwidth 20 finger IDT tends to show larger errors when off-resonance, as expected.

In general, the data fits the curvature well, and we can differentiate between the Rayleigh and Sezawa-like modes. These results show the non-linearity in the phonon dispersion relation can be measured for these complex layered structures to a high accuracy using time-resolved μ-BLS. Furthermore, good agreement with the numerical model is demonstrated, thus verifying the model is sufficient within the

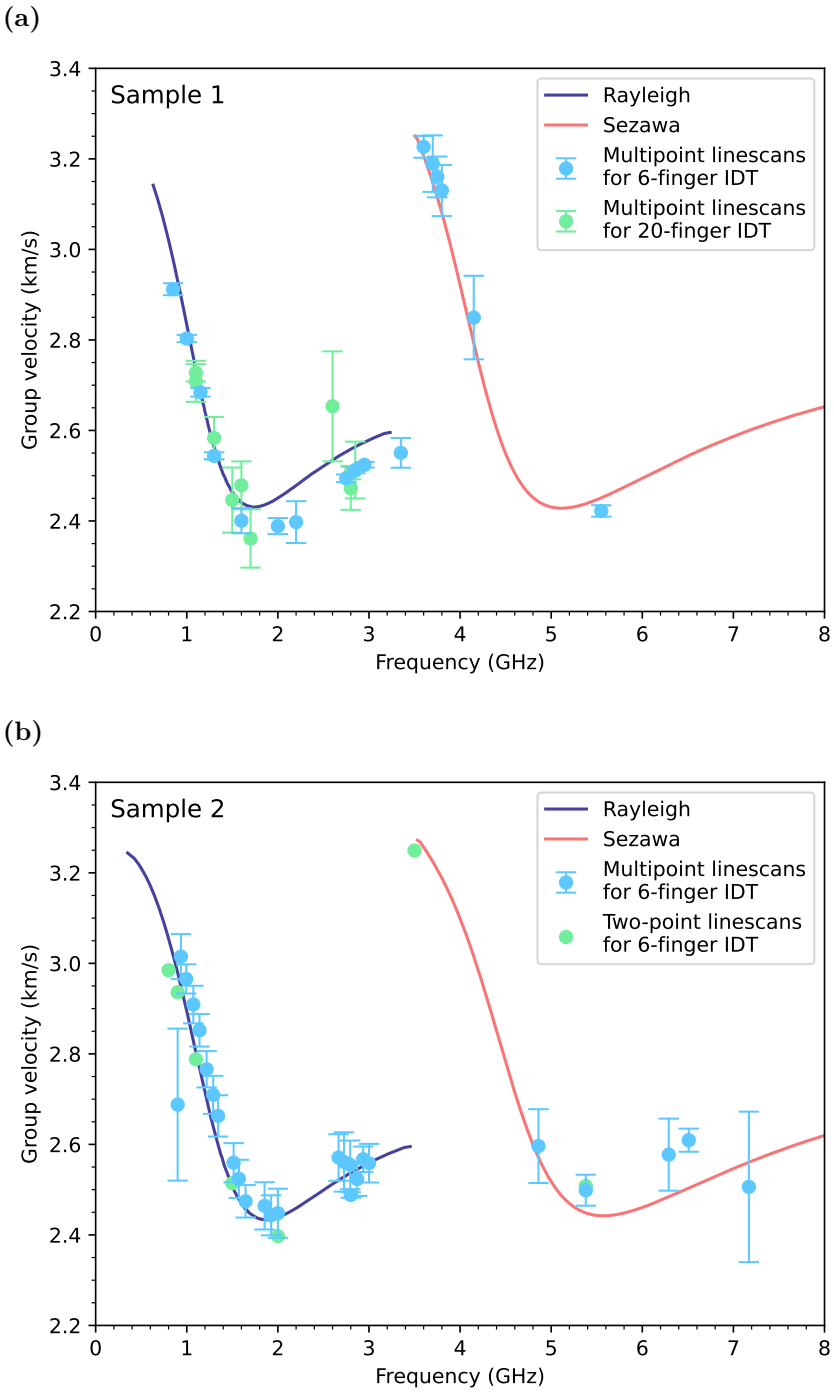

Figure 5.11: Comparison of the experimental group velocity data with the theoretical calculation. The calculated Rayleigh and Sezawa-like mode group velocities are shown as a function of frequency by the dark blue and red lines. (a) Experimental group velocity data for Sample 1, the light blue points show data for a 6 finger IDT and the green points for a 20 finger IDT. (b) Experimental group velocity data for a 6 finger IDT on Sample 2. In blue, multipoint linescans are shown, where the laser spot is scanned over multiple points in space. In green, two-point linescans are shown, where the laser spot measures at only two points in space. The group velocities were calculated as shown in Fig. 5.10.

assumptions made to interpret our experimental data. Additionally, it is noteworthy that the experimental results agree with the model for two different samples with different ZnO and YIG thicknesses and three different IDT structures.

5.4.3 Decay length

Finally, using the amplitudes from the Boltzmann fits, $A = D - C$, from Eq. (5.4), the phonon decay lengths can be estimated by fitting the equation

$$A(x_1) = A_0 e^{-\frac{x_1}{\Lambda}}, \tag{5.5}$$

where A_0 is the initial amplitude, Λ the decay length, and x_1 the propagation length of the SAW. Due to the aforementioned reduction in experimental data quality when off-resonance, this decay length is only calculated for values near the first accessible harmonic frequency of the IDT at 2.9 GHz.

Taking a weighted average, we find a decay length of $127 \pm 31\,\mu$m for the 6 finger IDT on Sample 1, consistent with the value of $124 \pm 65\,\mu$m for the 6 finger IDT on Sample 2. The relatively large errors in these values are thought to result from variations in the reflectivity of the surface of the samples, which could result from defects in the film or surface particles. We note that etching away the ZnO along the propagation path after the excitation region may increase the decay length, given the dead layer is not crystallographically ordered and, therefore, will have increased scattering.

5.5 The coupling of SAWs and spin waves

Having demonstrated a successful method for generating gigahertz SAWs; the final experiment carried out was to look for SAW-spin wave coupling. This was done by exciting the first accessible higher harmonic of the 6 finger IDT at 2.9 GHz on Sample 1 and scanning the external magnetic field in the plane of the thin film. The μ-BLS laser spot was positioned centrally with respect to the aperture and moved to a position of approximately $450\,\mu$m along the SAW propagation path. This was to ensure the SAWs had propagated a sufficient distance to enable

the SAW-spin wave coupling to occur, with a dip anticipated in the expected SAW intensity when coupling occurs.

The sample was positioned such that there was an angle of $-49.2°$ between the direction of SAW propagation and the applied magnetic field direction. The 6 finger IDT was excited continuously at 2.9 GHz using a microwave signal generator and amplifier at a power of 30 dBm while the electromagnets were swept from -40 to +40 mT. The resulting integrated μ-BLS intensity at 2.9 GHz as a function of the applied magnetic field can be seen in Fig. 5.12.

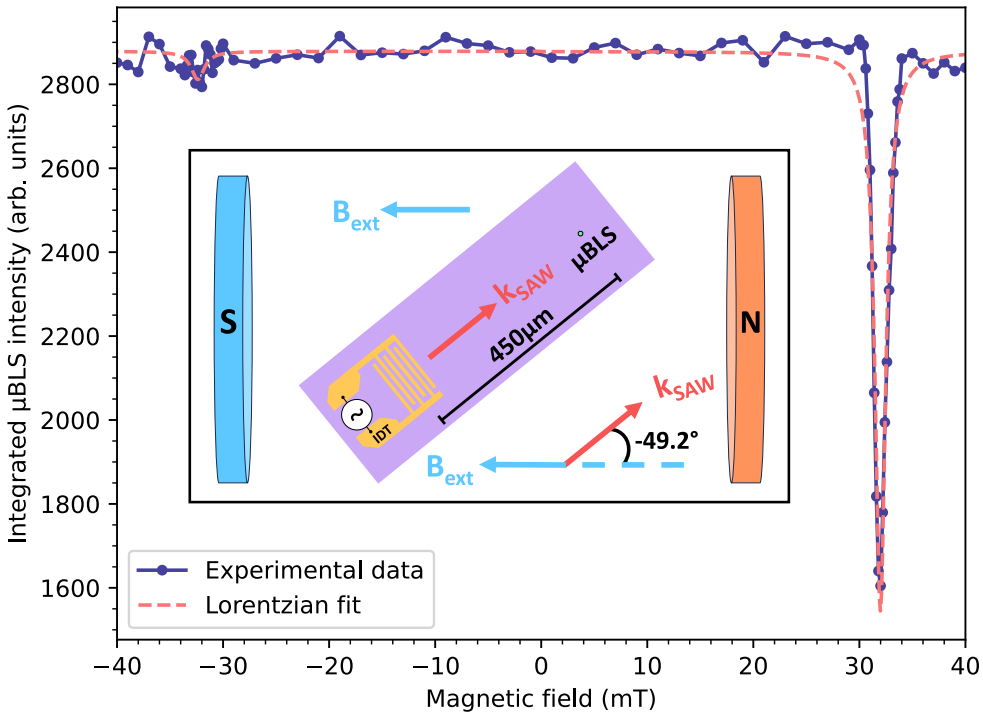

Figure 5.12: Experimental data, in blue, showing the μ-BLS measured SAW intensity at 2.9 GHz as a function of the applied magnetic field strength for an angle of $-49.2°$ between the direction of SAW propagation and the applied magnetic field. Measured on Sample 1 using the 6 finger IDT. Lorentzians (red) are fitted to the dips. The dip at -32 mT is small and hard to distinguish from the background. The dip at $+32$ mT is significantly larger, showing the pronounced non-reciprocity of the SAW-spin wave coupling. This dip is fitted well with the Lorentzian. The insert shows a schematic of the experiment setup, where the μ-BLS laser spot is positioned approximately 450 μm along the SAW propagation path.

First and foremost, there is a significant dip in the detected SAW intensity at +32.0 mT. Given the magnetic field dependence, this appears to indicate SAW-spin

wave coupling. It is also clear that, as expected, there is a pronounced non-reciprocity; the opposing dip at −32.0 mT is extremely small and hard to measure above the background level fluctuations in intensity. In red, Lorentzians of the form

$$L(x) = C - \frac{A}{\pi} \frac{\Gamma/2}{(x - x_0)^2 + (\Gamma/2)^2} \tag{5.6}$$

were fitted to the data, where Γ is the linewidth, x_0 the centre of the dip, and A & C are constants. A linewidth of 1.20 mT was found for the dip at +32.0 mT. The opposing dip was fitted by using an initial guess with the same linewidth at the reciprocal field value.

A slice from the colour map in Fig. 4.3 at −49.2° is taken. This is multiplied by −1 to show the expected decrease in SAW intensity, proportional to $-|M_z|^2$, rather than spin-wave intensity, and then normalised according to the calculated Lorentzian amplitude from the experimentally measured dip at +32.0 mT. This intensity calculated from the model is plotted alongside the experimental data in Fig. 5.13 in red, taking the plateau of the Lorentzian to match that of the experimental data.

In general, there is fairly good agreement with the model. First, the peak position is almost perfect; there is a difference of 0.1 mT between the fitted peak positions, where a Lorentzian is also fitted to the theoretical results to extract the position and linewidth. This is likely a result of experimental errors. The angle between the field and the SAW propagation direction was measured using an image from an LED microscope. This is not especially accurate; therefore, we would estimate an error of ±1° on the measurement of this angle. This results in a value from the theory curve for the peak position of 32.1±0.6 mT, accounting for the observed 0.1 mT discrepancy in the field position.

The non-reciprocity is also approximately correct. The non-reciprocity ratio, which we define as the difference in the two dip amplitudes divided by the sum of the two dip amplitudes, is calculated to be 0.90 from the experimental data and 0.75 from the theoretical model. Note that the amplitude of the Lorentzian is given by $2A/\pi\Gamma$. As shown, the non-reciprocity is highly dependent on the strain parameters input into the model. Given the caveats discussed in Section 3.4 and that we assume

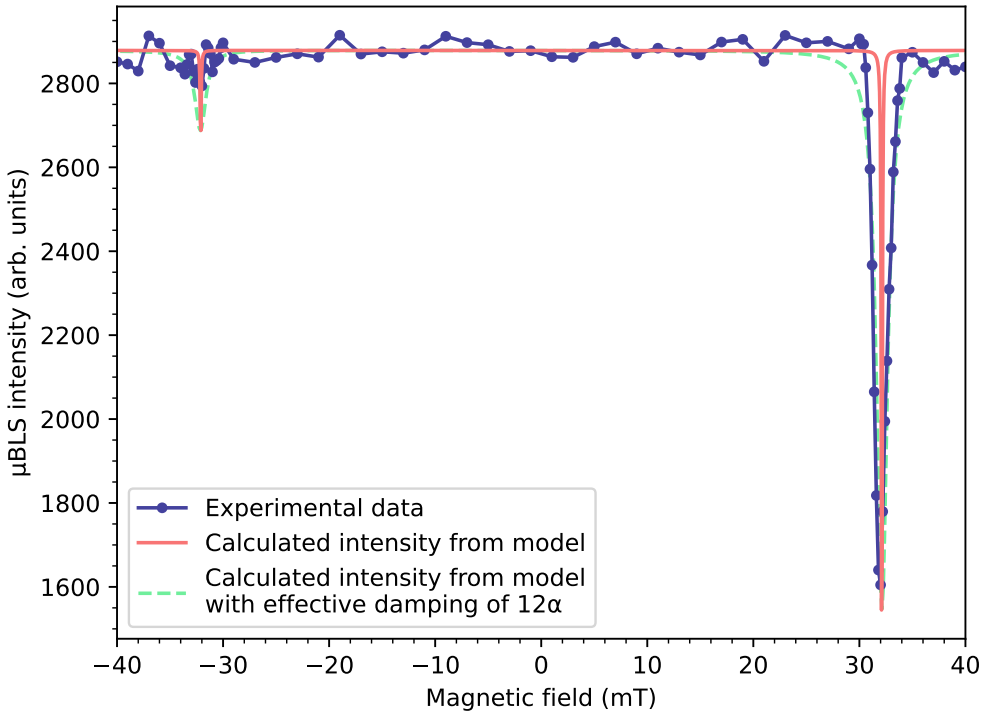

Figure 5.13: Comparison between the experimental and calculated dips in SAW intensity. Experimental data, in blue, shows the measured SAW intensity as a function of the applied magnetic field strength for an angle of $-49.2°$ between the direction of SAW propagation and the applied magnetic field direction. This is the same experimental data as in Fig. 5.12. The expected dips in SAW intensity calculated from the theoretical model are shown in red for the value of Gilbert damping shown in Tab. 4.1 and in green for an effective damping of 12 times this value. The theory curve is a horizontal slice taken from Fig. 4.3 at $-49.2°$. The peak position and observed non-reciprocity approximately fit the experimental data; however, an effective damping of 12α is required to fit the linewidth.

a uniform strain profile across the thickness of the YIG, it is unsurprising that there is some discrepancy. In fact, the agreement is surprisingly good, given there is no attempt to fit the non-reciprocity by modifying the strain parameters.

Therefore, the discrepancies are justifiable and relatively small regarding these two points. Where the experimental and theoretical models differ significantly is in the linewidth of the observed dips. The experimental results have a linewidth 12 times larger than the expected linewidth from the theoretical model. This is shown by the green dashed curve in Fig. 5.13, where the Gilbert damping parameter was increased by a factor of 12 to give an effective damping parameter, $\alpha_{\text{eff}} = 12\alpha$. This fits the experimental data fairly well, although there is a lack of curvature at the upper edges of the experimentally measured dip in SAW intensity. The

exact origin of this effective damping is not clear; however, a number of possible contributions are suggested.

Firstly, an additional term should be added to the Gilbert damping to account for the inhomogeneous line broadening [91], giving the effective FMR damping,

$$\alpha_{\text{eff}}^{\text{FMR}} = \frac{\gamma}{4\pi f}\mu_0 \Delta H + \alpha. \tag{5.7}$$

From the data provided by RPTU, $\mu_0 \Delta H \approx 0.4\,\text{mT}$ giving a value of $\alpha_{\text{eff}}^{\text{FMR}} \approx 4.8\alpha$, which gives a fairly sizeable increase to the damping.

Secondly, we have neglected any broadening that may occur due to the SAW lifetime. In other experiments with low SAW damping, due to the single crystal piezoelectric substrates, and high spin-wave damping [91, 99], this is a good assumption. However, in the case of YIG/ ZnO, the spin-wave lifetimes are relatively long, and the SAW lifetimes are relatively short. From the SAW decay length, $127 \pm 31\,\mu\text{m}$, calculated in Section 5.4.3, and with the calculated SAW group velocity of $2720\,\text{ms}^{-1}$, an estimate for the inverse SAW lifetime $1/\tau_{\text{SAW}}$ can be made. We find $1/\tau_{\text{SAW}} = 2.1 \pm 0.5{\times}10^7 \text{s}^{-1}$.

To estimate the inverse spin-wave lifetime, we use the expression for dipolar spin waves propagating at an angle, θ, to the magnetic field [10],

$$\frac{1}{\tau_{\text{SW}}} = \alpha\left(\omega_H + \frac{\omega_M}{2}\left(1 - G_{\text{SW}}\cos^2\theta\right)\right), \tag{5.8}$$

where G_{SW} is as defined in Eq. (4.10), $\omega_M = \gamma\mu_0 M_{\text{S}}$, and $\omega_H = \gamma B_0$, with $B_0 = 32.1\,\text{mT}$ and γ, the gyromagnetic ratio, as defined in Section 1.2.1. This gives a value of $1/\tau_{\text{SW}} = 1.0{\times}10^7$ and, therefore, $1/\tau_{\text{SAW}} \approx 2/\tau_{\text{SW}}$. Noting that linewidth is proportional to one over the lifetime, this likely gives an increased effective damping. To properly account for this effect, the fully coupled wave equation should be solved. This could also show if coherence between the coupled waves or power broadening is important.

Finally, it is possible that due to the variable strain as a function of depth in the YIG, which is ignored in the model, the driving fields are not uniform across the thickness of the YIG. This could lead to a broadening in the accessible spin

waves that can be excited and, therefore, an increase in the linewidth. Referring to Fig. 4.2, the displacements and, therefore, strains can be seen to vary over the YIG layer due to the short decay length. This possible contribution could be tested by varying the thickness of the YIG layer.

Taking into account these factors, the model provides reasonable results given the assumptions made and its simplicity, showing good agreement with the experimental data when an effective damping of 12α is used. Solving the fully coupled wave equation would be a good next step to better understand the observed effective damping.

Following the previous measurement, the SAW intensity as a function of propagation distance and applied magnetic field was measured for an angle of $-39.0°$ between the SAW propagation direction and the applied magnetic field. The laser spot was positioned centrally with respect to the aperture and, initially, approximately $1\,\mu$m along the SAW propagation path. The magnetic field was swept, and the laser spot was then stepped $\sim 19\,\mu$m along the propagation direction of the SAW, before again sweeping the field. This process was repeated up to $\sim 475\,\mu$m. The results are shown in Fig. 5.14, where the integrated μ-BLS intensity has been normalised to aid in displaying the results. A pronounced dip in the SAW intensity can be observed at $+37\,$mT, the approximately horizontal line of low intensity; this is again highly non-reciprocal, as no dip at $-37\,$mT can be observed.

The dips in the SAW intensity at approximately $+37\,$mT for the field sweeps, similar to Fig. 5.12, at different SAW propagation distances, were fitted with Lorentzians. There is a slight curvature to the dips with respect to the magnetic field, particularly at smaller propagation distances. This corresponds to an approximately $1.2\,$mT change in the dip position over the total distance. This is probably a result of experimental errors relating to inhomogeneity in the magnetic field. As can be seen in the photograph of the μ-BLS sample stage, Fig. 5.6, the pole faces of the electromagnets are small, approximately $25\,$mm in diameter, and relatively far apart. This suggests there is likely to be an inhomogeneity in the magnetic field across the sample. As the sample was not positioned perfectly centrally between the pole

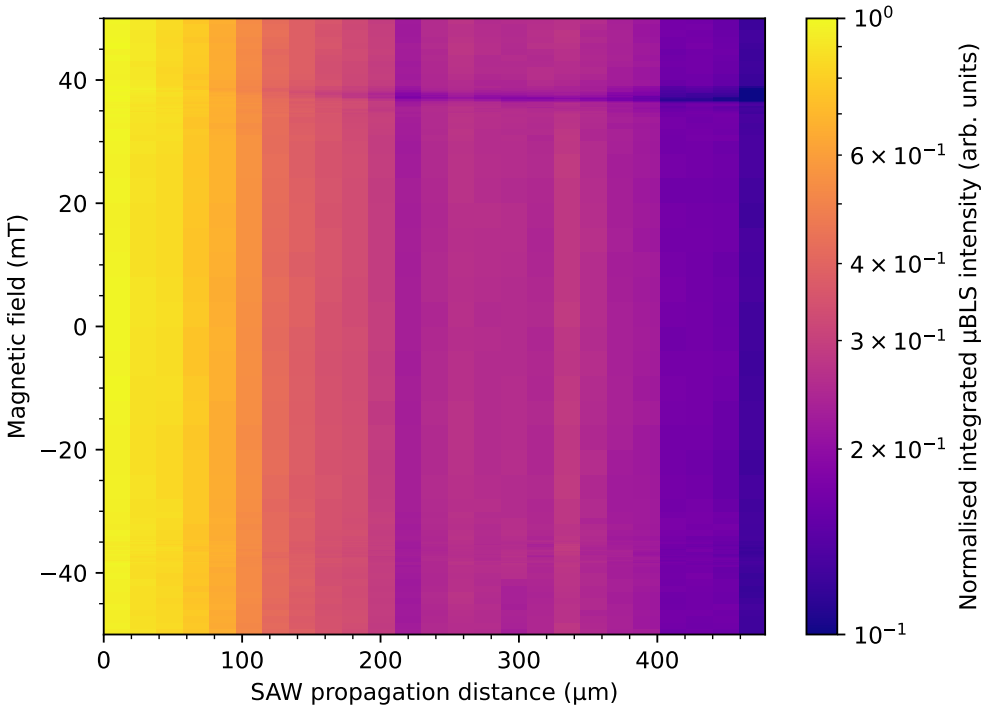

Figure 5.14: Colour map of the normalised integrated μ-BLS intensity as a function of the SAW propagation distance and the magnetic field measured on Sample 1 using the 6 finger IDT. The measurement is taken at 2.9 GHz with an angle of $-39.0°$ between the direction of SAW propagation and the applied magnetic field direction. The μ-BLS laser spot was stepped along the SAW propagation path, and a magnetic field sweep measurement was taken at each step. There is a clear dip in the SAW intensity shown by the approximately horizontal line at $\sim +37$ mT due to the SAW-spin wave coupling. The lack of a similar line at -37 mT indicates the non-reciprocity of the coupling.

faces and the laser spot was scanned at an angle with respect to the magnetic field direction and, therefore, the pole faces; this likely leads to the observed curvature.

The fitted amplitudes of the dips were normalised by dividing the amplitude by the value of C from Eq. (5.6), such that a value of -1 would indicate zero integrated BLS intensity. The resulting normalised dip amplitudes, plotted as a function of distance, are shown, in blue, in Fig. 5.15. These were fitted with an exponentially decaying function, similar to the SAW amplitude fitting in Section 5.4.3, as shown by the red curve. The decay length was found to be $154 \pm 26\,\mu$m, consistent with the value of the SAW decay length for Sample 1 of $127 \pm 31\,\mu$m. This indicates that the rate at which SAW-spin wave coupling occurs is proportional to the SAW intensity, as expected.

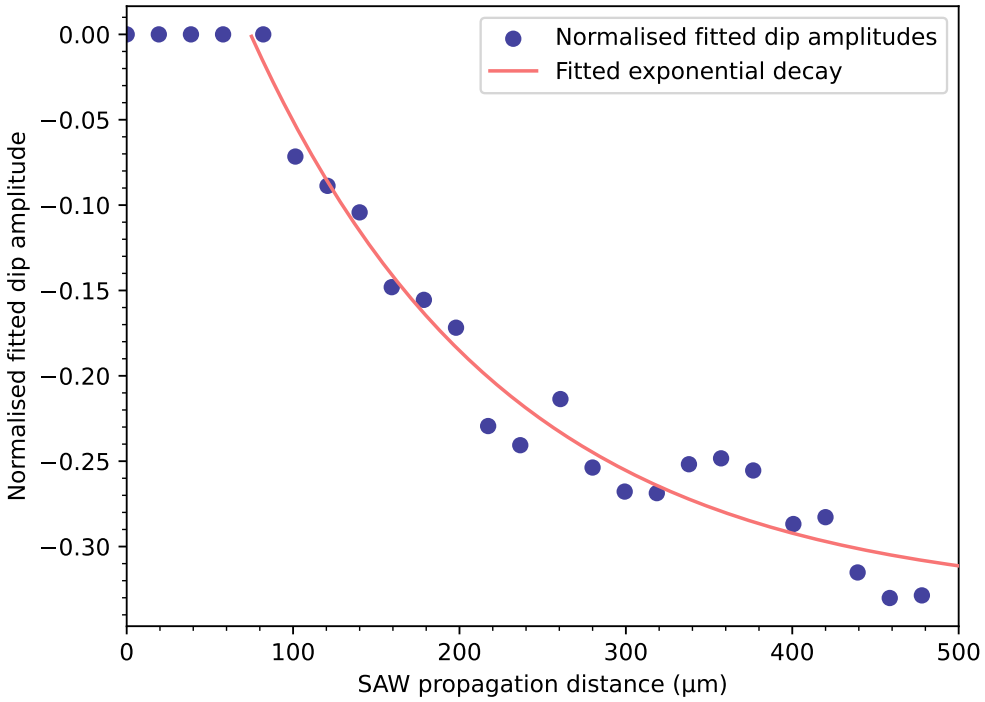

Figure 5.15: The fitted normalised dip amplitudes at positive ($\sim +37\,\mathrm{mT}$) magnetic fields from the experimental data in Fig. 5.14 are shown by the blue points, fitted with an exponentially decaying function shown by the red line. The fit indicates the SAW-spin wave coupling is decaying exponentially, as expected, given the exponential decay in SAW intensity. The decay length calculated is consistent with the decay length of the SAWs found in Section 5.4.3.

Unfortunately, due to a combination of restricted access time to the shared μ-BLS facility at RPTU and the lack of a rotational stage, it was not possible to collect experimental data at a full range of angles. This would be a sensible next step to allow a more detailed comparison between the experimental results and the model. With this experimental data, it would be possible to fit the strain parameters for the driving fields and compare these values to those calculated from the SAW model, giving an indication of the errors in this calculation. It may also be advisable to use micromagnetic simulation software, such as mumax3, to simulate the full spin-wave excitation to better explain the observed effective damping.

A final note: although attempted, it was not possible to directly observe spin waves in the sample. The μ-BLS microscope polariser was rotated 90° to increase sensitivity to spin waves; however, the suppression of SAWs was not perfect, meaning any spin wave signals were too small to measure. This is not helped by the fact

that spin-wave signals in YIG are harder to measure with a 532 nm green laser. The relative permittivity of YIG increases with frequency; a higher relative permittivity enables more efficient coupling between the electromagnetic field of the laser light and the spin waves, enhancing the BLS signal strength. Therefore, a blue laser can be used to increase sensitivity and would be recommended for future attempts to measure spin-wave signals directly, alongside optimising the SAW suppression rate, possibly by changing the polariser.

6
Conclusions and outlook

In conclusion, a method to generate gigahertz frequency SAWs and couple these SAWs to spin waves in YIG has been demonstrated. This was done by first patterning IDTs on the surface of YIG thin films and then RF magnetron sputtering piezoelectric ZnO over the surface. The contact pads of the IDTs were then etched free from the ZnO, enabling direct electrical contact and excitation of SAWs using a microwave signal generator.

The SAW signals were measured using μ-BLS microscopy. The IDT frequency response and SAW group velocities in the YIG/ZnO heterostructures were confirmed to be in good agreement with the theoretical model developed in Chapter 3. This model is applicable to any thin-film multilayer system and can be used to find the properties of SAWs without the need to resort to finite-element modelling software.

Finally, a theoretical model to describe the coupling of SAWs with spin waves in a YIG thin film was presented in Chapter 4. This was shown to explain the highly non-reciprocal nature of the observed coupling. This model shows good agreement with the experimental results, except for the large effective damping observed in the dip in the SAW intensity. This is partially explained by the inhomogeneous line broadening contribution [91]. There may also be a contribution from the broadening due to the relatively short SAW lifetimes. The fully coupled wave equation should be solved to investigate this effect further.

It is hoped that in the future, this SAW-driven non-reciprocal spin-wave generation could be used to probe device ideas such as acoustic isolators or circulators [87, 90, 92], and provide a method for energy-efficient spin-wave excitation, due to the absence of Joule heating. Furthermore, the degree of freedom provided by the IDT geometry lends another advantage to SAW-based spin-wave excitation. In a simple example, as demonstrated in Section 5.4.1, the bandwidth of the IDT frequency response can be narrowed by increasing the number of finger pairs. However, in addition, more complex designs can be realised. For example, curved IDTs can be fabricated to enable the focusing of SAWs [122] or 'chirped' IDTs with a linear gradient in the finger distance and width to achieve a wider bandwidth [123, 124]. Moreover, by locally varying the magnetic field, the interaction region between the SAWs and spin waves can be restricted to a small spatial region. Armed with such advantages, this is a promising technique for studying spin waves, strong magnon-phonon coupling [106, 107], and investigating non-linear SAW-spin-wave interaction phenomena by modifying IDT geometries or patterning additional resonator structures [125, 126].

To enable such work, improving the electromechanical coupling coefficients of the ZnO layer is of the utmost importance. As discussed in Section 3.5.2, it would appear that the coupling can be enhanced by sputtering the ZnO films onto a substrate tilted at 50° to the target, thereby changing the angle of the piezoelectric c-axis. Other possibilities include patterning the IDTs on top of the ZnO, thus avoiding the significant decrease in coupling efficiency caused by the dead layer of ZnO, and doping the ZnO with copper during the sputtering process, which has been shown to increase the electromechanical coupling coefficients by up to sixfold [127, 128].

Finally, the successful deposition of piezoelectric ZnO on YIG, despite the large lattice mismatch [129, 130], suggests it is likely to be possible to excite SAWs in other thin film materials that are lattice-mismatched with ZnO. This demonstrates the versatility of using ZnO as a piezoelectric and possibly opens the door to studying the magnetoelastic interaction in a host of other magnetic media.

Appendices

A

Surface acoustic waves

A.1 Material properties

The values and definitions of the constants used in Eq. (2.1) [74] for the thickness, t, in nanometres of a thin film of ZnO deposited on a quartz disc are given in Tab. A.1. The equation is repeated below for convenience

$$t = \frac{1000 \cdot N_{\mathrm{AT}} \cdot \rho_{\mathrm{quartz}}}{\pi \cdot \rho_{\mathrm{ZnO}} \cdot Z \cdot f_{\mathrm{f}}} \arctan\left(Z \tan\left(\frac{f_{\mathrm{i}} - f_{\mathrm{f}}}{f_{\mathrm{i}}}\pi\right)\right), \quad \text{where} \quad Z = \sqrt{\frac{\rho_{\mathrm{quartz}}\mu_{\mathrm{quartz}}}{\rho_{\mathrm{ZnO}}\mu_{\mathrm{ZnO}}}},$$

f_{i} is the initial frequency in MHz before the deposition, and f_{f} is the frequency after the deposition in MHz.

Table A.1: The values and descriptions of the constants used in the calculation of the thickness of a thin film deposited on a quartz disc.

Symbol	ρ_{quartz}	ρ_{ZnO}	N_{AT}	μ_{quartz}	μ_{ZnO}
Description	Density of quartz [27]	Density of ZnO [27]	Frequency constant of AT-cut quartz [131]	Shear modulus of quartz [131]	Shear modulus of ZnO [131]
Value	$2648\,\mathrm{kgm}^{-3}$	$5676\,\mathrm{kgm}^{-3}$	1661 Hzm	3.32×10^{10} Pa	5.0×10^{10} Pa

The material properties used in the numerical calculations of the SAW properties are given in Tab. A.2.

Table A.2: The material properties for the different layers used in the numerical calculations. Density is given in kgm^{-3}, the elastic constants in $10^9\mathrm{Nm}^{-2}$, the piezoelectric constants in Cm^{-2}, and the permittivities in $10^{-11}\mathrm{Fm}^{-1}$. The relevant references are: ZnO [27]; YIG [132, 133]; and GGG [134, 135]. Any components not listed are zero.

Material	Class	ρ	c_{11}	c_{12}	c_{13}	c_{33}	c_{44}	e_{x5}	e_{z1}	e_{z3}	ϵ_{xx}	ϵ_{zz}
ZnO	6mm	5676	209	121.1	105.1	210.9	42.5	-0.48	-0.57	1.32	8.55	10.2
YIG	$\mathrm{m}\bar{3}\mathrm{m}$	5170	269	107.7	107.7	269	76.4	0	0	0	4.3	4.3
GGG	$\mathrm{m}\bar{3}\mathrm{m}$	7094	285.7	114.9	114.9	285.7	90.2	0	0	0	12.1	12.1
'Dead layer'	N/A	5676	204.7	112.3	113.3	205.6	45.4	0	0	0	9.2	9.0

References

1. Waldrop, M. M. The chips are down for Moore's law. *Nature News* **530,** 144 (2016).
2. Theis, T. N. & Wong, H.-S. P. The end of moore's law: A new beginning for information technology. *Computing in Science & Engineering* **19,** 41–50 (2017).
3. Williams, R. S. What's Next?[The end of Moore's law]. *Computing in Science & Engineering* **19,** 7–13 (2017).
4. Track, E., Forbes, N. & Strawn, G. The end of Moore's Law. *Computing in Science & Engineering* **19,** 4–6 (2017).
5. Freitag, C. *et al.* The real climate and transformative impact of ICT: A critique of estimates, trends, and regulations. *Patterns* **2,** 100340 (2021).
6. Schneider, M. Bose-Einstein condensation of magnons by rapid cooling and its interplay with spin orbit torque (2021).
7. Chumak, A. V., Vasyuchka, V. I., Serga, A. A. & Hillebrands, B. Magnon spintronics. *Nature Physics* **11,** 453–461 (2015).
8. Khitun, A. & Krivorotov, l. in *Spintronics Handbook: Spin Transport and Magnetism, Second Edition: Nanoscale Spintronics and Applications—Volume Three* 571–600 (CRC Press, 2019).
9. Münzenberg, M. High-speed spins. *Nature Physics* **17,** 985–986 (2021).
10. Stancil, D. D. & Prabhakar, A. *Spin waves* 139–202 (Springer, 2009).
11. Gurevich, A. G. & Melkov, G. A. *Magnetization oscillations and waves* 179–279 (CRC press, 2020).
12. Chumak, A., Dhagat, P., Jander, A., Serga, A. & Hillebrands, B. Reverse Doppler effect of magnons with negative group velocity scattered from a moving Bragg grating. *Physical Review B* **81,** 140404 (2010).
13. Gruszecki, P. *et al.* in *Solid State Physics* 79–132 (Elsevier, 2019).
14. Demokritov, S. O., Hillebrands, B. & Slavin, A. N. Brillouin light scattering studies of confined spin waves: linear and nonlinear confinement. *Physics Reports* **348,** 441–489 (2001).
15. Chumak, A. V., Serga, A. A. & Hillebrands, B. Magnon transistor for all-magnon data processing. *Nature communications* **5,** 4700 (2014).
16. Chumak, A. *et al. All-linear time reversal by a dynamic artificial crystal Nat* 2010.
17. Karenowska, A. *Some Magnetic Reflections on Wave Dynamics* PhD thesis (Oxford University, UK, 2011).

18. Fischer, T. *et al.* Experimental prototype of a spin-wave majority gate. *Applied Physics Letters* **110,** 152401 (2017).
19. Wang, Q. *et al.* A magnonic directional coupler for integrated magnonic half-adders. *Nature Electronics* **3,** 765–774 (2020).
20. Papp, Á., Porod, W. & Csaba, G. Nanoscale neural network using non-linear spin-wave interference. *Nature communications* **12,** 6422 (2021).
21. Barman, A. *et al.* The 2021 Magnonics Roadmap. *Journal of Physics: Condensed Matter* **33,** 413001 (Aug. 2021).
22. Li, X., Labanowski, D., Salahuddin, S. & Lynch, C. S. Spin wave generation by surface acoustic waves. *Journal of Applied Physics* **122,** 043904 (July 2017).
23. Mahmoud, A. *et al.* Introduction to spin wave computing. *Journal of Applied Physics* **128,** 161101 (Oct. 2020).
24. Chumak, A. V. *et al.* Advances in magnetics roadmap on spin-wave computing. *IEEE Transactions on Magnetics* **58,** 1–72 (2022).
25. Ryburn, F. *et al.* Generation of gigahertz frequency surface acoustic waves in YIG/ZnO heterostructures. *arXiv preprint arXiv:2403.03006* (2024).
26. Rayleigh, L. On waves propagated along the plane surface of an elastic solid. *Proceedings of the London mathematical Society* **1,** 4–11 (1885).
27. Zhang, G. *Bulk and Surface Acoustic Waves* (CRC Press, Jan. 2022).
28. Campbell, C. *Surface Acoustic Wave Devices for Mobile and Wireless Communications, Four-Volume Set* (Academic press, 1998).
29. Ruby, R. A Snapshot in Time: The Future in Filters for Cell Phones. *IEEE Microwave Magazine* **16,** 46–59 (2015).
30. Gronewold, T. M. Surface acoustic wave sensors in the bioanalytical field: Recent trends and challenges. *Analytica Chimica Acta* **603,** 119–128 (2007).
31. Mandal, D. & Banerjee, S. Surface Acoustic Wave (SAW) Sensors: Physics, Materials, and Applications. *Sensors* **22** (2022).
32. Wohltjen, H. Mechanism of operation and design considerations for surface acoustic wave device vapour sensors. *Sensors and Actuators* **5,** 307–325 (1984).
33. Parker, T. & Montress, G. Precision surface-acoustic-wave (SAW) oscillators. *IEEE Transactions on Ultrasonics, Ferroelectrics, and Frequency Control* **35,** 342–364 (1988).
34. Ding, X. *et al.* Surface acoustic wave microfluidics. *Lab on a Chip* **13,** 3626–3649 (2013).
35. Destgeer, G. & Sung, H. J. Recent advances in microfluidic actuation and micro-object manipulation via surface acoustic waves. *Lab on a Chip* **15,** 2722–2738 (2015).
36. Ziman, J. *Electrons and Phonons: The Theory of Transport Phenomena in Solids* 1–3 (Oxford University Press, 2001).
37. Steinem, C. & Janshoff, A. in *Encyclopedia of Analytical Science (Second Edition)* (eds Worsfold, P., Townshend, A. & Poole, C.) Second Edition, 269–276 (Elsevier, Oxford, 2005).

38. Hering, E., Martin, R. & Stohrer, M. *Physik für Ingenieure* (Springer Berlin Heidelberg, 2013).
39. Koike, J., Shimoe, K. S. K. & Ieki, H. I. H. 1.5 GHz Low-Loss Surface Acoustic Wave Filter Using ZnO/Sapphire Substrate. *Japanese Journal of Applied Physics* **32,** 2337 (May 1993).
40. Le Brizoual, L. *et al.* GHz frequency ZnO/Si SAW device. *IEEE Transactions on Ultrasonics, Ferroelectrics, and Frequency Control* **55,** 442–450 (2008).
41. Wang, Q. J. *et al.* Gigahertz surface acoustic wave generation on ZnO thin films deposited by radio frequency magnetron sputtering on III-V semiconductor substrates. *Journal of Vacuum Science & Technology B: Microelectronics and Nanometer Structures Processing, Measurement, and Phenomena* **26,** 1848–1851 (Nov. 2008).
42. Fu, S. *et al.* High-Frequency Surface Acoustic Wave Devices Based on ZnO/SiC Layered Structure. *IEEE Electron Device Letters* **40,** 103–106 (2019).
43. Su, R. *et al.* Enhanced performance of ZnO/SiO2/Al2O3 surface acoustic wave devices with embedded electrodes. *ACS Applied Materials & Interfaces* **12,** 42378–42385 (2020).
44. *General Properties of ZnO* 1–76 (John Wiley & Sons, Ltd, 2009).
45. Köhl, D. *The influence of energetic bombardment on the structure formation of sputtered zinc oxide films. Development of an atomistic growth model and its application to tailor thin film properties* PhD thesis (RWTH Aachen University, Germany, 2011).
46. Landau, L. & Lifshitz, E. On the theory of the dispersion of magnetic permeability in ferromagnetic bodies. *Phys. Z. Sowjet.* **8,** 135 (1935).
47. Gilbert, T. L. A phenomenological theory of damping in ferromagnetic materials. *IEEE transactions on magnetics* **40,** 3443–3449 (2004).
48. Lakshmanan, M. The fascinating world of the Landau–Lifshitz–Gilbert equation: an overview. *Philosophical Transactions of the Royal Society A: Mathematical, Physical and Engineering Sciences* **369,** 1280–1300 (2011).
49. Qin, H., Hämäläinen, S. J., Arjas, K., Witteveen, J. & van Dijken, S. Propagating spin waves in nanometer-thick yttrium iron garnet films: Dependence on wave vector, magnetic field strength, and angle. *Phys. Rev. B* **98,** 224422 (22 Dec. 2018).
50. Maendl, S., Stasinopoulos, I. & Grundler, D. Spin waves with large decay length and few 100 nm wavelengths in thin yttrium iron garnet grown at the wafer scale. *Applied Physics Letters* **111,** 012403 (July 2017).
51. Fujii, T. & Sakabe, Y. in *Encyclopedia of Materials: Science and Technology* (eds Buschow, K. J. *et al.*) 3666–3670 (Elsevier, Oxford, 2001).
52. Wu, M. in (eds Camley, R. E. & Stamps, R. L.) 163–224 (Academic Press, 2010).
53. Inglis, A. *Investigating a phase conjugate mirror for magnon-based computing* (Springer Nature, 2020).
54. Schlömann, E. & Joseph, R. Generation of spin waves in nonuniform magnetic fields. III. Magnetoelastic interaction. *Journal of Applied Physics* **35,** 2382–2390 (1964).

55. Engelhardt, F., Bittencourt, V., Huebl, H., Klein, O. & Kusminskiy, S. Optimal Broadband Frequency Conversion via a Magnetomechanical Transducer. *Physical Review Applied* **18** (Oct. 2022).

56. Kittel, C. Physical theory of ferromagnetic domains. *Reviews of modern Physics* **21,** 541 (1949).

57. Bitter, F., Yensen, T. & Zwicky, F. *Introduction to Ferromagnetism* (McGraw-Hill, 1937).

58. Auld, B. *Magnetostatic and magnetoelastic wave propagation in solids* (Academic Press Inc, 1971).

59. Chikazumi, S. & Graham, C. D. *Physics of ferromagnetism* **94** (Oxford university press, 1997).

60. Cherepanov, V., Kolokolov, I. & L'vov, V. The saga of YIG: Spectra, thermodynamics, interaction and relaxation of magnons in a complex magnet. *Physics reports* **229,** 81–144 (1993).

61. Du, X. *et al. ZnO film for application in surface acoustic wave device* in *Journal of Physics: Conference Series* **76** (2007), 012035.

62. Hanna, S. & Murphy, G. Interactions between magnetostatic and surface acoustic waves in garnet films. *IEEE Transactions on Magnetics* **24,** 2814–2816 (1988).

63. Kryshtal, R. & Medved, A. Nonlinear spin waves in dynamic magnonic crystals created by surface acoustic waves in yttrium iron garnet films. *Journal of Physics D: Applied Physics* **50,** 495004 (2017).

64. Fung, T. *Phonon magnonics* PhD thesis (University of Oxford, 2015).

65. Furuya, A. & Hirono, S. Target magnetic-field effects on deposition rate in rf magnetron sputtering. *Journal of Applied Physics* **68,** 304–310 (July 1990).

66. Yildirim, B. & Tigli, O. Comprehensive characterization of ZnO thin films for surface acoustic wave applications. *Journal of Materials Science: Materials in Electronics* **30,** 14621–14630 (Aug. 2019).

67. Krishnaswamy, S., McAvoy, B., Takei, W. & Moore, R. *Oriented ZnO films for microwave shear mode transducers* in *1982 Ultrasonics Symposium* (1982), 476–479.

68. Ko, K.-H. *et al.* Structural and optical properties of a radio frequency magnetron-sputtered ZnO thin film with different growth angles. *Nanoscale research letters* **7,** 1–5 (2012).

69. Anderson, A. & Oates, D. *RF Magnetron sputtering of ZnO for SAW: Effects of magnetic field strength and configuration* in *1982 Ultrasonics Symposium* (1982), 329–333.

70. Khuri-Yakub, B. T., Kino, G. & Galle, P. Studies of the optimum conditions for growth of rf-sputtered ZnO films. *Journal of Applied Physics* **46,** 3266–3272 (1975).

71. Shiosaki, T., Ooishi, M., Ohnishi, S. & Kawabata, A. *Fabrication of ZnO piezoelectric film by planar magnetron RF sputtering equipment* in *Proceedings of the 1st meeting on ferroelectric materials and their applications* (1978).

72. Bachari, E., Baud, G., Ben Amor, S. & Jacquet, M. Structural and optical properties of sputtered ZnO films. *Thin Solid Films* **348,** 165–172 (1999).

73. Lin, S.-S. & Huang, J.-L. Effect of thickness on the structural and optical properties of ZnO films by r.f. magnetron sputtering. *Surface and Coatings Technology* **185,** 222–227 (2004).

74. Lu, C.-S. & Lewis, O. Investigation of film-thickness determination by oscillating quartz resonators with large mass load. *Journal of Applied Physics* **43,** 4385–4390 (Nov. 2003).

75. Dubs, C. *et al.* Low damping and microstructural perfection of sub-40nm-thin yttrium iron garnet films grown by liquid phase epitaxy. *Phys. Rev. Mater.* **4,** 024416 (2 Feb. 2020).

76. Howe, B. M. *et al.* Pseudomorphic Yttrium Iron Garnet Thin Films With Low Damping and Inhomogeneous Linewidth Broadening. *IEEE Magnetics Letters* **6,** 1–4 (2015).

77. Damjanovic, D. Ferroelectric, dielectric and piezoelectric properties of ferroelectric thin films and ceramics. *Reports on progress in physics* **61,** 1267 (1998).

78. Farnell, G. & Adler, E. in (eds Mason, W. P. & Thurston, R.) 35–127 (Academic Press, 1972).

79. Sezawa, K. Dispersion of elastic waves propagated on the surface of stratified bodies and on curved surfaces. *Bull. Earthq. Res. Inst. Tokyo* **3,** 1–18 (1927).

80. Love, A. E. H. *Some Problems of Geodynamics: Being an Essay to which the Adams Prize in the University of Cambridge was Adjudged in 1911* (University Press, 1911).

81. Den Toonder, J., Van Dommelen, J. & Baaijens, F. The relation between single crystal elasticity and the effective elastic behaviour of polycrystalline materials: theory, measurement and computation. *Modelling and Simulation in Materials Science and Engineering* **7,** 909 (1999).

82. Foster, N., Coquin, G., Rozgonyi, G. & Vannatta, F. Cadmium Sulphide and Zinc Oxide Thin-Film Transducers. *IEEE Transactions on Sonics and Ultrasonics* **15,** 28–40 (1968).

83. Yanagitani, T., Morisato, N., Takayanagi, S., Matsukawa, M. & Watanabe, Y. c-Axis Zig-Zag ZnO film ultrasonic transducers for designing longitudinal and shear wave resonant frequencies and modes. *IEEE Transactions on Ultrasonics, Ferroelectrics and Frequency Control* **58** (2011).

84. Laude, V. & Ballandras, S. Slowness curves and characteristics of surface acoustic waves propagating obliquely in periodic finite-thickness electrode gratings. *Journal of Applied Physics* **94,** 1235–1242 (June 2003).

85. O'Rorke, R., Winkler, A., Collins, D. & Ai, Y. Slowness curve surface acoustic wave transducers for optimized acoustic streaming. *RSC advances* **10,** 11582–11589 (2020).

86. Maupin, V. in *Advances in Wave Propagation in Heterogenous Earth* (eds Wu, R.-S., Maupin, V. & Dmowska, R.) 127–155 (Elsevier, 2007).

87. Sasaki, R., Nii, Y., Iguchi, Y. & Onose, Y. Nonreciprocal propagation of surface acoustic wave in Ni/$LiNbO_3$. *Phys. Rev. B* **95,** 020407(R) (2 Jan. 2017).

88. Tateno, S. & Nozaki, Y. Highly Nonreciprocal Spin Waves Excited by Magnetoelastic Coupling in a Ni/Si Bilayer. *Phys. Rev. Appl.* **13,** 034074 (3 Mar. 2020).

89. Hernández-Mínguez, A., Maciá, F., Hernández, J. M., Herfort, J. & Santos, P. V. Large Nonreciprocal Propagation of Surface Acoustic Waves in Epitaxial Ferromagnetic/Semiconductor Hybrid Structures. *Phys. Rev. Appl.* **13,** 044018 (4 Apr. 2020).

90. Xu, M. *et al.* Nonreciprocal surface acoustic wave propagation via magneto-rotation coupling. *Science Advances* **6,** eabb1724 (2020).

91. Küß, M. *et al.* Nonreciprocal Dzyaloshinskii–Moriya Magnetoacoustic Waves. *Phys. Rev. Lett.* **125,** 217203 (21 Nov. 2020).

92. Küß, M. *et al.* Symmetry of the Magnetoelastic Interaction of Rayleigh and Shear Horizontal Magnetoacoustic Waves in Nickel Thin Films on $LiTaO_3$. *Phys. Rev. Appl.* **15,** 034046 (3 Mar. 2021).

93. Küß, M. *et al.* Nonreciprocal Magnetoacoustic Waves in Dipolar-Coupled Ferromagnetic Bilayers. *Phys. Rev. Appl.* **15,** 034060 (3 Mar. 2021).

94. Li, Y., Zhao, C., Zhang, W., Hoffmann, A. & Novosad, V. Advances in coherent coupling between magnons and acoustic phonons. *APL Materials* **9,** 060902 (June 2021).

95. Geilen, M. *et al.* Fully resonant magneto-elastic spin-wave excitation by surface acoustic waves under conservation of energy and linear momentum. *Applied Physics Letters* **120,** 242404 (June 2022).

96. Küß, M. *et al.* Nonreciprocal magnetoacoustic waves in synthetic antiferromagnets with Dzyaloshinskii-Moriya interaction. *Phys. Rev. B* **107,** 024424 (2 Jan. 2023).

97. Küß, M. *et al.* Nonreciprocal transmission of magnetoacoustic waves in compensated synthetic antiferromagnets. *Phys. Rev. B* **107,** 214412 (21 June 2023).

98. Huang, M., Hu, W., Zhang, H. & Bai, F. Phonon–magnon conversion using longitudinal leaky surface acoustic waves through magnetoelastic coupling. *Journal of Applied Physics* **133,** 223902 (June 2023).

99. Kunz, Y. *et al.* Coherent phonon-magnon interactions detected by micro-focused Brillouin light scattering spectroscopy. *arXiv preprint arXiv:2311.16688* (2023).

100. Shah, P. J. *et al.* Giant nonreciprocity of surface acoustic waves enabled by the magnetoelastic interaction. *Science Advances* **6,** eabc5648 (2020).

101. Verba, R., Bankowski, E. N., Meitzler, T. J., Tiberkevich, V. & Slavin, A. Phase Nonreciprocity of Microwave-Frequency Surface Acoustic Waves in Hybrid Heterostructures with Magnetoelastic Coupling. *Advanced Electronic Materials* **7,** 2100263 (2021).

102. Rasmussen, C., Quan, L. & Alù, A. Acoustic nonreciprocity. *Journal of Applied Physics* **129,** 210903 (June 2021).

103. Küß, M., Albrecht, M. & Weiler, M. Chiral Magnetoacoustics. *Frontiers in Physics* **10** (2022).

104. Rana, B., Fukuma, Y., Miura, K., Takahashi, H. & Otani, Y. Excitation of coherent propagating spin waves in ultrathin CoFeB film by voltage-controlled magnetic anisotropy. *Applied Physics Letters* **111,** 052404 (Aug. 2017).

105. Nikitchenko, A. I. & Pertsev, N. A. Spin-orbit torque control of spin waves in a ferromagnetic waveguide. *Phys. Rev. B* **104,** 134422 (13 Oct. 2021).

106. Hwang, Y. *et al.* Strongly Coupled Spin Waves and Surface Acoustic Waves at Room Temperature. *arXiv preprint arXiv:2309.12690* (2023).

107. Hwang, Y. *et al.* Strongly Coupled Spin Waves and Surface Acoustic Waves at Room Temperature. *Physical Review Letters* **132,** 056704 (2024).

108. Dreher, L. *et al.* Surface acoustic wave driven ferromagnetic resonance in nickel thin films: Theory and experiment. *Physical Review B* **86,** 134415 (2012).

109. Baselgia, L. *et al.* Derivation of the resonance frequency from the free energy of ferromagnets. *Physical Review B* **38,** 2237 (1988).

110. Moon, J.-H. *et al.* Spin-wave propagation in the presence of interfacial Dzyaloshinskii-Moriya interaction. *Physical Review B* **88,** 184404 (2013).

111. Wu, M. Nonlinear spin waves in magnetic film feedback rings. *Solid State Physics* **62,** 163–224 (2010).

112. Harte, K. Theory of magnetization ripple in ferromagnetic films. *Journal of Applied Physics* **39,** 1503–1524 (1968).

113. Maekawa, S. & Tachiki, M. *Surface acoustic attenuation due to surface spin wave in ferro-and antiferromagnets* in *AIP Conference Proceedings* **29** (1976), 542–543.

114. Polder, D. VIII. On the theory of ferromagnetic resonance. *The London, Edinburgh, and Dublin Philosophical Magazine and Journal of Science* **40,** 99–115 (1949).

115. Klingler, S. *et al.* Measurements of the exchange stiffness of YIG films using broadband ferromagnetic resonance techniques. *Journal of Physics D: Applied Physics* **48,** 015001 (2014).

116. Comstock, R. Magnetoelastic coupling constants of the ferrites and garnets. *Proceedings of the IEEE* **53,** 1508–1517 (1965).

117. Sebastian, T., Schultheiss, K., Obry, B., Hillebrands, B. & Schultheiss, H. Micro-focused Brillouin light scattering: imaging spin waves at the nanoscale. *Frontiers in Physics* **3** (2015).

118. Büttner, O. *et al.* Spatial and spatiotemporal self-focusing of spin waves in garnet films observed by space- and time-resolved Brillouin light scattering. *Journal of Applied Physics* **87,** 5088–5090 (May 2000).

119. Demidov, V. E., Demokritov, S. O., Hillebrands, B., Laufenberg, M. & Freitas, P. P. Radiation of spin waves by a single micrometer-sized magnetic element. *Applied Physics Letters* **85,** 2866–2868 (Oct. 2004).

120. Heinz, B. M. *Nano-scaled yttrium iron garnet conduits for magnonic networks* PhD thesis (Rheinland-Pfälzische Technische Universität Kaiserslautern-Landau, 2021).

121. Chen, Y.-Y., Wu, T.-T. & Chou, T.-T. Analysis of the frequency response of a dispersive IDT/ZnO/sapphire SAW filter using effective permittivity and the coupling of modes model. *Journal of Physics D: Applied Physics* **37,** 120 (2003).

122. Bourquin, Y., Reboud, J., Wilson, R. & Cooper, J. M. Tuneable surface acoustic waves for fluid and particle manipulations on disposable chips. *Lab on a Chip* **10,** 1898–1901 (2010).

123. Syamsu, I. *et al. Design and fabrication of AlN-on-Si chirped surface acoustic wave resonators for label-free cell detection* in *Journal of Physics: Conference Series* **1319** (2019), 012011.

124. Mazalan, M. B., Noor, A. M., Wahab, Y., Yahud, S. & Zaman, W. S. W. K. Current development in interdigital transducer (IDT) surface acoustic wave devices for live cell in vitro studies: A review. *Micromachines* **13,** 30 (2021).

125. Geilen, M. *et al. Parametric Excitation and Instabilities of Spin Waves driven by Surface Acoustic Waves* 2022.

126. Shah, P. J. *et al. Symmetry and nonlinearity of spin wave resonance excited by focused surface acoustic waves* 2023.

127. Lee, J.-B., Lee, H.-J., Seo, S.-H. & Park, J.-S. Characterization of undoped and Cu-doped ZnO films for surface acoustic wave applications. *Thin Solid Films* **398,** 641–646 (2001).

128. Wang, X. *et al.* The influence of different doping elements on microstructure, piezoelectric coefficient and resistivity of sputtered ZnO film. *Applied Surface Science* **253,** 1639–1643 (2006).

129. Abrahams, S. C. & Bernstein, J. L. Remeasurement of the structure of hexagonal ZnO. *Acta Crystallographica Section B* **25,** 1233–1236 (July 1969).

130. Gurjar, G., Sharma, V., Patnaik, S. & Kuanr, B. K. Structural and magnetic properties of high quality single crystalline YIG thin film: A comparison with the bulk YIG. *AIP Conference Proceedings* **2115,** 030323 (July 2019).

131. *074-547-P1B Q-pod operating manual - INFICON* Accessed: 2024-18-03.

132. Clark, A. E. & Strakna, R. E. Elastic Constants of Single-Crystal YIG. *Journal of Applied Physics* **32,** 1172–1173 (June 2004).

133. Hasan, I. H., Hamidon, M. N., Ismail, I., Osman, R. & Ismail, A. *Yttrium iron garnet thick film inclusion for enhanced microstrip patch antenna performance* in *2017 IEEE Regional Symposium on Micro and Nanoelectronics (RSM)* (2017), 131–134.

134. Graham, L. J. & Chang, R. Elastic Moduli of Single-Crystal Gadolinium Gallium Garnet. *Journal of Applied Physics* **41,** 2247–2248 (Nov. 2003).

135. Connelly, D. A. *et al.* Complex Permittivity of Gadolinium Gallium Garnet From 8.2 to 12.4 GHz. *IEEE Magnetics Letters* **12,** 1–4 (2021).